

GROWTH AND CHARACTERIZATION OF SINGLE QUANTUM DOT DEVICES FOR FIBER-BASED QUANTUM COMMUNICATIONS

THÈSE N^o 3698 (2006)

PRÉSENTÉE LE 15 DÉCEMBRE 2006

À LA FACULTÉ DES SCIENCES DE BASE

Institut de photonique et d'électronique quantiques

SECTION DE PHYSIQUE

ÉCOLE POLYTECHNIQUE FÉDÉRALE DE LAUSANNE

POUR L'OBTENTION DU GRADE DE DOCTEUR ÈS SCIENCES

PAR

Blandine ALLOING

ingénieur, ENSI, Caen, France
de nationalité française

acceptée sur proposition du jury:

Prof. G. Meylan, président du jury

Prof. A. Fiore, directeur de thèse

Prof. N. Grandjean, rapporteur

Prof. M. Gurioli, rapporteur

Dr J.-C. Harmand, rapporteur



ÉCOLE POLYTECHNIQUE
FÉDÉRALE DE LAUSANNE

Lausanne, EPFL

2006

*À ma famille,
et tout particulièrement
à mon père,*

Contents

Abstract	7
Résumé	9
Kurzfassung	11
1 Introduction	13
1.1 Single photon emitter	13
1.1.1 Applications	14
1.1.2 Different types of single photon sources	16
1.2 Self-assembled quantum dots as single photon emitters	19
1.2.1 Quantum confinement	19
1.2.2 Advantages and drawbacks	20
1.2.3 Single photon generation with single quantum dots: overview	21
1.3 Outline of the manuscript	22
2 Experimental Techniques	25
2.1 Epitaxy with molecular beam epitaxy (MBE) system	25
2.1.1 Principle, advantages and drawbacks	25
2.1.2 III-V growth with VG 80 system	26
2.1.3 Growth rate measurements	28
2.2 In situ characterization: RHEED	29
2.2.1 Principle	29
2.2.2 Characterizations	29
2.3 Structural characterization by AFM	32
2.4 Processing techniques	33
2.4.1 Sample masking	33
2.4.2 Mesa etching	34
2.4.3 Isolating layer	35

2.4.4	Contact deposition	36
2.5	Photoluminescence setup	36
2.5.1	Macro-photoluminescence	36
2.5.2	Micro-photoluminescence	37
2.5.3	Time-resolved photoluminescence	37
3	Growth of InAs/GaAs quantum dots	39
3.1	Self-assembled quantum dots	40
3.1.1	Growth modes	40
3.1.2	Coherent island or dislocations?	41
3.1.3	Nucleation mechanisms	42
3.1.4	Mechanism of size ordering versus Ostwald ripening	43
3.2	Growth optimization	44
3.2.1	First approach: decrease of InAs thickness	45
3.2.2	Second approach: growth rate effect	46
3.2.3	Optimization of the capping layer	49
3.2.4	Substrate misorientation	52
3.2.5	Other optimization: growth interruption	53
3.2.6	Conclusion	55
3.3	Assessment of desorption rate	56
3.4	TEM characterizations	59
3.5	Conclusion	63
4	Characterization of QD ensembles	65
4.1	Comparative studies	65
4.1.1	Photoluminescence experiments	66
4.1.2	Time-resolved photoluminescence experiments	68
4.2	Temperature dependence	71
4.3	Conclusion	74
5	Single quantum dot spectroscopy	75
5.1	Characterization technique	75
5.1.1	Isolation of single quantum dot	76

5.1.2	Insertion in a microcavity	77
5.2	Characterization of single quantum dots	77
5.2.1	Pump power dependence	77
5.2.2	Temperature dependence	81
5.2.3	Time-resolved experiment	81
5.2.4	Antibunching experiment	82
5.3	Insertion of low-density quantum dots in a high quality factor microcavity	85
5.3.1	Spontaneous emission in a microcavity in the weak coupling regime	85
5.3.2	Micropillar	88
5.3.3	Photonic crystal microcavity	92
5.4	Conclusion	93
6	Single quantum dots in light emitting diodes	95
6.1	Comparison of different approaches	96
6.2	Metal aperture light emitting diodes	97
6.2.1	First structure: metal aperture	97
6.2.2	Measurements	97
6.2.3	Second structure: metal aperture and mesa etching	99
6.2.4	Conclusion	101
6.3	Current-aperture LEDs	101
6.3.1	Structure	101
6.3.2	Processing steps	101
6.3.3	Limitation: current spreading and carrier diffusion	102
6.3.4	Diffusion coefficient and diffusion length	104
6.3.5	Current-voltage measurements	106
6.3.6	Light-current measurements	107
6.3.7	Electroluminescence measurements at low temperature	109
6.3.8	Conclusion	111
6.4	Microcavity light emitting diode	111
6.4.1	Structure	111
6.4.2	Current-voltage characteristics	113
6.4.3	Light-current characterisation	113
6.4.4	Spectral characterization	114

6.4.5	Alternative approach: planarized micropillar	117
6.5	Conclusion	122
	Conclusions	123
	Bibliography	126
	Acknowledgements	149
	Curriculum Vitae and Publications	151

Abstract

Single photon sources have recently attracted significant interest for their potential role in the future applications of quantum cryptography, and in the longer term, quantum computing. Among the different types of single photon emitters, semiconductor quantum dots (QDs) are good candidates as they combine discrete electronic transitions with the possibility of electrical excitation. Self-assembled InAs QDs on GaAs substrate are by far the most studied system as they can easily be grown into a microcavity structure. Embedding these into a microcavity is important as it increases the extraction efficiency, directionality and speeds up the photon emission. Until now, most studies have concentrated on QDs emitting in the $\lambda < 1000$ nm range. However fiber-based quantum communication applications require an emission wavelength in the 1300 or 1550 nm transmission window where optical losses of silica fiber are minimal. Hence, the purpose of this study is to realize a single photon source from self-assembled InAs/GaAs QDs emitting at 1300 nm. This poses difficulties associated first with the QD epitaxial growth as large and sparse InAs QDs are required, and second with the single photon Detection as single photon detection system in the near-infrared presents a poor quantum efficiency and signal to noise ratio.

The first part of this thesis is devoted to optimising the QD growth. A low area QD density is required in order to obtain the isolation of a single QD. Moreover, the QD size must be large enough to obtain emission wavelengths around 1300 nm at low temperatures (10K), i.e. 1400nm at room temperature. We present here the optimization of a growth procedure that allowed the fabrication of low-density QDs ($2 \cdot \mu m^{-2}$) emitting at the predicted wavelengths and showing a very good size homogeneity. In addition, we show comparative studies on the optical characteristics of these low-density QDs with higher density QDs. These show that the low area density does not imply a reduction of the carrier capture efficiency of the QDs.

The second part of this thesis concentrates on the spectroscopy of single QDs under optical and electrical pumping. By careful optimization of the detection system, single QD emission has been demonstrated. Single photon emission at 1300 nm was also proven by

means of an anti-correlation experiment. Preliminary results of low-density QDs inserted into three-dimensional microcavities such as a micropillar and a photonic crystal structures are also presented. Further experiments are under way.

Finally, the fabrication and characterization of single QD light emitting diodes (LED) are detailed. Electrical injection poses additional problems, notably in term of device processing and carrier diffusion. Different designs of LED structures have been tested. The results are discussed. Finally, electroluminescence emission from a single QD under electrical injection is reported.

Keywords: semiconductor, quantum dots, molecular beam epitaxy, single photon, microcavity, light emitting diode.

Résumé

L'intérêt pour les sources à photons uniques a récemment fortement augmenté en vue de leurs futures applications dans les domaines de la cryptographie quantique et de l'ordinateur quantique à plus long terme. Parmi les différents types d'émetteurs à photons uniques, les boîtes quantiques (BQs) à semiconducteurs sont un candidat intéressant car elles possèdent des niveaux électroniques discrets. De plus l'injection électrique dans les BQs est possible. Les BQs auto-organisées InAs sur substrat de GaAs en particulier, sont de loin le système le plus étudié car elles peuvent être facilement incorporées dans une microcavité. Un environnement en microcavité augmente l'efficacité d'extraction, la directionalité et l'émission spontanée de photons. Jusqu'à maintenant, la plupart des études se sont concentrées sur les boîtes quantiques émettant dans le domaine des longueurs d'ondes inférieures à 1000 nm. Pourtant, les longueurs d'ondes correspondant au minimum d'atténuation dans les fibres optiques en silice se situent autour de 1300 et 1550 nm. Ce sont donc les longueurs d'onde requises pour une application dans les communications quantiques transmises par fibres optiques. Le but de cette étude est ainsi de réaliser une source à photons uniques à partir de boîtes quantiques InAs/GaAs auto-organisées émettant à 1300 nm. Ceci pose des difficultés liées d'abord à la croissance des BQs (cela nécessite en effet des BQs larges et diluées) et également à la détection de photons uniques (les systèmes de détection de photons uniques pour le proche infrarouge présentent en effet une faible efficacité quantique et un faible rapport signal sur bruit.).

La première partie de cette thèse est consacrée à l'optimisation de croissance des BQs. Une faible densité de surface des BQs est nécessaire pour faciliter l'isolation d'une BQ unique à l'intérieur d'un dispositif. De plus, la taille de ces BQs doit être suffisamment grande pour que leur longueur d'onde d'émission atteigne 1300 nm à basse température (10 K) c'est-à-dire 1400 nm à température ambiante. Nous avons mis au point une procédure de croissance qui permet de fabriquer des BQs à faible densité ($2 \cdot \mu\text{m}^{-2}$), émettant à la longueur d'onde souhaitée et présentant une très bonne homogénéité en taille. Des études comparatives sur les propriétés optiques des BQs à différentes densités de surface ont également été menées

et ont montré qu'une très faible densité de BQs n'impliquait pas forcément une plus faible efficacité de capture des porteurs dans les BQs.

La deuxième partie de cette thèse se concentre sur la spectroscopie de BQs uniques sous excitation optique et électrique. Par une optimisation soignée du système de détection, l'émission d'une boîte quantique unique a pu être observée, la preuve de l'émission de photons uniques étant apportée par les expériences d'anticorrélation. Des résultats préliminaires sur les BQs dans des microcavités tridimensionnelles comme les micropiliers ou les cristaux photoniques sont également présentés. Des études plus approfondies sont en cours.

La fabrication et la caractérisation de diodes luminescentes à BQs uniques sont finalement abordées. L'injection électrique pose des problèmes supplémentaires relatifs notamment au processus de fabrication des dispositifs et à la diffusion des porteurs. Différents designs de structures ont été testés et les résultats sont discutés. Des mesures d'électroluminescence sur BQs uniques ont finalement été réalisées.

Mots-clés: semiconducteur, boîte quantique, épitaxie à jets moléculaires, photon unique, microcavité, diode électroluminescente.

Kurzfassung

Ein-Photonen-Quellen sind seit einigen Jahren ein hochaktives Forschungsfeld. Verantwortlich hierfür sind ihre potentiellen Anwendungen in der Quantenkryptographie sowie, eher langfristig, in Quanten-Rechnern. Unter den verschiedenen Typen von Ein-Photonen-Quellen sind insbesondere Halbleiter-Quantenpunkte besonders vielversprechende Kandidaten, da sie diskrete elektronische Übergänge mit direkter elektrischer Anregbarkeit verbinden. Das mit Abstand meist-untersuchte System im Bereich der Halbleiter-Quantenpunkte wiederum sind InAs-Quantenpunkte auf GaAs-Substrat, da hier eine einfache Integration in optische Mikrokavitäten möglich ist. Für die Anwendung ist das ein wichtiger Punkt, da auf diese Weise eine grössere Photonenausbeute, eine verbesserte Direktionalität sowie eine Beschleunigung der Ausstrahlung erreicht wird.

Die Mehrzahl der Studien über Ein-Photonen-Quellen auf Basis von Quantenpunkten beschränkt sich bis heute auf solche mit Emissions-Wellenlängen unter 1000nm. Eine Anwendung in der Glasfaser-gestützten Telekommunikation erfordert aber Wellenlängen nahe 1300 nm bzw. 1550 nm, da die Absorptionsverluste in den üblichen Silika-Fasern hier minimal sind. Ziel dieser Arbeit ist es daher, eine Ein-Photonen-Quelle mit InAs-Quantenpunkten auf GaAs zu realisieren, die Licht bei einer Wellenlänge von 1300 nm ausstrahlt. Die Herausforderungen liegen dabei zum einen in der Epitaxie: die Quantenpunkte müssen gross sein, dürfen aber nur mit geringer Flächendichte aufgebracht werden. Die zweite Schwierigkeit ist die Einzel-Photonen-Detektion, da im nahen Infrarot auf Detektorsysteme mit geringer Quanteneffizienz und verstärktem Rauschen ausgewichen werden muss.

Der erste Teil der vorliegenden Dissertation behandelt die Epitaxie. Die hergestellten Quantenpunkte müssen von grossem Volumen sein, um eine hohe Emissions-Wellenlänge zu erreichen. Gleichzeitig müssen die Abstände zwischen den Quantenpunkten gross sein, um die spätere Isolierung zu erleichtern. Durch eine Optimierung der Prozessparameter konnte die Herstellung von Quantenpunkten von niedriger Dichte ($2 \cdot \mu\text{m}^{-2}$) und der geforderten Emissionswellenlänge (um 1300 nm bei einer Temperatur von 10 K) sowie einer sehr guten Grössen-Homogenität erreicht werden. Darüber hinaus wurden diese Proben hinsichtlich

ihrer optischen Charakteristika im Vergleich zu Quantenpunkten höherer Dichte untersucht. So konnte gezeigt werden, dass die niedrige Dichte keinen negativen Einfluss auf die Effizienz des Einfangs von Ladungsträgern in die Quantenpunkte hat.

Im zweiten Teil geht es um die spektroskopischen Eigenschaften der Quantenpunkte unter optischer sowie elektrischer Anregung. Die niedrige Dichte und ein optimiertes Detektionssystem ermöglichten die spektroskopische Untersuchung einzelner Quantenpunkte, was anhand der Spektren gezeigt werden konnte. Mithilfe eines Anti-Korrelations-Experimentes konnte ausserdem nachgewiesen werden, dass es sich hierbei um die Emission einzelner Photonen handelt. Zusätzlich präsentieren wir erste Messungen von einzelnen Quantenpunkten, die in eine dreidimensionale Mikrokavität eingebettet wurden.

Abschliessend werden die Fabrikation und Charakterisierung von Lichtemittierenden Dioden (LED) auf Basis einzelner Quantenpunkte präsentiert. Die elektrische Anregung stellt zusätzliche Anforderungen besonders an die Prozessierung und in bezug auf die Ladungsträger-Diffusion. Verschiedene Designs der LED-Strukturen wurden realisiert, die Resultate und Etappen werden diskutiert. Die Elektrolumineszenz einzelner Quantenpunkte unter elektrischer Anregung konnte schliesslich beobachtet werden.

1

Introduction

In the last decades, continuous efforts have been devoted to the miniaturization of electronic devices. This progress led scientists to study objects with nanoscale dimensions for which quantum confinement effects occurs. Among such “nanostructures”, quantum dots (QDs) have attracted much interests since they offer the prospect of temperature-independent ultralow-threshold lasers [Arakawa 82]. Next, the emergence of the field of quantum information and the development of quantum protocols for optical transmission of cryptographic keys revealed a new possible application of QDs as source of single photons. This work has been carried out in the framework of research of a reliable single photon source emitting in the 1300 or 1550 nm transmission window of optical fiber. After a summary of the different applications of a single photon emitter, an overview of various physical systems demonstrated as single-photon sources will be given. Advantages and drawbacks of QDs will be detailed. We will insist on our motivation concerning the choice of the QD system, and expose the outline of the manuscript.

1.1 Single photon emitter

A single photon source is a light source able to emit on demand a pulse consisting of only one photon. Up to know very few experiments relying on single photons have been realized. Since the main application of single photon sources is at the moment quantum cryptography, we will briefly summarize its principle.

1.1.1 Applications

Applications of single photons are based on the encoding of bits (called quantum bit or qubit) by single photons. In contrast to a classical bit, a qubit is a linear superposition of the basis states $|0\rangle$ and $|1\rangle$.

Single photons can be used to encode a secret key in a quantum cryptography system. In the cryptography protocol defined by Bennett and Brassard (BB84), the encoding is done on the polarization of a single photon [Bennett 92]. The principle uses the fact that a quantum measure disturbs the state of the measured qubit to detect a possible eaves-dropper.

Two conjugate basis are used for the polarization of the photons: normal (\longrightarrow or \uparrow) or 45° polarized (\nearrow or \searrow). Let's assume for instance that 0 bit is encoded by 0° or 45° polarized single photons and 1 bit is encoded in 90° or 135° polarized single photons.

Experiment involves three characters: The sender (Alice), the receiver (Bob) and an eaves-dropper (Eve).

Alice emits a series of random bits encoded by single photons in one of the two polarization basis. The basis is chosen randomly for each bit. If the receiver (Bob) analyzes the photons with the same basis as Alice, he will observe the same bits series as Alice. But in fact he has 50% probability to choose the other one (Figure 1.1). In that case, he has 50% probability to measure the wrong bit value. After exchanging the bits, Alice and Bob exchange the basis they employed to emit and detect the photon using a conventional communication channel. Statistically, only 50% of the measurements were done in the same basis and will be kept. These bits can then be used as secret key.

If an eaves-dropper tries to intercept the communication by measuring the photon sent by Alice and then creates copies to reinject in the communication channel, the situation changes. As for Bob, Eve has 50% chance to choose the correct measurement basis. Then for a photon emitted by Alice and measured by Bob in the same basis, there is a 50% probability that Eve decodes and reinjects wrongly the photon and thus, 25% possibilities that Bob measures a wrong bit instead of a null probability without Eve's presence. By comparing (on a public channel) a part of the bits of the key, Alice and Bob can observe an anomalous error rate and thus detect that they have been eaves-dropped.

We note that these experiments are very interesting in the context of free-space quantum cryptography however they present some limitations over distances of more than a few kilometers of optical fiber: polarization conservation in long optical fiber is difficult due to decoherence phenomena. Other quantum cryptography schemes can thus be used, using in

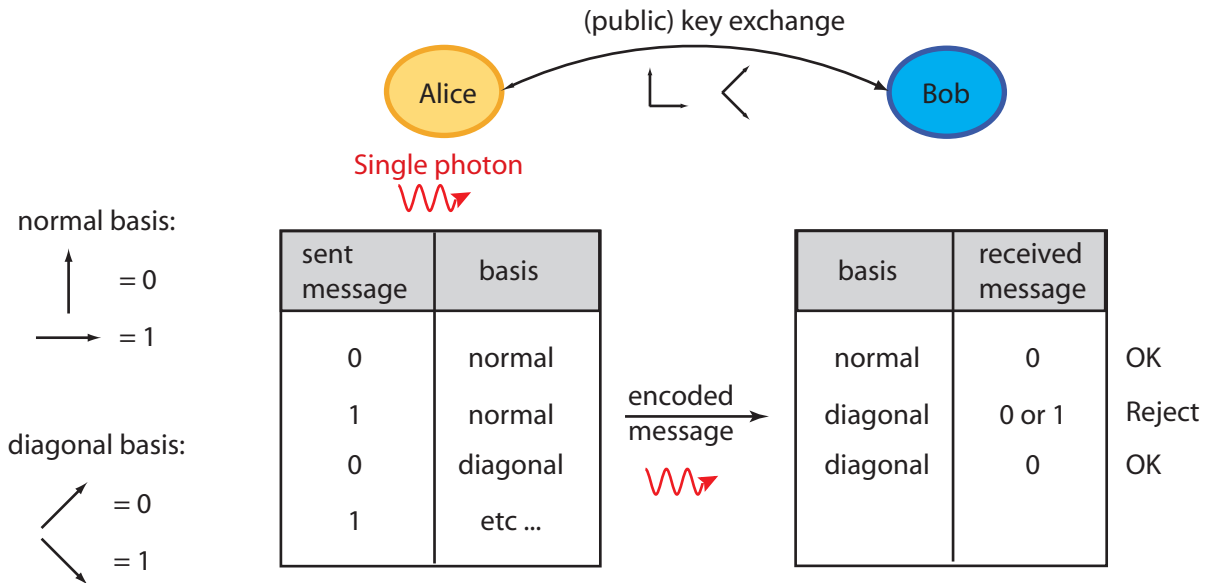


Figure 1.1: Scheme of principle of a quantum key distribution: qubits are encoded by single photons emitted in a random polarization basis. The photons are detected with another random polarization basis. Series of basis is then exchanged via a public communication channel and bits exchanged using the same basis are used as secret key.

particular phase encoding [Zbinden 97]. The main limitation to quantum cryptography is that the signal can not be amplified as for a conventional communication system because this would introduce some errors (on the basis of the no cloning theorem [Wootters 82] it is not possible to produce a copy of a quantum system, in particular a polarized photon). Losses in optical fiber should then be minimal so that secure communications can occur over long distances. As we can see on the figure 1.3, attenuation of transmission in optical fiber is minimum for an emitter at 1300 nm and 1550 nm.

In the longer term, another conceivable application of single photon source can be found in the quantum computing domain. In 2001, Knill *et al.* [Knill 01] proposed a quantum computation scheme based on linear optics and on single-photon emitters. An optical system (for example using a beam splitter [Santori 01]) can realize a quantum logic gate which constitutes the basic block for quantum computation. This requires a source of coherent single photons.

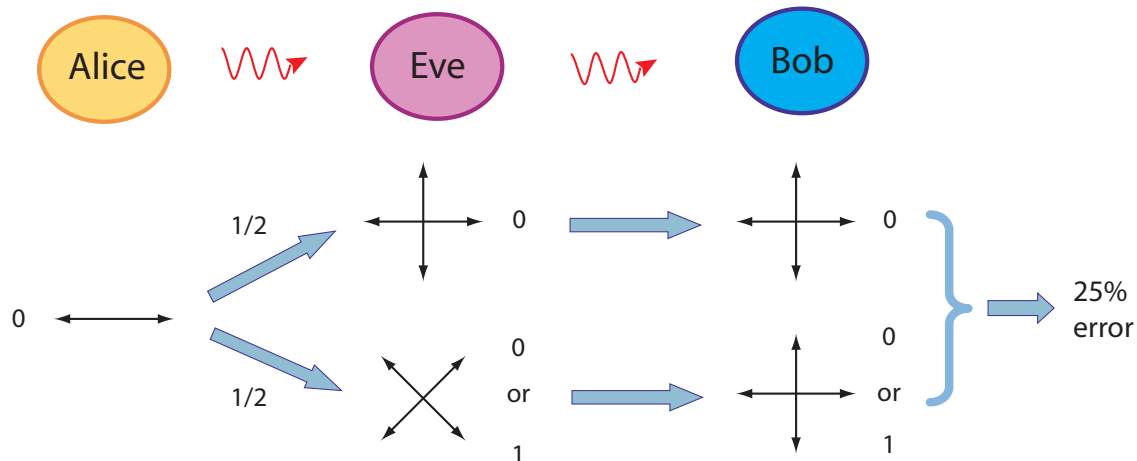


Figure 1.2: Example of a situation where Bob and Alice have the same polarization basis. The presence of Eve increases by 25% the error rate in Bob measurements.

1.1.2 Different types of single photon sources

Attenuated laser

The experiments of quantum cryptography are usually based on weak coherent pulses as light emitter with a low probability of containing more than one photon [Buttler 98, Stucki 02]. Most of the pulses will contain zero photons but since coherent light (such as laser light) is poissonian, the probability to have two photon per pulse is not zero. This permits an eventual attack from an eaves-dropper [Huttner 95] in particular the *photon number splitting* (PNS) attack [Brassard 00]: Without changing photon polarization Eve can determine the photon number of each pulse. For pulses containing 2 photons, she kept one and send the other one to Bob. When receiving the data regarding the basis, Eve measures her photon and obtains full information. Each signal containing more than one photon in this way will yield its complete information to an eavesdropper without leading to errors in the sifted key. The situation becomes worse in the presence of loss, in which case the eavesdropper can replace the lossy channel by a perfect quantum channel and forward to Bob only chosen signals. This suppression is controlled such that Bob will find precisely the number of nonempty signals as expected given the lossy channel. If there is a strong contribution by multiphoton signals, then Eve can suppress the single photon signals completely, to obtain full information on the transmitted bits. Of course, in the realistic case, perfect quantum channel does not exist and detection techniques do not allow such attacks, however, it shows

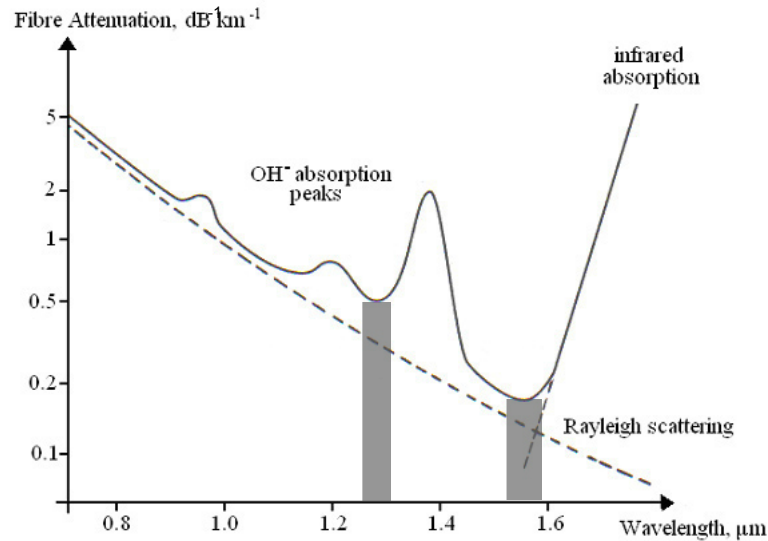


Figure 1.3: Spectral attenuation profile in a silicon fiber [Shahimin 04]

that attenuated laser are not a solution on its own. The strong attenuation, required to limit multiphoton pulses, limits the effective single photon generation efficiency and reduces the transmission range by increasing losses which are also a source of insecurity. A “real” single photon source would enhance the secured transmission range and the bit rate since it will be limited only by transmission losses.

Atoms and Molecules

A two-level system excited by an optical pulse much shorter than its lifetime can only emit a single photon. The first experiment showing the emission of photons one by one was done in 1977 by Kimble et al. by measuring resonance fluorescence from sodium atoms [Kimble 77]. The advantages of this system are that all atoms of a given isotope are exactly indistinguishable, and there is no variation in the emission properties from atom to atom. In order to direct the single photon emission efficiently into a single mode, experiment holding a single atom [McKeever 04, Kuhn 02] or single ion [Maurer 04] cooled and trapped into a high finesse cavity have been done. However this required complex setups, which are not practical for integration into larger systems.

Single organic molecules can be handled more easily than single atoms, by incorporating

the molecules as dilute impurities in a crystalline host [Basché 92]. Their emission is efficient even at room temperature, the light extraction and collection efficiency can be very high since high numerical aperture microscope objectives can be used to collect the fluorescence and molecules are usually imbedded in low-refractive-index materials. Molecules emitting at all wavelengths from the UV to the IR are available. However molecules generally suffer from photobleaching, i.e. the molecules stop emitting light after a certain amount of active time [Ambrose 94]. Furthermore, it remains difficult to isolate spatially a single molecule and to implement this system into a tridimensional microcavity [Lounis 00].

Another alternative is to use nitrogen-vacancy (NV) centers in synthetic diamond crystal as the optical emitters. These defects consist of a substitutional nitrogen atom with a vacancy at an adjacent lattice position, and can be created with a controlled density by electron irradiation followed by annealing in a nitrogen environment. NV center can be considered as a three-level system (due to the presence of metastable shelving states), and avoid the problem of photobleaching [Gruber 97]. Antibunching has been shown at room temperature, and isolation of a single emitter is easier than with the precedent methods. One of the drawbacks is a broad spectral emission (~ 120 nm), in the visible range [Kurtsiefer 00] which increases the spatial dispersion and the attenuation in fibers. Moreover, the integration of the emitters into devices is not practical and the rather long radiative lifetime of the order of 10 ns, limits the maximum single-photon-emission rate.

Finally, a single photon device has been realized using mesoscopic quantum well [Kim 99]. It is based on the tunnelling of electrons and holes one-by-one in a GaAs/AlGaAs double-barrier mesoscopic p-i-n heterojunction driven by an alternating voltage source, exploiting the Coulomb-blockade effect. However this required an operation temperature below 50 mK and no photon correlation measurements were performed to confirm single-photon generation.

The work presented in this thesis is related on another kind of single photon emitter, based on semiconductor quantum dots. Characteristics of such nanostructures are detailed in the following paragraph.

1.2 Self-assembled quantum dots as single photon emitters

1.2.1 Quantum confinement

A quantum dot (QD) is a nanostructure in which carriers are confined to a volume whose dimensions are of the order of nanometers. As the carrier de Broglie wavelength is comparable to nanostructure dimensions, size quantization effect becomes significant. Confinement is realized by using two materials with different band gap energies. Carriers are trapped in the low-bandgap material by the effective potential well. This has been first used to confine matter in 2 dimensions (Quantum Well), then in 1 dimension (Quantum Wire) and 0 dimension (Quantum Dots). Solution of Schrödinger equation in case of carrier localization in all three dimensions results in a discretization of electronic levels. The density of state exhibits a δ -function-like (figure 1.4) which explains why quantum dots are often called “artificial atoms”. Optical transitions between the valence band and the conduction band can thus occur only at discrete energies. Then, an electron-hole pair injected into the QD can recombine emitting a single photon, and no further photon emission is possible before another excitation is provided. When excited in continuous-wave, the system behaves as a “photon-dropper”, and by a periodically pulsed (optical or electrical) excitation, a stream of single photons is generated. Practically, the injection of a single electron-hole pair can not be controlled, and several electron-hole pairs are present in the QD, however, because of the Coulomb interaction among the strongly confined electron-hole pairs, the emission frequency of each transition depends strongly on the number of carriers in the dot. This means that the emission arising from the last electron-hole pair occurs at a distinct frequency, so that spectral filtering readily permits isolation of the single photon emitted by a single quantum dot at the end of its radiative cascade when it contains a single electron-hole pair [Moreau 01b].

The fabrication of quantum dots has changed with the development of epitaxial techniques. In 1970’s, quantum dots were created by patterning quantum wells using nanoscale lithographic techniques. In 1980’s it was found that quantum dots could be grown directly during the epitaxy by strain-induced process which simplified considerably their fabrication process.

Quantum dots have also been made in colloidal solutions. Colloidal II-VI nanostructures have been studied for a long time: they are used in the commercial production of colored and photochromic glasses. These dots are still the subject of intense studies; easy and cheap

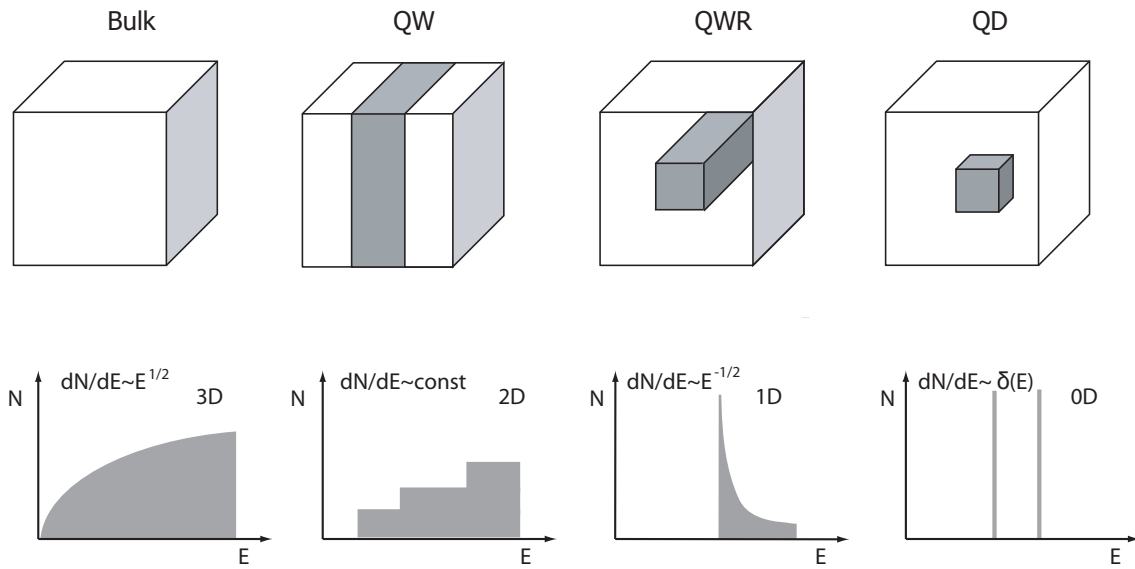


Figure 1.4: Density of states for charge carriers in structures with different dimensionality (D) : Bulk material: 3D, Quantum Well (QW): 2D, Quantum Wire (QWR): 1D, Quantum Dot (QD): 0D

to fabricate, they are however difficult to incorporate into larger semiconductor structures. They can easily be used at room temperature but present also blinking phenomena.

1.2.2 Advantages and drawbacks

Quantum dots offer several advantages as a source of single photons. First, the quantum efficiency is high and the radiative lifetime is short (~ 1.2 ns) as compared to NV center (~ 20 ns) or CdSe/ZnS nanocrystals (~ 32 ns). Quantum dots do not suffer from bleaching and are stable even after several temperature cycles. Finally they can be easily inserted in a microcavity which will modify their emission characteristics. The main drawbacks are that up to now low temperatures have been required to operate the devices. Interaction with phonons gives rise to a broadening of the emission lines [Matsuda 01] so that it is not possible to spectrally filter them separately and the background signal becomes also important. Moreover their inhomogeneity in size varies the wavelength emission from one QD to another one: in a larger QD, confinement energy is higher and single photon will be emitted at longer wavelength. This is a problem for the measurement reproducibility and for the coupling into cavities.

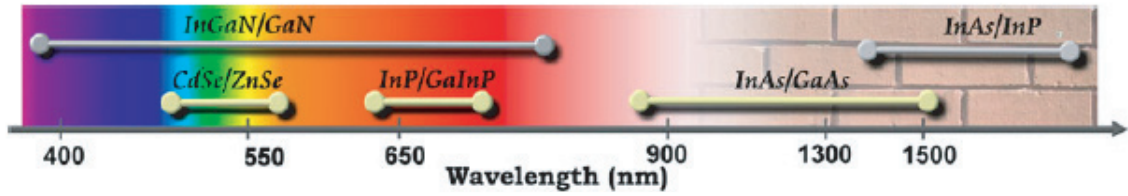


Figure 1.5: Schematic representation of the wavelength ranges accessible with different Stranski-Krastanov quantum dot material systems. The region inaccessible to silicon detectors is indicated by a brick wall [Zwiller 04].

1.2.3 Single photon generation with single quantum dots: overview

The colloidal QDs were the first type of QDs used to generate single photons [Michler 00a]. In figure 1.5, we show a schematic representation of the wavelength emission ranges for several Stranski-Krastanov quantum dot-material systems. Up to now, single-photon generation has been achieved with the InAs/GaAs, InP/GaInP and CdSe/ZnSe quantum-dot systems.

CdSe quantum dots in ZnSe have been used to generate single photons at around 500 nm [Sebald 02]. This material system presents a short radiative lifetime as compared to III-V quantum dots, and a larger energy splitting between the exciton and the biexciton than for the InAs/GaAs material system. This larger splitting is useful to achieve a better filtering of the exciton emission, making operation at higher temperatures possible. The refractive index of ZnSe is lower than for GaAs, making the light extraction easier however their emission wavelength are not compatible with a transmission in fiber.

InP dots in GaInP have been used to generate single photons in the 640-690 nm range [Zwiller 03] which corresponds to the maximum efficiency of silicon avalanche photodiodes, a detection efficiency in excess of 70% can be reached around 650 nm.

InGaN quantum dots imbedded in GaN present the strong advantage to potentially cover the complete visible range. Moreover it possesses high exciton binding energies. Single dot emission has been recently studied [Robinson 05, Moriwaki 00, Martin 05].

InAs dots imbedded in InP can be used to generate single photons at 1550 nm, where optical fibres have their lowest absorption. However, integration of such QDs is a micro-cavity structure with AlGaAs/GaAs Distributed Bragg Reflectors (DBRs) is difficult due to the high lattice mismatch between InP and GaAs material. Microphotoluminescence experiments on single QD have been done recently [Miyazawa 05, Takemoto 04, Saint-Girons 06a].

The InAs/GaAs system is by far the most studied of all quantum-dot systems since InAs/GaAs material can be easily embedded in a microcavity. This is the system studied in this document. At the beginning of this thesis, most of the reported works has been done on InAs QDs emitting in the 900-950nm range [Michler 00b, Santori 01]. The research performed in this thesis led to obtain single-QD emission [Alloing 05] and single-photon experiments [Zinoni 06] at 1300nm as well as evidence of single QD emission through electrical excitation [Monat 06]. It takes place among the few experimental demonstrations published in this field [Kaiser 02, Ward 05].

1.3 Outline of the manuscript

The realization of a single photon emitter from InAs/GaAs self-assembled quantum dots emitting at 1300 nm represents a challenge for the growth side first, since it requires a low areal density (to make the isolation of a single QD easier) and a long emission wavelength. Second, the single photon detection technology for the near infrared is still in its infancy and noise levels, quantum efficiency and temporal response are considerably poorer when compared to the single photon detection modules operating below 1000nm. These difficulties will be evoked in this manuscript which is organized as followed:

In the second chapter, the different experimental methods used in this work will be presented. It includes the description of growth, processing, structural and optical characterization techniques.

The third chapter is focused on the MBE growth optimization of QDs whose characteristics are adapted for an application as single photon sources. Influence of the different growth parameter will be detailed, structural characterizations of the QDs will be presented.

The fourth chapter concerns the optical characterization of QD ensembles. Carrier recombination processes and evolution of the emission of low-density QDs at different temperatures will be studied as compared to the emission of higher-density QDs.

The fifth chapter shows the results obtained with single QD spectroscopy. Discrete transitions of a single QD are clearly observed at 1300nm, results of antibunching experiment are presented. We also explain the influence of a three-dimensional microcavity environment on the spontaneous emission of a light emitter through the Purcell effect. Preliminary results on QDs embedded in a micropillar and a photonic crystal structure are reported.

Finally the last chapter concentrates on the realization of single quantum dot light emitting diode (LED). Single photon emission under electrical injection is thus essential for

the practical application of single photon devices. However, diffusion carriers and current spreading give additional problems as compared to the optical excitation. An optimized design of the device is then required to restrict the current injection and/or selectively collect the emission from a single QD. Different LED structures have been tested, emission from discrete levels will be demonstrated. In the end, the realization of a three-dimensional microcavity LED will be reported.

This work benefited from the collaboration with the following laboratories:

Laboratoire de Photonique et de Nanostructures, Marcoussis, France (G. Patriarche) for the transmission electron microscope measurements.

Laboratoire Photonique sur Silicium, Grenoble, France (L. Grenouillet) for the micropillar fabrication.

Institute of Photonics and Nanotechnology, Roma, Italy (L. Lunghi, A. Gerardino, M. Francardi) for the processing requiring e-beam lithography, as well as for the photonic crystal cavity study.

Finally, the characterization of single QDs and cavities under optical pumping described in chapter 5 was performed by C. Zinoni and L. Balet in the framework of their thesis work at EPFL. Electroluminescence measurements on LEDs in chapter 6 were carried out in collaboration with Dr. C. Monat, postdoctoral scientist at EPFL.

2

Experimental Techniques

In this chapter we will present the experimental methods applied as well as the details of the setups. Growth technique and structural characterization tools will be explained, followed by fabrication techniques used for single quantum dot devices. Finally, experimental setups for optical characterizations will be presented.

2.1 Epitaxy with molecular beam epitaxy (MBE) system

2.1.1 Principle, advantages and drawbacks

MBE technique has been developed in the early 1970's by the Bell laboratories. This method consists in the interaction of atomic or molecular flux in a chamber with ultra-low residual pressure (below 10^{-10} Torr). These fluxes are issues from evaporation cells oriented toward a monocrystalline substrate. Knudsen relation expresses the flux Φ as function of partial pressure P , atom mass m and material temperature T :

$$\Phi = \frac{P}{\sqrt{2\pi mk_B T}}$$

with k_B is the Boltzmann constant. Under these conditions, the atomic mean-free path is larger than the distance between the source and the substrate. Substrate is heated to a convenient temperature so that atoms can be adsorbed. Atomic layer by atomic layer, deposition is achieved by using low beam flux: typical growth rates of 0.1-1 $\mu\text{m}/\text{h}$ are obtained. A uniform growth is obtained by rotating the substrate during the deposition.

MBE method is specially adapted to thin film deposition, the main advantages of this technique are the following:

- a high quality of deposited material due to the ultra high vacuum in the chamber,
- abrupt interfaces between films with different materials are allowed by shutter systems in front of the sources. Diffusion at the interfaces is also limited by the low substrate temperature,
- a high control of the growth rate by varying the cell temperature,
- a possible realization of concentration profile specially for doping,
- a possible *in-situ* monitoring of growth conditions and growth rate by using reflection high-energy electron diffraction (RHEED), laser reflectometry, or other methods thanks to the ultra high vacuum conditions.

The main drawbacks are:

- a lateral inhomogeneity of the deposited layer due to the geometry of atomic and molecular flux. This limitation had to be taken into account in our MBE system however progress in MBE chamber conception enables to reach now a high surface homogeneity in recent industrial systems.
- a long and periodic maintenance due to the complexity of the system and the ultra high vacuum environment.

2.1.2 III-V growth with VG 80 system

The solid-source MBE VG 80 system at EPFL consists in 4 vacuum chambers (figure 2.1): two growth chambers connected via a transfer chamber, and a load lock to bring samples into and out of the vacuum environment while maintaining the vacuum integrity of the other chambers. The both growth chambers are nearly identical except that one is equipped with two In cells. This is the one that will be used for the work reported here. Ionic pump system together with cryopanel in the growth chamber allow to keep a vacuum as high as 10^{-9} mbar when cells are heated at working temperature. Representation of a MBE growth chamber and a typical effusion cell is presented on the figure 2.2.

The growth chamber contains III-element effusion cells (Al, Ga, two In cells), Be and Si cells for doping, and an As cell with cracker and valve to control V-element flux: the

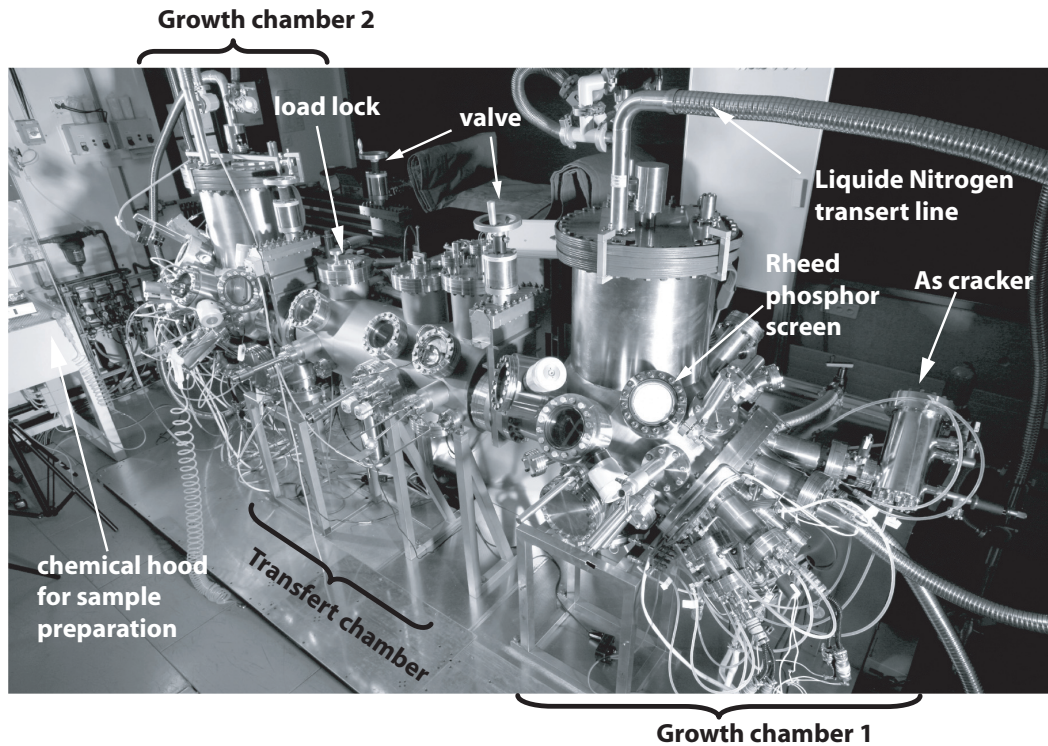


Figure 2.1: MBE VG 80 System (picture by A. Herzog). Two growth chambers are connected through a transfer chamber. High vacuum is realized by an ionic pump system. Samples presented in this thesis have been grown in the growth chamber 2 which contains two Indium cells.

cell is charged by solid As, which is thermally evaporated in As_4 molecules. Cracker allows to separated them in an As_2 flux. The substrate temperature is monitored by an optical pyrometer facing the sample surface. Sample is fixed on an holder which rotates during the growth to enhance the layer uniformity. For growth process the holder is flipped from the loading position so that sample faces the material sources. The holder also has an ion gauge mounted on the side opposite the sample which can read the chamber pressure, or be placed facing the sources to measure beam equivalent pressure (BEP) of the material sources.

Growth of III-V alloys is based on the three temperatures method proposed by K.Günter in 1958. Substrate temperature T_S is intermediate between evaporation temperature of III elements, T_{III} , and the sublimation temperature of V elements, T_V : $T_{III} > T_S > T_V$. This allows III element atoms to be condensed on the substrate with a small re-evaporation

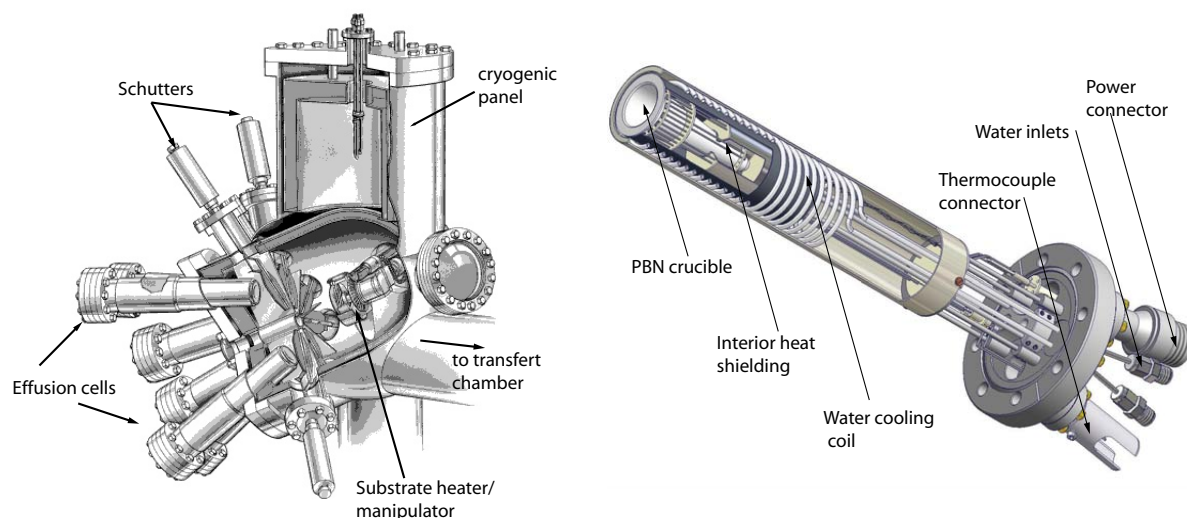


Figure 2.2: Representation of (a) an MBE chamber (b) a 30cc Veeco® Ga cell.

rate. Furthermore, an excessive proportion of V-element atoms during the growth results in the control of the stoichiometry: atoms which are involved in boundaries with III-elements participate in the growth, the others are desorbed. Thickness and growth rate of the III-V layer depend only on III-element fluxes.

Prior to the growth, GaAs substrates are mounted on molybdenum supports and introduced into the loading chamber where they are degassed for one night at 110°C . Then, they are introduced into the preparation chamber. One substrate is then heated for one hour at a temperature around 350°C before to be led into the growth chamber. Substrate is then heated under As overpressure, until 600°C in order to remove the protective oxide layer on its surface. Then a 500 nm-thick GaAs layer is deposited at 620°C in order to obtain an optimal surface quality before the growth of the structure.

2.1.3 Growth rate measurements

Calibration of the growth rate is essential for proper tuning of resonant-cavity devices. One way to measure the growth rate is to use the BEP gauge. The BEP reading is proportional to the flux at the sample surface and hence the growth rate. This technique does not require to grow any epitaxial layer but it does not give a direct measure of the growth rate, so some other in-situ (for example RHEED oscillations, as detailed in the next paragraph) or ex-situ

methods (X-ray diffraction measurements for example) must still be used to relate BEP to a growth rate. Furthermore, resolution of the gauge is only of several percent and is too small to measure very low growth rates. In the following RHEED oscillations and measure of the 2D-3D transition time have been used to estimate the growth rate for 2D layer deposition and QD growth, respectively.

2.2 In situ characterization: RHEED

2.2.1 Principle

Reflection high energy electron diffraction (RHEED) technique is based on the reflection and diffraction of an electron beam on the sample surface. An electron gun produces high energy electron flux ($\sim 10\text{keV}$) which is reflected with a very small angle ($1\text{-}3^\circ$) on the sample surface and strikes a phosphor screen. It forms a pattern consisting of a specular reflection and a diffraction figure. A camera monitors the screen and records instantaneous pictures or measures the intensity of a given pixel as a function of time. The de Broglie wavelength of the incident electron, between 0.17 and 0.006 Angstrom, is on the same range as the lattice dimension. Due to the small incident angle, electron penetration length is limited to the first atomic layers of the substrate. Resulting diffraction figure is thus only sensitive to the surface and not to the volume of the sample and can give information on the morphology of the surface, in real time so that growth parameter can be changed during the growth.

2.2.2 Characterizations

During this thesis, RHEED technique has been used to calibrate the growth rate and the substrate temperature, to observe removal of oxide from the surface, and to determine the proper arsenic overpressure. Indeed, analysis of RHEED pattern provides a large amount of information on the following properties:

The surface quality: The diffraction diagram corresponds to the intersection of the reciprocal lattice of the substrate with the Ewald sphere (figure 2.3). Ideally the diffraction figure is constituted of points. However, the angular and energy dispersion of the electron beam combined with an unperfect surface leads to a diffraction figure showing streaky lines. Finally the diffraction figure becomes “spotty” if small corrugations are formed on the surface.

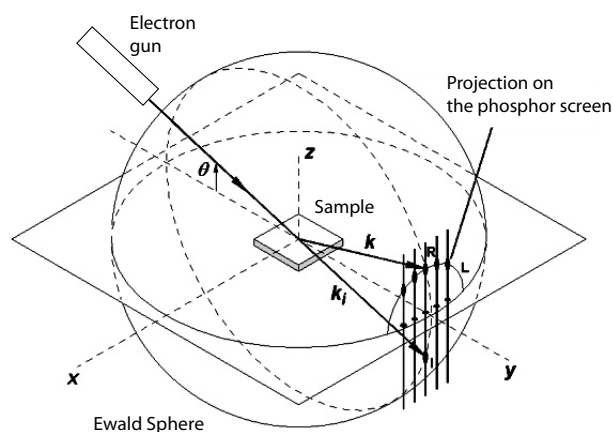


Figure 2.3: RHEED diffraction figure: Intersection between electron beam reflected on the sample surface with a small angle $\theta < 3^\circ$ and Ewald sphere [Boschetti 00].

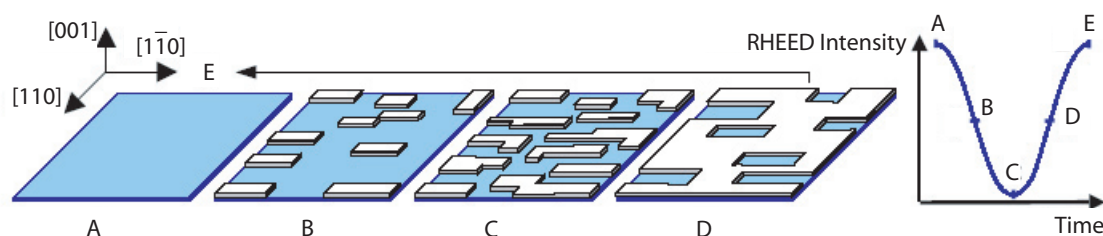


Figure 2.4: RHEED oscillations principle. The intensity variation of the specular spot is function of the surface reconstruction state [Panish 93].

Composition and thickness of 2D layer: During growth of two-dimensional layer, we observe that the intensity of diffraction lines oscillates. When a complete layer is deposited, interferences become constructive and a maximal intensity is observed. When an half layer is formed, the intensity is minimal. We obtain intensity oscillations with a period corresponding to the formation time of one monolayer as shown on the figure 2.4. The growth rate can then be deduced.

The spacing between diffraction lines depends also on the lattice parameter of the deposited material. Nature of the growing material can then be deduced from the diffraction figure.

Observation of 3D growth dynamic: QD appearance can be observed when diffraction figure change from dotted lines to “spotty” figure. Information on the shape of the QDs can be deduced from the “chevron” pattern, which results from the diffraction on the island facets [Lee 98]. Furthermore, the observation of specular spot intensity can

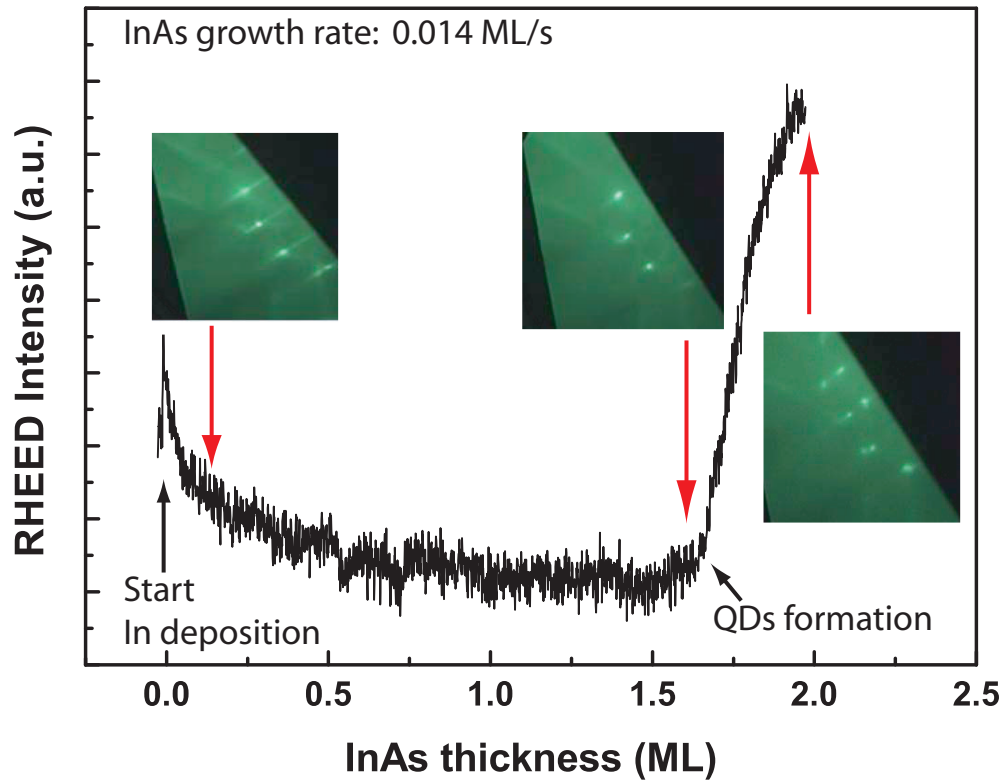


Figure 2.5: Variation of specular intensity with InAs deposition thickness as measured on our system. Intensity increases abruptly when QDs start to be formed. The 2D-3D transition is observed with the change of diffraction figure on RHEED screen.

give information on the formation dynamic of QDs: As shown on the figure 2.5 the spot intensity increases abruptly after 2D-3D transition. Finnie et al. [Finnie 02] have shown that the spot intensity can also be related to the quantum dot volume. More precisely, by leaning on the mean-field theory [Dobbs 97], Song et al. [Song 06] have shown that kinetic mechanisms of the QD formation and the QD disappearance can be investigated from the evolution of the spot intensity during the 2D-3D transition.

RHEED technique thus appears very useful for in-situ monitoring of the growth and is a strong advantage for the MBE epitaxy.

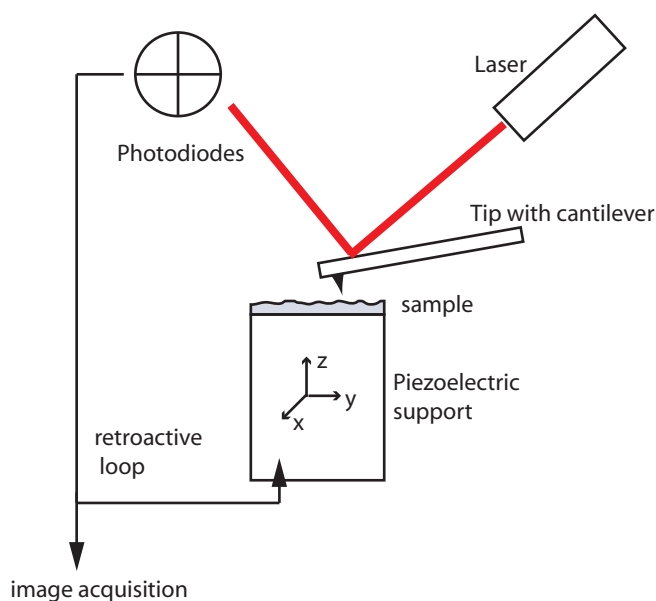


Figure 2.6: Scheme of the AFM principle. Retroactive loop is used to keep a constant distance between tip and surface.

2.3 Structural characterization by AFM

Atomic force microscopy (AFM) technique has been invented in 1986. It allows a tridimensional topographical analysis of a surface with a lateral and vertical resolution of few nanometers. This method measures the interaction forces between atoms on the sample surface and a tip fixed on a cantilever. The tip scans the sample surface fixed on a piezoelectric support. Surface roughness leads to a variation of interaction forces and then, to a variation of the distance between the tip and the surface. In order to maintain this distance constant, cantilever bends. The bending is registered by the reflection of a laser beam on the cantilever. The signal is detected by four photodiodes connected to a numerical acquisition system. The scheme of the AFM principle is shown on the figure 2.6.

Resolution of this method is appropriate to study nanostructures such as self-assembled quantum dots. Nevertheless, this method contains some limits that must be taken into account:

- It requires that QDs are uncapped. Now, it has been observed that QD shape changes before and after capping layer deposition. Abrupt cooling process of the sample after QDs deposition are used to freeze the surface but this does not prevent an eventual post-growth QD evolution. AFM is thus more useful for a comparative analysis (between samples cooled down using the same cooling process) than for quantitative

measurements of QD dimensions.

- The physical resolution is limited by the tip shape, and QD dimensions can be distorted by a blunted tip. Measurements need then to be interpreted cautiously, and if necessary to be confirmed by TEM investigations. Recent progress have been done about AFM resolution by sticking a carbon nanotube at the tip extremity [Seo 03].

In the following, AFM has been used to study the evolution of QD density depending on growth conditions. Just after the QD appearance, the substrate temperature was immediately cooled down ($80^{\circ}\text{C}/\text{min}$), the sample is kept under an Arsenic overpressure (till 350°C) before being taken out of the growth chamber.

2.4 Processing techniques

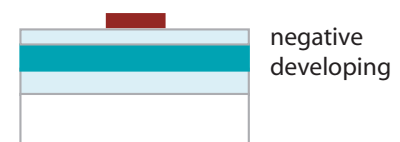
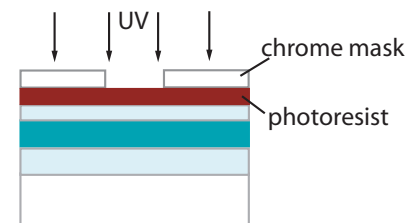
After the growth of the epitaxial structure, a patterning of the surface is required to fabricate microcavities with high extraction efficiency or single photon light emitting diodes. In the following, different steps of the device fabrication are detailed.

2.4.1 Sample masking

Photolithography

This technique is used to transfer a pattern on a photomask onto the sample. First the sample is spin-coated by a photo-sensitive thin layer (photoresist). A suitable photoresist is the Shipley AZ5214E, which can be easily removed by solvents. Its resolution is around $0.1\ \mu\text{m}$. Spinning at 500 rpm during 30 sec yields a $1.3\ \mu\text{m}$ thick layer. After drying on a plate at 90°C for 5 min, the photoresist film is exposed to UV light (Mercury light emitting at 365-405 nm), locally shadowed by a chrome mask. Exposed part are then removed by developing (positive photoresist). Developer MF319 has been used. Using the same resist, a negative process is possible (masked part are removed by developing) if the coated sample is heated after exposition,

Original sample :



for 2 min at 115°C and then re-expose to UV light for 60 sec without mask.

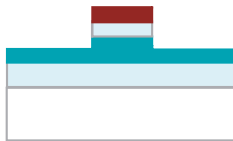
Oxygen plasma

O₂ plasma is used to remove polymerized photoresist residues or other organic components. After developing the UV exposed structure of photoresist, a 60 W plasma at 800 mTorr is performed for 1 min. At the end of each processing step, the sample is cleaned with acetone and a 80 W plasma at 800 mTorr for 2 min.

2.4.2 Mesa etching

Removing material from the wafer surface can be used to realize optical or carrier confinements, to contact a buried layer, or to eliminate a sacrificial layer. Two different etching techniques are employed.

Dry etching by reactive ion etching



vertical sidewalls by RIE

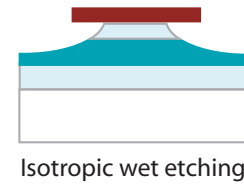
Reactive ion etching (RIE) involves both a reactive chemical process and a physical process using ion bombardment. Cl₂, SiCl₄ and Ar as etching gases have been used. In a low pressure chamber, where sample has been introduced, an RF power is applied between two electrodes. The sample is mounted on one of these electrodes (the cathode). The RF field creates a plasma of the inserted gaz. A DC self-bias develops on the cathode and the wafer acquires a large

voltage difference with respect to the plasma. This condition creates directionality for the ionized species moving towards the wafer. The extremely reactive ions etch the wafer anisotropically. This results in vertical sidewalls.

Wet etching

Another etching technique using only a reactive chemical process is wet etching. This is done by dipping the sample into a liquid etchant. In contrast to RIE etching, etched sidewalls are not vertical but oblique or isotropic, depending on the etching solution and on the nature and the crystallographic orientation of the etched material. Also the etching rate depends strongly on the material being etched.

This method is suitable for selective etching and when oblique etching profiles are required. But this technique is not always reproducible since etching rate is very sensitive to the composition and homogeneity of the etchant.

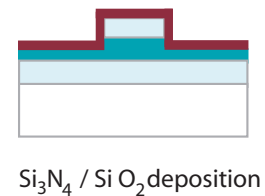


2.4.3 Isolating layer

To restrict current injection in a small region, an isolating layer has to be created above this region, in between the sample surface and a metal contact. This has been done in two ways:

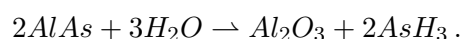
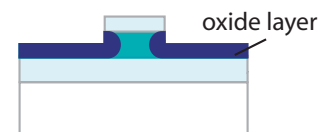
Plasma enhanced chemical vapor deposition (PECVD)

Dielectric layers like Si_3N_4 or SiO_2 are deposited on the surface by reaction of plasma-activated precursors on the surface of the heated sample. SiH_4/N_2 2/98% reacts with NH_3 or N_2O gases for Si_3N_4 and SiO_2 deposition, respectively. Deposited rates are typically 25 nm/min at a plasma power of 100 W, a pressure of 1 Torr and a sample temperature of 300°C . The dielectric layer can be locally etched by CF_4/O_2 plasma, using standard photoresist as a mask. At low power, photoresist does not polymerize, so it can be removed by acetone afterwards.



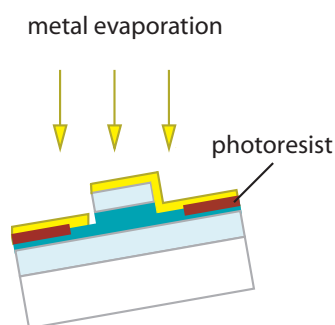
$\text{Al}_{1-x}\text{Ga}_x\text{As}$ oxidation

PECVD technique requires a masking of the sample to remove the isolating layer from the coated region. For very small structures ($\leq 4\ \mu\text{m}$), mask alignment is very critical. $\text{Al}_{1-x}\text{Ga}_x\text{As}$ oxidation is a self-aligned process and avoids this problem. Sample is introduced in a oven heated at 400°C in a H_2O atmosphere created by bubbling N_2 in a water bath at 85°C . The oxidation starts at the exposed surface following a chemical reaction which can be approximately described as



In general the final compound (after oxidation) is an AlGaOH oxide, with some remains of Gallium (depending on the starting composition) and hydrogen. The reaction rate is a function of $\text{Al}_{1-x}\text{Ga}_x$ composition. The oxide layer is used as electrical isolating layer, but we will see that it can also be used for optical confinement.

2.4.4 Contact deposition



The deposition of metals is done by e-beam evaporation of ultra-pure metal sources in an ultra-high vacuum chamber. A metal target is heated locally by an electron beam and evaporated on the sample. In order to deposit the metal locally on the surface, the sample is patterned by photolithography before the evaporation. To avoid any oxide layer which would affect metal adherence, sample is deoxidized in HCl|H₂O 1:1 solution for 30 sec before introduction in the chamber. After deposition, the resist is removed by solvents

together with the metal on top of it (“lift-off” process). In order to facilitate this last step or to increase metal adherence on mesa sidewalls, it can be useful to tilt the sample in the evaporation chamber, as shown on figure beside. It results in an inhomogeneous repartition of the metal layer on the sample surface.

2.5 Photoluminescence setup

2.5.1 Macro-photoluminescence

Photoluminescence (PL) measurements as function of excitation power and temperature has been used to investigate discrete energy levels of QDs. The experimental setup is sketched in figure 2.7. A continuous-wave Ti:Sapphire laser tuned to 800 nm excites electrons in the sample above the GaAs bandgap from the valence band to the conduction band and creates electron-hole pairs. The pairs recombine in the QDs and emit photons. Spontaneous emission is collected into a single multimode fiber and dispersed in a 1 m focal lens spectrometer equipped with a linear array of InGaAs detectors. At low excitation power, excitons are confined in the ground state level (GS) before recombination, and a single gaussian peak is observed. At higher excitation powers, excited states are getting filled which results in peaks at higher energy in the detected spectrum. For PL measurements which require high

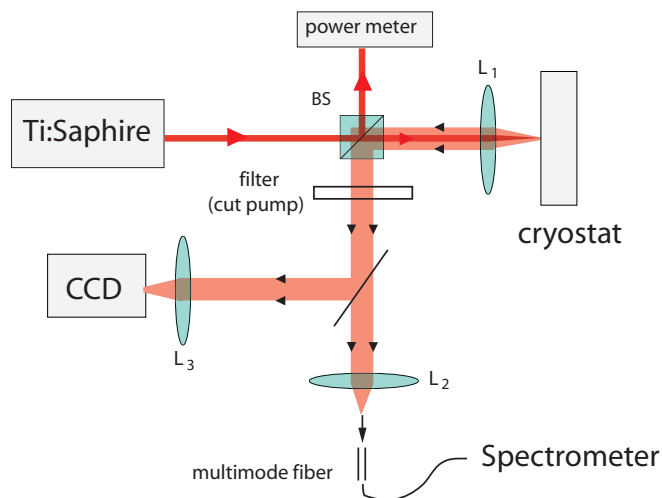


Figure 2.7: Sketch of the experimental setup used for PL saturation experiment and PL temperature-dependence experiment. Lens focal: $L_1=38$ mm, $L_2=25$ mm, $L_3=300$ mm.

excitation density, an objective was used to focus the beam to a $\sim 7 \mu\text{m}$ spot. Spot size was estimated by imaging the circular spot on a CCD camera. To study the evolution of luminescence efficiency with temperature, the sample was excited homogeneously by a large spot with low areal excitation density.

2.5.2 Micro-photoluminescence

Characterization of single QD emission requires a more complex PL setup in order to focus excitation beam to a smaller spot and to collect efficiently luminescence of a single QD. Figure 2.8 presents the experimental setup used for microPL experiments or time-resolved experiments depending on the position of the flip mirror M_1 . A laser diode emitting at 850 nm is used as a pump source. Beam is focused to a $4 \mu\text{m}$ spot on the sample with a microscope objective (Numerical Aperture=0.5). Emission is collected with the same objective and driven into the spectrometer. Collection is enhanced by using a beam splitter with a transmission/reflection efficiency of 90%/10%. The spectra resolution of the setup is better than $30 \mu\text{eV}$ (~ 0.04 nm).

2.5.3 Time-resolved photoluminescence

Time-resolved photoluminescence (TRPL) experiment was used to obtain information on the dynamics of the interband radiative recombination. Measurements were performed on the same setup as for microPL experiment. A PicoQuant pulsed laser diode emitting at 780 nm with a maximum repetition rate of 80 MHz and a pulse width of 50 ps was used

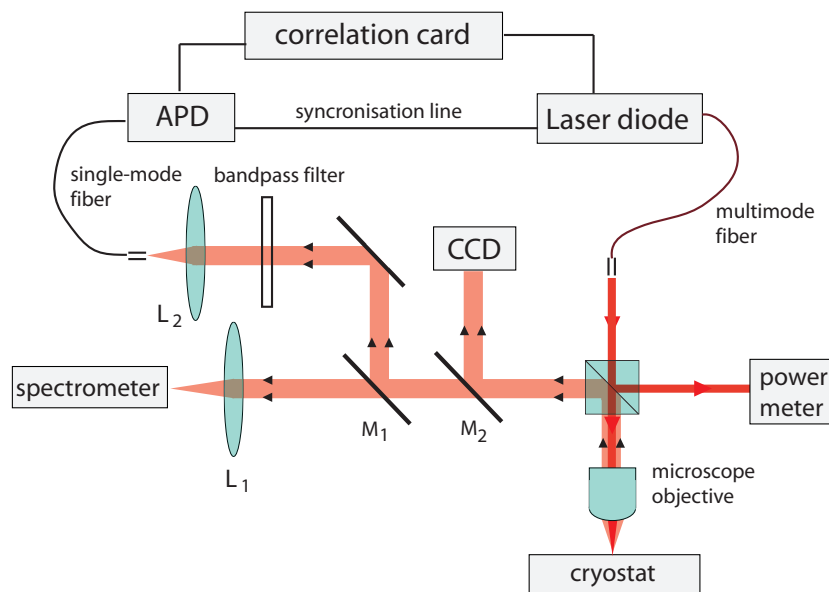


Figure 2.8: Sketch of the experimental setup used for microPL experiment and time-resolved photoluminescence measurements. The flip mirror M_1 is used to send the beam into the spectrometer or through avalanche photo diode. Flip mirror M_2 allows to visualize sample image on a CCD camera. Lens focal: $L_1=100$ mm, $L_2=8$ mm

as excitation source. As shown on figure 2.8, the emission from the sample is coupled into a single mode fiber. An idQuantique single-photon avalanche photodiode (gate opening time: 100 ns) is synchronized with a correlation card (data acquisition time: 150 ns) and the laser emission so that correlation card measures the time between laser pulses and the photon detection by the APD. Time-correlated fluorescence spectroscopy is provided in an histogram form. The setup resolution was measured with a sample of GaNInAs quantum wells, emitting at 1300 nm at room temperature, with a lifetime previously measured to be 50 ps [Bennett 05b], which is well below the temporal resolution of the detector estimated at 600 ps.

3

Growth of InAs/GaAs quantum dots

In the first chapter, the advantages of quantum dots as single photon sources have been discussed. For this purpose, such nanostructures have to fulfill the following requirements:

- A sufficiently deep localizing potential and a small size (around 10 nm), in order to obtain zero-dimensional confinement effects,
- A high crystalline quality without defects such as dislocations,
- A good uniformity in size,
- A low areal density in order to easily isolate one of them in a device such as microcavity or LED structure,
- and more specifically for our work: an emission wavelength at 1300 nm at low temperature.

We will describe in this chapter the different optimization steps of QD fabrication. In the first section, we will focus on the comprehension of nucleation and QD growth mechanisms. Effect of growth parameters on crystal growth mode and thus on the morphology of the thin deposited layer will be detailed. The respective influence between thermodynamic and kinetic mechanisms will be discussed. The second section explains step by step how to optimized the growth of low density InAs/GaAs quantum dots emitting at 1300 nm. Finally, structural characterizations of these QDs will be described in the last section.

3.1 Self-assembled quantum dots

The realization of semiconductor nanostructures that provide carrier confinement in all three directions can be achieved by several ways.

First, quantum dots can be fabricated by patterning of a quantum well structure or by growth on a prepatterned substrate [Hartmann 97]. These methods have the advantage to control shape, size, and position of the QDs depending on the resolution of the processing technique. In the other hand, fabrication methods are complex, and require a high optimization of processing techniques. Indeed, multiplicity of processing steps enhances the probability of impurity incorporation and creation of defects at the interfaces which favor non radiative recombination.

Another way to form quantum dots has been discovered by Goldstein et al. [Goldstein 85] in 1985. Formation of defect-free islands has been observed after deposition of a significant amount of InAs layer on GaAs substrate. Further researches have shown that these coherent islands present zero dimensional electronic properties. Structural properties and then optical properties of these nanostructures (or self-assembled quantum dots) can be modified by the optimization of growth conditions.

3.1.1 Growth modes

Three growth models have been built in the middle of the twentieth century to understand the epitaxial growth:

Frank-van der Merwe model (FM) (1949): based on elasticity theory, it describes the growth monolayer by monolayer below a critical misfit [Frank 49].

Volmer-Weber model (VW) (1926): applying nucleation theory, it suggests that crystalline films grow from 3D nuclei on the substrate. Their relative number and growth rate are determined by interfacial and surface free energies [Volmer 26].

Stranski-Krastanov model (SK) (1938): based on atomistic model, it shows that initially, a few pseudomorphic 2D layer is formed, on top of which 3D crystals with their natural lattice constant will grown [Stranski 38].

Each of the three scenarios is observed depending on the involved thermodynamic quantities, and give rise to the labelling of the three growth modes of epitaxy:

In a lattice-matched system, growth modes are governed by the interface and surface energies: the surface free energy of the substrate (γ_1), the surface free energy of the deposited

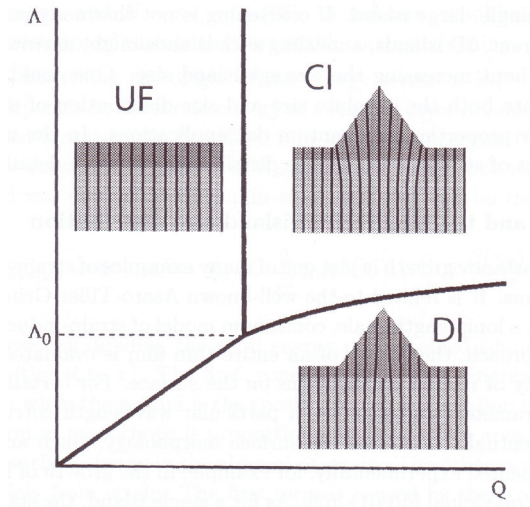


Figure 3.1: Phase diagram showing morphology (UF: Uniform Film, CI: Coherent Island, DI: Dislocated Island) as a function of the amount of deposited material Q and of Δ , ratio between energy of dislocated interfaces and change of the surface energy. (After [Vanderbilt 91])

material (γ_2) and the interface energy (γ_{12}). If $\gamma_1 > \gamma_2 + \gamma_{12}$: deposited material wets the surface, FM growth mode occurs, if $\gamma_1 < \gamma_2 + \gamma_{12}$: VW is favored.

In a lattice mismatched system, effect of strain has to be taken into account. The structural mismatch leads to a monotonic increase of the volume strain energy in the 2D pseudomorphic layer with increasing film thickness. Then for a critical thickness, γ_{12} reaches a critical value which favors the 3D growth mode. SK mode occurs because strain relief is much harder in a perfectly 2D layer than by the formation of coherent islands that adopt the bulk lattice constant.

3.1.2 Coherent island or dislocations?

For a thermodynamical point of view, the formation of an island requires a relaxation of plastic energy and a change of the surface. Surface morphology depends on the ratio (Δ) between the dislocation energy and the surface change energy. In 1991, Vanderbilt and Wickham [Vanderbilt 91] built a phase diagram showing morphology of formed island as function of amount of deposited material and Δ . As shown on the figure 3.1, formation of coherent island occurs for a sufficiently high amount of material and requires a small change of the surface energy or a large energy of the dislocated interface, so that Δ is larger than a critical value Δ_0 .

3.1.3 Nucleation mechanisms

In this paragraph we point out on the individual atomistic process responsible for adsorption and crystal growth, illustrated on the figure 3.2. Deposition fluxes from evaporation sources create single atoms on the substrate which diffuse over the surface until they are lost by one of several process. These processes include re-evaporation or re-resolution, nucleation of clusters, capture by existing clusters, and capture at special sites such as steps. On an ideally flat substrate, these last two processes would be excluded, though they may often be present in practice. Each of these processes will be governed by characteristic times, which themselves will depend on the single-atom concentration and/or coverage. If such processes are thermally activated, then these times will in turn be controlled by activation energies and frequency factors such as surface vibration frequency. Substrate temperature and deposition rate are the independent variables that can influence the system.

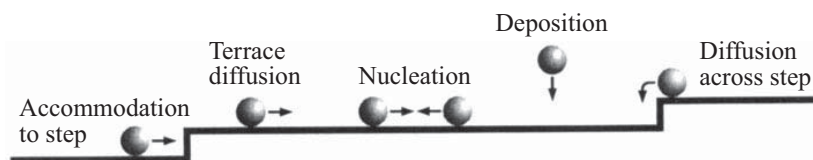


Figure 3.2: Elementary processes involved in island nucleation and thin film growth (simplified by one-dimensional projection).

However, real surfaces are not perfect and may contain a distribution of ledges, dislocations and point defects, in addition to the perfect terraces. These imperfections can influence the binding of atoms to the substrate and thus, adsorption, diffusion and nucleation behavior. Once initial clusters are formed, at defect sites or on the perfect terrace, they can re-arrange in many different ways in order to reach their most stable form. Such processes can include mixing of species (alloying), shape changes caused by surface diffusion and/or coalescence, annealing of defects, etc. Diffusion processes thus occur at different stages of thin film formation: the diffusion of single atoms to form small clusters, the mobility of these clusters themselves and the re-arrangement of larger clusters (islands) after coalescence.

Thermodynamic and kinetic theories are used to explain the final state of the system. Lowest-energy configuration can be foreseen by thermodynamic considerations, however, the final state which is observed is not necessarily the most stable and thus depends on kinetic

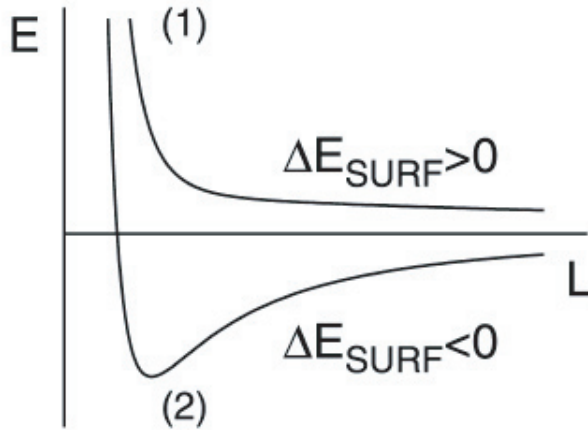


Figure 3.3: Energy per atom versus island size for an array of three-dimensional coherently strained islands. (1): An array of islands exhibits a driving force to Ostwald ripening. (2): An optimum size of the islands exists. Ostwald ripening is not favorable energetically. (From [Shchukin 01])

mechanisms. Some process can be kinetically forbidden, others may be in “local” thermodynamic equilibrium, and some other will be kinetically rate-limited depending on growth parameters such as substrate temperature or pressure.

3.1.4 Mechanism of size ordering versus Ostwald ripening

Control of island size and size homogeneity is primordial to obtain reliable single photon source at 1300nm. Comprehension of mechanisms involved in the QD size evolution is thus required.

Once islands are formed, adatom migration on the surface allows material exchange between islands in order to minimize the total energy of the system. Thermodynamic and kinetic mechanisms have been proposed to explain size distribution of islands after growth. Thermodynamic principle will suggest that large islands will grow at the expense of smaller islands. This mechanism is called Ostwald ripening mechanism. However, it has been observed that islands, after being formed, apparently do not undergo Ostwald ripening and display a narrow size distribution. The change of the total energy of the system due to the formation of a single 3D island has been calculated by Shchukin et al. [Shchukin 01]. The dependence of the energy per atom E in the islands versus island size L is shown on the figure 3.3. Transition between ordering and ripening depends on the change of surface energy. If the formation of a single island results in an increase of the surface energy ($\Delta E_{surf} > 0$), there exists a driving force to ripening, since the minimum of $E(L)$ corresponds to $L \rightarrow \infty$. This would correspond to one large cluster where all deposited material is collected. If

the formation of a single island leads to a decrease of the total surface energy, despite the increase of the total surface area, there exists an optimum size of island corresponding to the absolute minimum of the energy. There is no driving force to ripening in this case. In this model, the change of the surface energy is mainly due to the appearance of side facets, and the disappearance of certain area of the wetting layer. Shape and size of the island appear then to be strongly interdependent. We note that for a dense system of islands, elastic interaction between islands via the strained substrate becomes possible and needs to be taken in consideration. There exist a minimum of the strain energy corresponding to a certain distance between island.

Kinetic models taking into account processes such as diffusion, deposition, attachment and detachment, predict evolution of island density and size distribution as function of growth rate and coverage [Dobbs 97]. A narrowing size distribution can be explained by different mechanisms such as a preferential migration of adatoms towards smaller islands due to kinetic barriers which limits the attachment to strained island [Kobayashi 96], an influence of island facets on the kinetic growth [Jesson 98], an enhancement of adatoms detachment from large island due to the competition between bonding energy at the island edges as compared to the strain energy at the edges [Barabasi 97]. This results in a tendency for self-limited size of an array of coherent islands.

Influence of growth parameters appears determinant in the relative influence of thermodynamic and kinetic mechanisms and then, in the final surface morphology after growth. In the following, we will detail the different steps of the growth optimization in order to obtain a sparse array of InAs/GaAs quantum dots (around $1 \text{ QD}/\mu\text{m}^2$) together with a wavelength emission at 1300 nm at low temperature i.e. 1400 nm at room temperature.

3.2 Growth optimization

This section details chronologically the optimization steps performed in order to form large and sparse QDs. A combination of an ultra-low InAs growth rate with an InGaAs capping layer has been found to provide QDs which fulfill the required characteristics. To study the influence of different growth parameters, AFM and PL characterization techniques have been employed. For sample series grown for AFM investigation, the substrate was immediately cooled down to room temperature just after InAs deposition and kept under an As overpressure. To perform PL measurements, a second series of samples was grown under the same growth conditions except that the dots were capped by 100-nm thick GaAs layer.

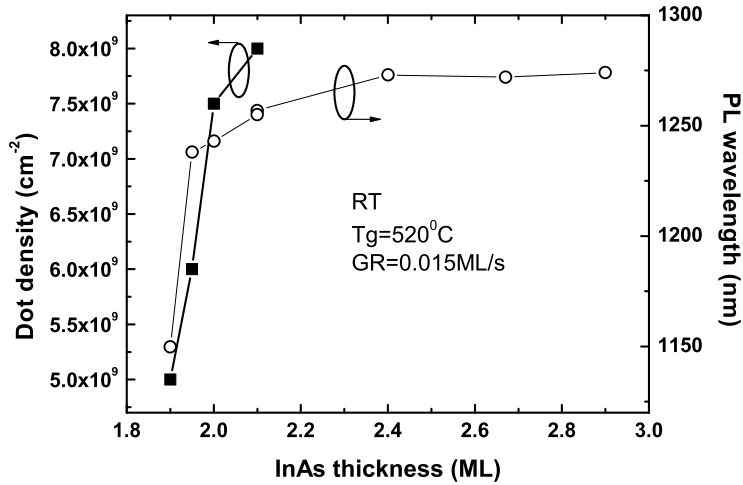


Figure 3.4: Evolution of InAs quantum dots density and PL wavelength as function of InAs thickness.

3.2.1 First approach: decrease of InAs thickness

In 1994, Leonard et al. [Leonard 94] shows that dot density can be decreased by reducing the total amount of deposited InAs. In 1996, Kobayashi et al. [Kobayashi 96] confirmed this trend using in situ atomic force microscopy. First spectroscopy experiments on single quantum dots used a very thin InAs layer [Marzin 94, Grundmann 95]. We thus were first interested in this growth parameter.

Two series of samples with different InAs thickness were grown for AFM and PL investigations. InAs layer was deposited on a $0.5 \mu\text{m}$ -thick GaAs buffer layer. The buffer layer was grown at 620°C under a background pressure of 10^{-6} mbar. During InAs deposition, growth temperature and pressure were fixed at 520°C and 10^{-6} mbar respectively. InAs growth rate was estimated at 0.015 ML/s . AFM and PL results are summarized on the figure 3.4. As we can see, at low coverage the density decreases rapidly but the PL wavelength blueshifts at the same time. We attribute this blueshift to a decreasing QD size due to a smaller amount of deposited InAs material. However this trend was not evident through AFM observations.

Decrease of InAs thickness appeared then not suitable for our application, as we need QDs emitting at 1300 nm . We then turned on to the study of another growth parameter such as InAs growth rate.

3.2.2 Second approach: growth rate effect

Experimental observation of growth rate effect on structural and optical properties of InAs/GaAs quantum dots has been reported by several groups [Joyce 00, Nakata 00, Murray 98]. A decrease of the InAs growth rate is found to reduce the dot density and to extend the emission wavelength. According to these studies, the decrease of QD density is due to an increased migration length of In adatoms at low growth rates. Indeed, in order to minimize the strain and the surface energy, In adatoms incorporate into existing islands instead of forming new dots. This mechanism is easier with a large migration length and leads to a reduction in QD density and an increase in QD size. We decided to investigate this effect by growing a series of sample at different InAs deposition rates.

As we will see in the following, the InAs growth rates that were investigated in this work reached very small values. It was not practically possible to measure them by a conventional BEP reading or by RHEED oscillation method. We thus measured them from the 2D-3D transition observed by RHEED. Assuming that the critical thickness is $1.7\text{ ML} \pm 0.1\text{ ML}$ [Joyce 00, Patella 06, Leonard 94] and depends weakly on the growth rate [Tu 04, Dubrovskii 04], a value of InAs growth rate was deduced with an accuracy estimated at 10%.

In flux variation

The first way to vary the InAs growth rate is to change the In cell temperature and thus the In flux.

After buffer growth, 2.1 monolayers of InAs were deposited at different growth rates in the range 0.16-0.0012 ML/s at fixed growth temperature and As pressure. Two series of samples were grown for PL and AFM measurements. Dot density as function of the growth rate is shown in figure 3.5(A). InAs growth rate is observed to have a strong influence on the QD density. A dot density as low as $2 \cdot 10^8$ dots/cm² is obtained when InAs growth rate is reduced down to 0.001 ML/s.

Furthermore, figure 3.5(B) reporting the RT PL measurements, shows a redshift of PL peak emission wavelength. This can be related to a higher confinement energy attributed to the increased QD size and In content [Joyce 00], as the growth rate is decreased. TEM observations detailed in the next section will confirm this tendency. Wavelength reaches 1310nm at RT at the lowest growth rate. We note that ground state (GS) and first excited state (ES) signal are clearly distinguishable and that spectra present a full width at half

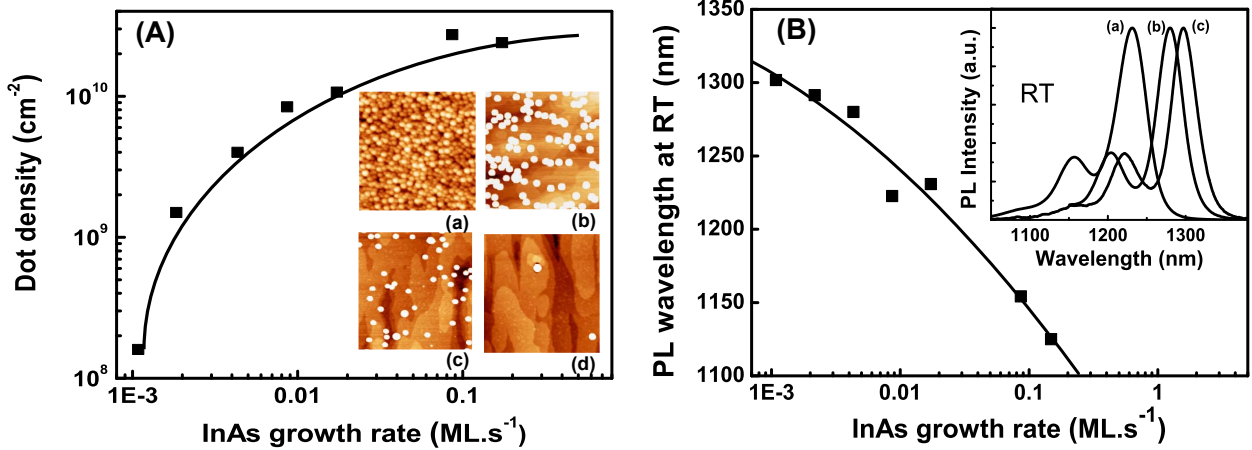


Figure 3.5: (A) Dot density, as measured from AFM images plotted as a function of InAs deposition rate. The solid line is a guide to the eye. Inset: $1 \times 1 \mu\text{m}^2$ AFM images of 2.1 ML InAs deposited with following growth rates: (a) $0.16 \text{ ML}\cdot\text{s}^{-1}$, (b) $0.08 \text{ ML}\cdot\text{s}^{-1}$, (c) $0.004 \text{ ML}\cdot\text{s}^{-1}$, (d) $0.0015 \text{ ML}\cdot\text{s}^{-1}$. (B) Evolution of PL emission wavelength as a function of InAs growth rate. Inset: normalized PL spectra at RT of 2.1 ML-thick, GaAs-capped InAs QDs grown at (a) 0.015 ML/s , (b) 0.0035 ML/s , (c) 0.0015 ML/s .

maximum (FWHM) value around 25 meV which implies a good QD size homogeneity. We still note that the broadening relative to the QD size inhomogeneity is less important in case of large QDs than in the case of small QDs since the GS energy is proportional to $1/l^2$, with l the characteristic linear size of the system.

Influence of growth temperature/pressure

Growth pressure and growth temperature influence kinetics of the QD formation, and especially the growth rate value.

High temperature increases the mobility of adatoms on the surface and favors the formation of larger dot size. Moreover, it increases the adatom diffusion length and In desorption rate. The effect is significant for ultralow growth rate. As we will see in the section 3.4., the increase of growth temperature delays the QD formation and then decreases the InAs growth rate. At a growth temperature of 505°C , In desorption rate value becomes comparable to the growth rate values that we used.

The As pressure has also a strong influence on the QD morphology. Ledentsov et al. [Ledentsov 96] showed that an increase of the As pressure leads to a reducing island size

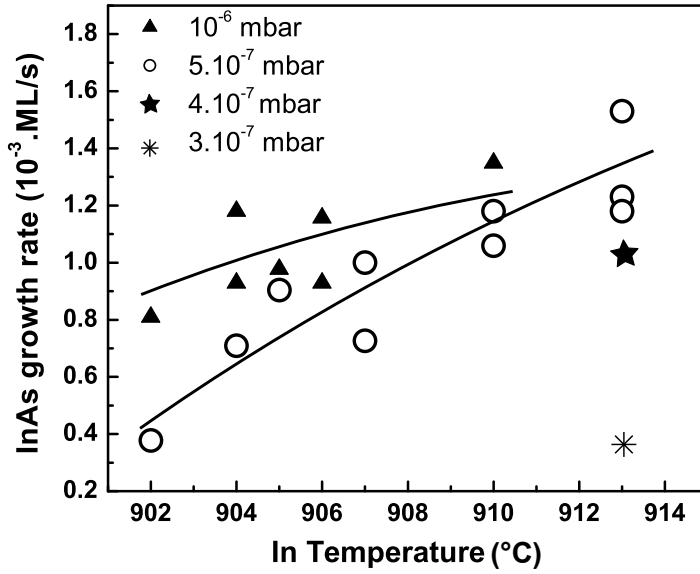


Figure 3.6: InAs growth rate measured for different In cell temperatures on samples grown under different As pressure. Growth temperature was fixed at 505°C. Solid lines are guide to the eye for samples grown under a growth pressure of $5 \cdot 10^{-7}$ mbar and 10^{-6} mbar.

and a higher concentration of dislocated clusters. Inversely low As pressure enlarges the diffusion length of the adsorbed In atoms. Redshift at low As pressure has been observed [Chu 99] together with an improvement of the QD quantum efficiency [Trofimov 04]. QD growth under different As pressure and In flux was then performed. Figure 3.6 presents the evolution of InAs growth rate measured on many samples at different In cell temperatures and for different As pressures. We observe that growth rate decreases at low As pressure. For low In cell temperature ($< 910^\circ\text{K}$), when As pressure is lower than $5 \cdot 10^{-7}$ mbar, 2D-3D transition is not visible any more at the RHEED. AFM measurements do not provide a clear trend of QD density as function of As pressure. Considering work done by Riel et al [Riel 02], at low As pressure, the distribution of material between the WL and QDs appears to favor a stabilization of QD size, and therefore of QD emission lines. We then decide to reduce As pressure down to $5 \cdot 10^{-7}$ mbar during QD growth.

We have demonstrated that growth rate can be controlled by several ways:

- Decreasing In flux
- Increasing growth temperature
- Reducing As pressure

An InAs growth rate as low as 0.001 ML/s allows to reduce the QD density down to

$2 \cdot 10^8$ dots/cm². These low-density quantum dots (LDQDs) present a PL emission wavelength at 1300 nm at room temperature i.e. ~ 1200 nm at low temperature. Results are encouraging but not sufficient since wavelength emission is still 100 nm smaller than required. To extend furthermore the wavelength to 1400 nm, we choose to grow an InGaAs capping layer, after the QD deposition.

3.2.3 Optimization of the capping layer

Emission wavelength can be extended by using an InGaAs capping layer on top of the QDs. The redshift can be attributed to three main factors:

strain relaxation: InGaAs lattice parameter is larger than GaAs but smaller than InAs which is predicted to reduce the compressive strain in the QDs [Nishi 99, Yeh 00, Liu 05]. This has been calculated to reduce the bandgap [Sun 06]. However, it should be mentioned that recent calculations based on continuous elasticity theory affirm the contrary, InGaAs is a “strain-reinforcing” layer: due to the strain in the InGaAs layer induced by the lattice mismatch with GaAs, it reinforces both in-plane compressive strain and vertical tensile strain in the QDs; this is found to decrease the band gap energy [Shin 06].

matrix bandgap: reduction of the matrix (WL+capping layer) bandgap results in a change in quantum confinement effects due to wave-function penetration into the covering layer.

mass transport: another explanation is mass transport inside the InGaAs capping layer due to In segregation [Maximov 00]. There is formation of In-rich region on top of the dots in the InGaAs capping which increases QD size and results in higher localization energies.

It has been reported that QD size change is very small with addition of a capping layer. This would lead to negligible effect of size increasing [Yeh 00, Sun 06]. Furthermore, a capping layer of InAlAs shows a redshift of PL, although InAlAs bandgap is larger than GaAs. This shows that strain relaxation is the main mechanism responsible for the wavelength extension. Redshift is less pronounced than with InGaAs, because of the higher elastic stiffness of InAlAs as compared to InGaAs [Yeh 00]. InGaAs capping is also found to reduce the linewidth. This has been attributed to a reduction of the In segregation with InGaAs

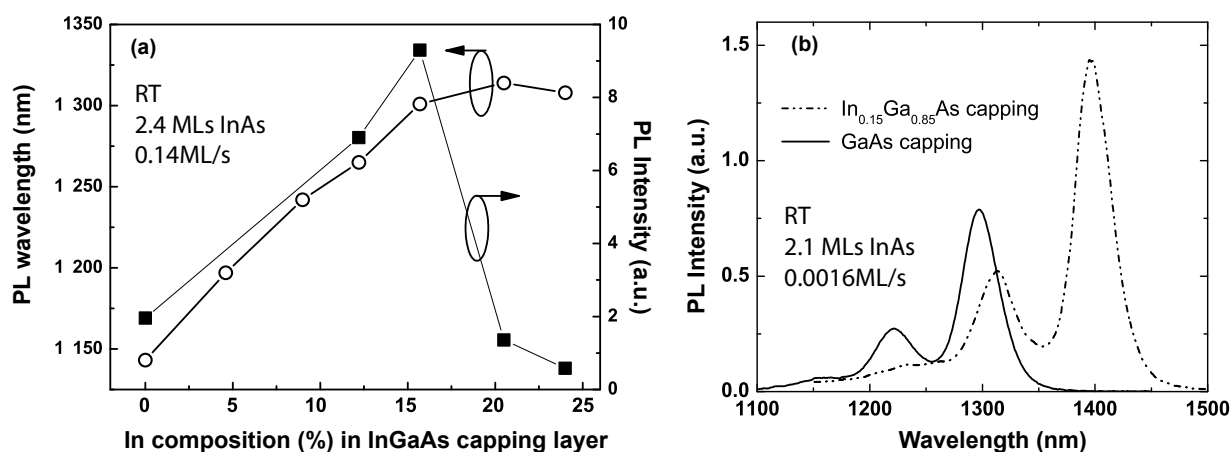


Figure 3.7: (a) Influence of capping layer composition on PL wavelength and PL intensity. (b) RTPL spectra of low density InAs QDs capped by GaAs or InGaAs layer.

capping, which leads to a better QD size homogeneity [Nishi 99]. As we will see in the following, this will be confirmed by TEM observation: QD grown at very low growth rate present an atypical large height and a high concentration of In.

Capping layer composition

Several test samples have been grown, to determine the optimal In composition of InGaAs capping layer. Effect on PL wavelength and PL intensity is presented on figure 3.7(a). For these tests, 2.4 MLs of InAs were deposited with a growth rate of 0.14 ML/s. Growth temperature was kept at 530°C. According to literature, we used a common InGaAs thickness of 5 nm. For high InGaAs thickness (>8 nm), redshift is found to saturate and PL intensity decreases ([Nishi 99]). Standard growth rate around 0.8 ML/s has been used to avoid incorporation of impurities and then assure a good layer quality. We clearly see that the good compromise between a high PL intensity and a long wavelength emission occurs for an In composition comprised between 15% and 20%. Figure 3.7(b) shows room-temperature PL spectra of QDs grown at low growth rate (0.0016 ML/s) with GaAs and InGaAs capping layer. We observe a strong redshift of the PL wavelength and an enhancement of the PL intensity due to the InGaAs capping layer deposition.

Combining InGaAs capping layer and low-growth rate QDs allows to reach low density QD and long wavelength emission at the same time. However it should be mentioned that this requires to have two In cells in the growth chamber since QD and InGaAs capping layer

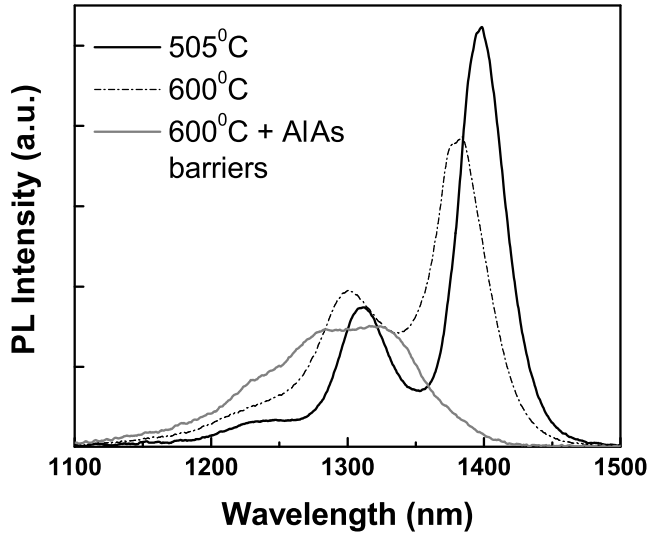


Figure 3.8: Room-temperature photoluminescence spectra of QDs capped by InGaAs and GaAs under growth temperature of 505°C and 600°C.

depositions occur at much different growth rates and then need different In cell temperatures.

Growth temperature during capping layer deposition

We observed a remarkable degradation of QD optical properties when GaAs capping layer was grown at 600°C. As shown on the figure 3.8 the ground state (GS) PL peak intensity decreases and the GS PL peak wavelength blueshifts. The degradation is even stronger when QDs are embedded in AlAs barriers (also grown at 600°C). The blueshift can be attributed to the interdiffusion of In and Ga atoms at the interface between QD layer and the GaAs barrier at high temperature [Xu 98, Fafard 99, Ru 03]. However, the decrease of PL intensity is unusual. Capping of high density QDs at 600°C resulted in no significant change. We believe that the plastic relaxation in the large low-density QDs might happen during the capping procedure due to the highly accumulated strain and the large QD size, which might be responsible for the optical property degradation. Noticed that the growth of rest upper layer of any device is very similar to this procedure, it is important to select a right growth temperature to conserve a good quality of the low-density QDs. We found that a growth temperature close to the one used for the dot growth is a good choice. For a capping temperature of 505°C, PL spectrum presents a higher intensity and a narrower linewidth.

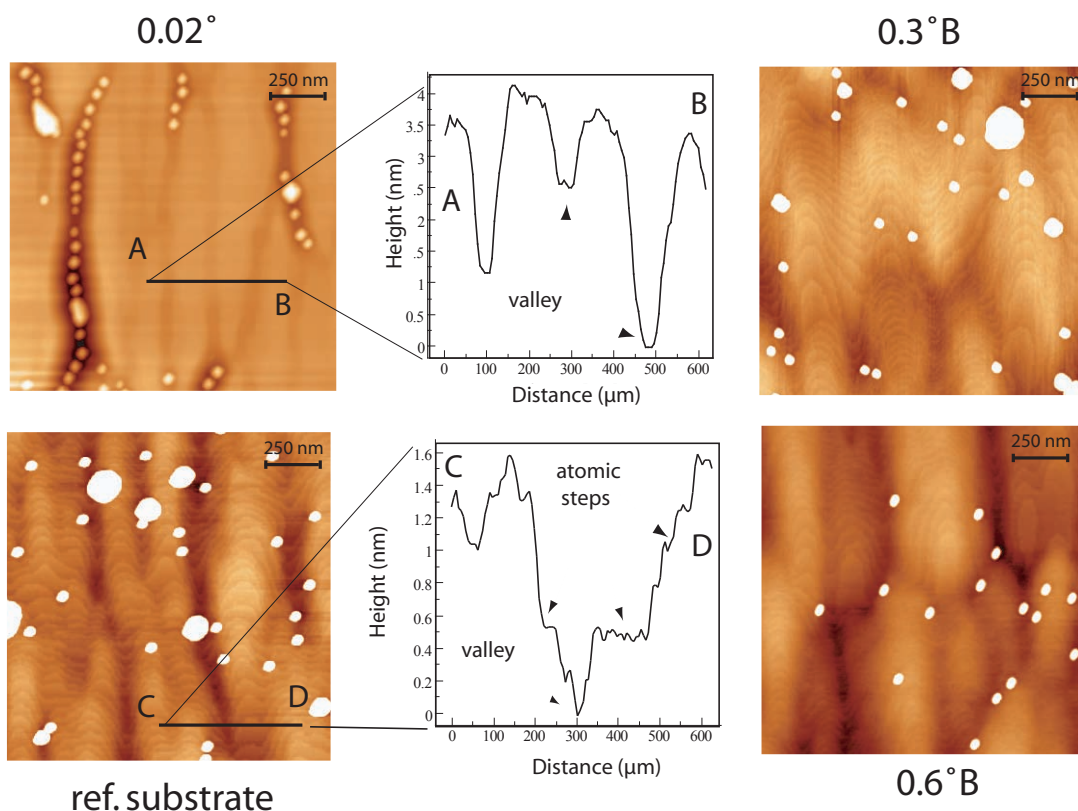


Figure 3.9: AFM pictures ($1.5 \times 1.5 \mu\text{m}$) of QDs grown on GaAs substrate with different small misorientations. Profiles of perfectly orientated substrate and reference substrate are shown.

3.2.4 Substrate misorientation

Study of sample misorientation has been performed and used to influence the QD position. It has been observed that QDs nucleate preferentially on step edges of multiatomic steps [Leonard 94] which are created by surface reconstruction. Different step orientations with different density can be introduced with an intended miscut. On a (100) GaAs surface, miscut towards $\langle 011 \rangle$ and $\langle 01\bar{1} \rangle$ results in type-A (i.e. Ga-atom layer on the surface) steps running along $\langle 01\bar{1} \rangle$ and type-B (i.e. As-atoms layer on the surface) steps running along $\langle 011 \rangle$, respectively. The density of steps depends on the degree of misorientation. If substrate is exactly oriented, multiatomic steps are very large. Self-alignment of QDs have been observed for misorientation degree below 6° [Kitamura 95, Oshinowo 94, Poser 03, Wang 04].

All samples used in this work have been grown on $(001)\pm 0.5^\circ$ GaAs substrate. This substrate will be taken as reference. Influence of a misorientation below 6° is usually negligible for QDs grown at higher growth rate and with higher areal density. Nevertheless, regarding the long QD time deposition that we used, we can suspect an effect of the small surface corrugations on the QD position.

Several pieces of misoriented substrates, type A and B, with a degree of misorientation comprised between 0.02° (perfectly (001) oriented substrate) and 0.6° were stucked together with a reference piece of commonly used GaAs substrate on a molybdenum support and introduced in the growth chamber. After growth of 2.1 ML InAs at 0.002 ML/s, substrate was cooled down for AFM investigations. Measurements are summarized on figure 3.9.

A succession of deep valleys and atomic steps can be seen as usually for slightly misorientated samples. As commonly observed, QDs are formed preferentially at the edges of the atomic steps. Since misorientation is too small to form steps on straight lines, it results in a random and quite homogeneous QD repartition on the surface. Results are similar for sample type A (not shown) and B. In case of perfectly oriented substrate, situation is different. Atomic steps are larger and not easily distinguishable. QDs are then formed preferentially in the deep valley (<3 nm deep). It results in a very inhomogeneous repartition of the islands and a strong tendency to align. This could be considered as a first step towards determining QD position. In our case, this effect is rather negative for the realization of devices since QDs are grouped and can not be excited separately. This study is nevertheless interesting since it notices that perfectly orientated substrates have to be avoided for the growth of single quantum dots devices.

3.2.5 Other optimization: growth interruption

Finally we have compared the method using very long QD deposition time, with method employing growth interruption procedure after QD growth. Growth interruption is often used to extend QD emission wavelength since it gives rise to an increase of larger islands at the expense of the smaller ones due to Ostwald-ripening process [Gérard 95, Min 98, Convertino 04]. Advantage of this method is that the growth interruption time can be used to change the In cell temperature. In our case, this would allow us to increase the In cell temperature in order to use the same In cell for InAs QDs and InGaAs capping layer deposition.

Several test samples have been grown. In this case, 1.7 ML-thick InAs layer is deposited

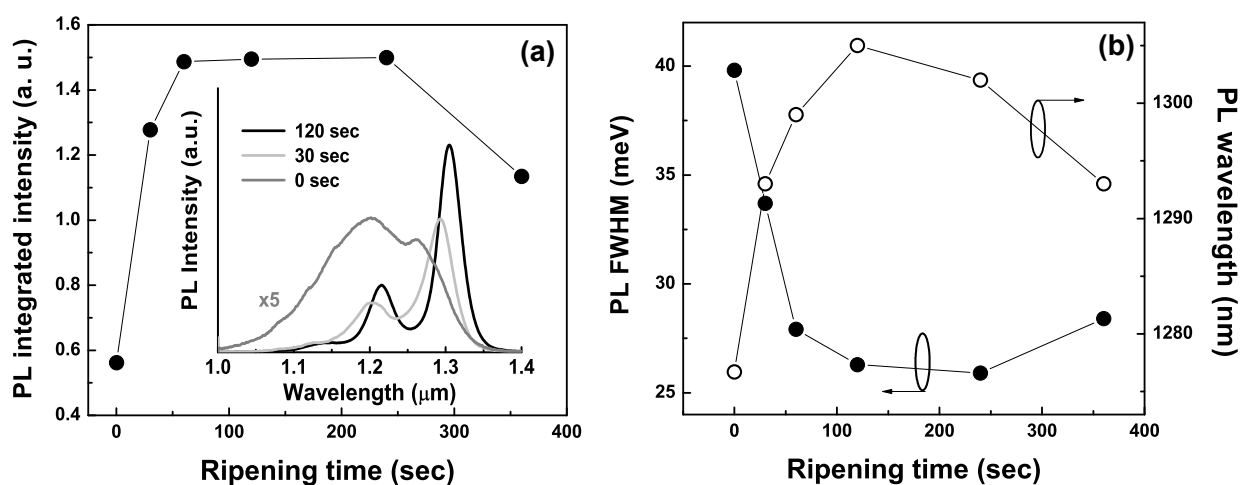


Figure 3.10: Evolution with growth interruption time of (a) PL intensity (b) PL FWHM and PL wavelength. (a) inset: PL Spectra of 1.7 ML-thick InAs QDs capped by GaAs for three different annealing times.

at 0.002 ML/s. Immediately after the QD formation is observed by the RHEED, growth is interrupted, sample is kept for several seconds to several minutes under As overpressure before GaAs capping layer deposition. Growth temperature and pressure are fixed at 500°C and 10^{-6} mbar, respectively during the epitaxy. Effects on RTPL emission are shown on the figure 3.10. We observe that growth interruption procedure results in an increase of PL intensity and wavelength. FWHM decreases strongly at the same time which indicates that QD size homogeneity is enhanced. Best results are observed for an interruption time about 120 sec with an emission wavelength at 1304 nm. AFM pictures show a rather small QD density ($\sim 10^9$ dots $\cdot\text{cm}^2$) but surface repartition seems less homogeneous as for the first growth method. Nevertheless, results are comparable, and further optimization procedures might make this method an interesting alternative requiring only one In cell.

3.2.6 Conclusion

Considering the optimization of different growth parameters we finally adopt the following conditions for the QDs growth:

Layer	Thickness	Growth rate	Growth temperature	Background pressure
GaAs buffer	500 nm	0.8 ML/s	600°C	10^{-6} mbar
InAs QDs	2.1 ML	0.002 ML/s	505°C	$5 \cdot 10^{-7}$ mbar
In _{0.15} Ga _{0.85} As	5 nm	0.85 ML/s	505°C	10^{-6} mbar
GaAs	100 nm	0.8 ML/s	505°C	10^{-6} mbar

Figure 3.11 shows the PL emission on this kind of sample, AFM and TEM characterization evidence the required low dot density.

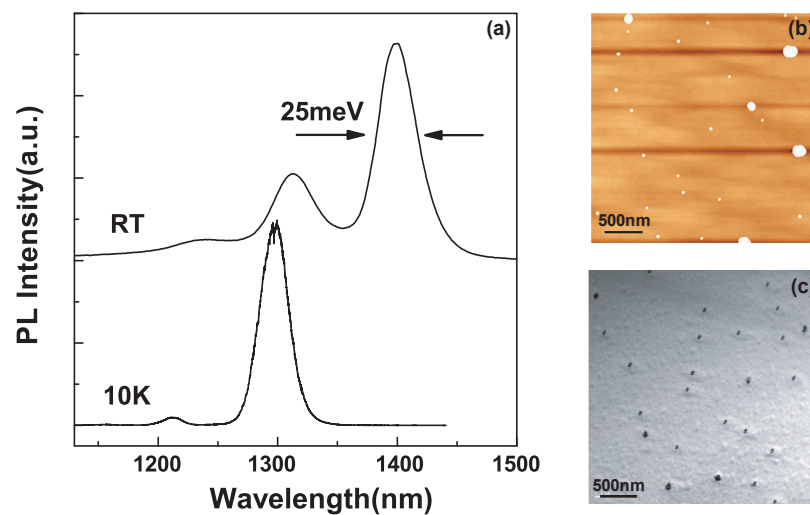


Figure 3.11: (a) PL (b) AFM and (c) TEM (performed by M. Cantoni at CIME, EPFL) characterizations of sample grown under optimized growth conditions.

3.3 Assessment of desorption rate

In the precedent section, influence of growth parameters on QD density and emission have been observed. Now, influence of different kinetic mechanisms involved in QD formation is investigated through the comparison between results and standard kinetic models. We remarked on several test samples grown at the same growth temperature, that below a certain value of In cell temperature, QD nucleation could not be observed at the RHEED. However 2D-3D transition can be recovered by decreasing the sample temperature. This proves that absence of transition is not due to the In cell (In flux is still reliable even at low cell temperature) but is determined by kinetic mechanisms and especially In desorption.

In the following the distinction is made between the In deposition rate R_{Dep} , and the InAs growth rate R_G : The In deposition rate is related to the In flux F and represents the rate of incident In atoms coming on the substrate, whereas the InAs growth rate, measured by the RHEED, represents the effective amount of material grown on the substrate. As it is difficult to directly measure by RHEED oscillations the low In fluxes used in this work, one value, F_0 , of In flux was obtained at high In cell temperature by extracting the measurement results of X-ray diffraction, and then extrapolated to other cell temperatures with the relation: $F=F_0 \cdot \exp(E/kT_{In})$ with E , the In activation energy, and T_{In} the In cell temperature. Figure 3.12(a) shows the variation of R_G (as measured from the 2D-3D transition time) with F , we observe that the relation is linear for $R_G > 0.002 \text{ ML} \cdot \text{s}^{-1}$. Figure 3.12(b) presents data taken over three years and shows evolution of the dot density measured by AFM as function of In flux. As we have seen before, QD density decreases by reducing In flux. A dot density of $2 \cdot 10^8 \text{ dots/cm}^2$ is obtained when the In flux is reduced down to $10^{12} \text{ cm}^{-2} \cdot \text{s}^{-1}$ (corresponding to an InAs growth rate around 0.001 ML/s). In this general trend, three distinct regimes are visible:

The first regime appears for $\text{In flux} > 3 \cdot 10^{12} \text{ cm}^{-2} \cdot \text{s}^{-1}$. The QD density exhibit a dependence on the growth rate following the standard nucleation theory and can be fitted by the relation [Venables 84, Jeffrey 06, Bartelt 92]:

$$N = \alpha \cdot F^\chi. \quad (3.1)$$

The slight difference between the exponent that we observe, $\chi=0.56$, and the values predicted by theory ($\chi \sim 0.3$), can be attributed to the influence of the elastic energy which is not taken into account in the model of Ref. [Venables 84, Bartelt 92].

However, this fit cannot be used for $F < 3 \cdot 10^{12} \text{ cm}^{-2} \cdot \text{s}^{-1}$: QD density decreases abruptly

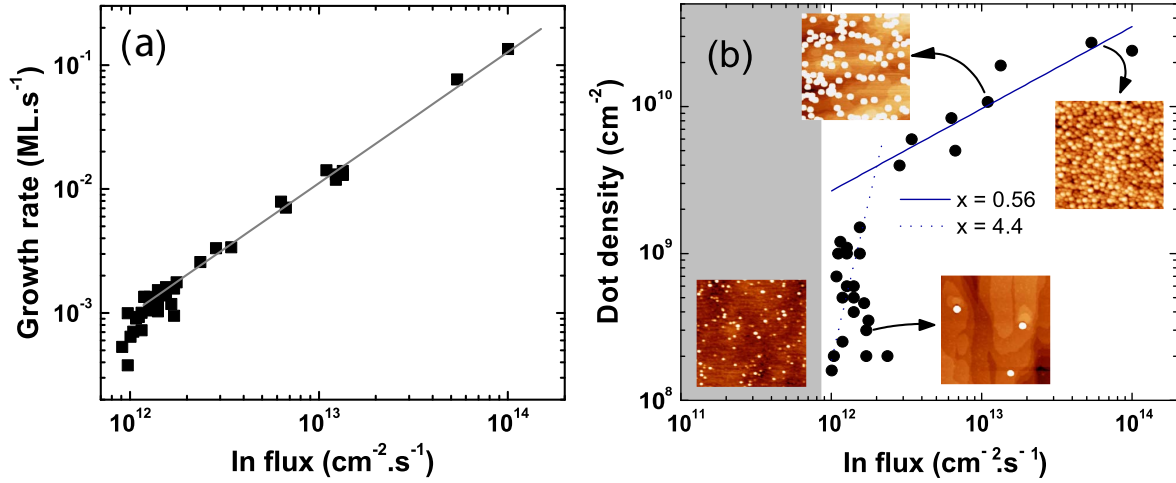


Figure 3.12: (a) InAs growth rate measured by RHEED under a substrate temperature of 505°C as function of In Flux. The solid line represents a linear fit. (b) QD density, as measured from AFM images, as a function of In flux. AFM images are done on a $1 \times 1 \mu\text{m}^2$ area. The solid and dotted lines show the flux dependence of the dot density fitted by the relation $N = \alpha \cdot F^\chi$, with $\chi = 0.56$ and $\chi = 4.4$ respectively. Grey area represents the region where no nucleation is observed.

and the fit provides a value of $\chi = 4.4$ in this region. This type of behavior was in fact predicted in Ref. [Venables 84], when island density dependency as function of deposition flux, is modelled in case of negligible and important In desorption. For both cases, density dependency follows relation (3.1) but exponent χ varies from $i/(i+2)$ to i (with i , number of atoms in the island, this model discussed about the first steps of nucleation) when In desorption becomes predominant. The steeper decrease of the density that we observed could also be related to the increasing relative contribution of In desorption: as the desorption rate approaches the deposition rate, the number of adatoms available for nucleation decreases. QDs with low areal density $\sim 1\text{-}10 \mu\text{m}^{-2}$ and large size (the height of uncapped QDs is estimated around 12 nm by AFM) are formed in these conditions.

Finally, a third regime occurs for In flux lower than $10^{12} \text{ cm}^{-2} \cdot \text{s}^{-1}$ (indicated by the grey area on figure 3.12(b): for this flux region, islanding transition can not be observed by RHEED. AFM measurements performed on these samples show a high density ($60 \cdot 10^8 \text{ dots/cm}^2$) of islands, with a significantly smaller size (3 nm) than those grown at higher growth rate. These small QDs may have been formed during the cooling process of the sample after

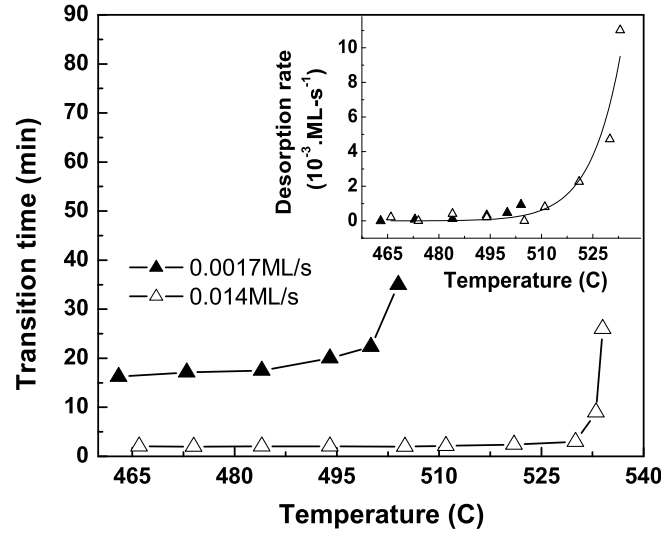


Figure 3.13: Evolution of 2D-3D transition time with growth temperature for two In fluxes corresponding to InAs growth rates of 0.0017 ML/s and 0.014 ML/s at 470°C. Inset: Evolution of deduced desorption rate as function of growth temperature, the solid line is a fitted curve following the relation $R_{Des} = A \cdot \exp(-E_d/kT)$.

growth since we do not observe any luminescence signal on a similar sample, capped by a GaAs layer after InAs deposition. This has been attributed to the arsenic condensation during the substrate cooling [Krzyzewski 04]. We suppose that under these growth conditions, the In desorption rate is comparable to the deposition rate, preventing the onset of nucleation.

In order to compare quantitatively the In desorption rate R_{Des} with the deposition rate R_{Dep} , we used RHEED to study QD formation at different growth temperatures. It is established that in InAs/GaAs system, intermixing with Ga from the substrate and In desorption are involved in QD formation. The effect of these mechanisms depends strongly on growth parameters and becomes more significant with increasing growth temperature. We have measured by RHEED the 2D-3D transition time θ for different growth temperatures at two In fluxes (corresponding to InAs growth rates of 0.0017 ML/s and 0.014 ML/s at a 470°C growth temperature). The results are presented on figure 3.13. We observe that θ has a temperature-activated behavior, increasing strongly above a critical temperature, which depends on the InAs growth rate. Since negligible intermixing has been reported for

low growth rates [Heyn 05, Joyce 00], we attribute this strong increase to In desorption. In these conditions, the growth rate R_G can be expressed as $R_G = R_{Dep} - R_{Des}$. As θ is almost constant in the 460°C-480°C, desorption rate is negligible in this region and a R_{Dep} value can be estimated, independent of growth temperature. R_{Des} as function of growth temperature can then be deduced, its evolution is presented in the inset of figure 3.13 and fitted by the relation $R_{Des} = A \cdot \exp(-E_d/kT)$ [Foxon 78]. We obtain a value of an activation energy about 2.8 eV which is in the range of values reported in literature [Mozume 92, Coleiny 03]. We also note that at 500°C the desorption rate value reaches approximately 0.0005 ML/s and is in the same range as the In deposition rate, which is used for low-density QD growth. This explains the very long transition time at this growth temperature. Furthermore, in the 500°C region, R_{Des} is very sensitive to the growth temperature which results in the dispersion in QD density as shown in figure 3.12(b). Moreover this value is very close to the minimum value of InAs growth rate above which it is still possible to observe the 2D-3D transition by RHEED.

3.4 TEM characterizations

The morphology of low-density QDs was investigated. AFM images show a slight increase of the QD size with a decreasing growth rate. In order to precisely determine the QD dimensions, TEM measurements were performed by G. Patriarche from LPN (Marcoussis, France) on two samples containing low-density QDs grown at the same growth rate (0.0015 ML/s) with GaAs and InGaAs capping layer. Figure 3.14 shows cross-sectional (002) Dark Field TEM images of the QDs which present a lens shape with larger dimensions than usually observed: 7.5 nm height for QDs capped by GaAs and 9 nm for those capped by InGaAs. These values are larger than the typical height around 5 nm for QDs grown at higher InAs growth rate [Joyce 01, Offermans 05, Bruls 02]: The large size is partly responsible to the long emission wavelength obtained for these samples. Height and composition difference observed for different capping material contribute to the PL red-shift upon capping by InGaAs. Depending on the capping layer, the morphology of the 2D layer (WL+capping) surrounding the QDs is quite different: uniform for GaAs-capped QDs, the 2D layer for InGaAs-capped QDs appears on the contrary very thick (about 10 nm) close to the QDs and becomes thinner (7.6 nm) at longer distances. STM studies reported a planarization effect of InGaAs capping which is symptomatic of enhanced surface diffusion lengths. This would preserve QD height and shape more effectively than with GaAs capping

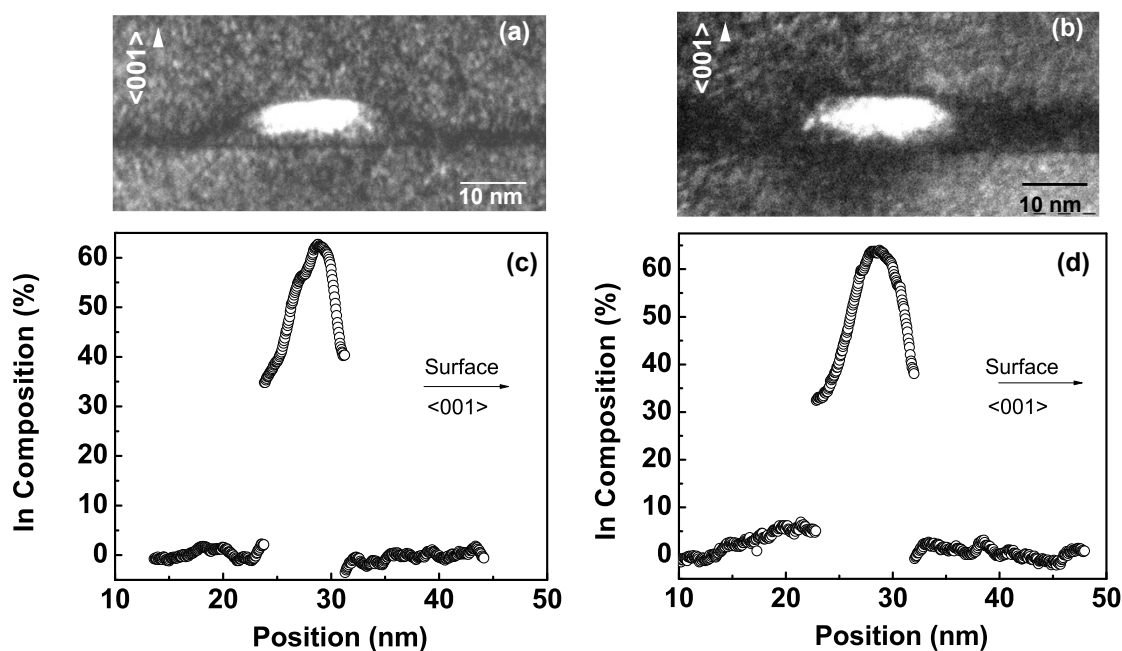


Figure 3.14: (002) Dark-Field images of QDs grown at low InAs growth rate (0.0015 ML/s) and capped by (a) GaAs, and (b) InGaAs. (c) and (d) show the In composition variation in the $\langle 001 \rangle$ direction of the QDs capped by GaAs and InGaAs, respectively.

[McGee 06]. To estimate the In composition distribution, we used the technique proposed in Ref. [Patriarche 04, Lemaitre 04] which allows the estimation of In content from TEM contrast in dark-field (002) images, with a spatial resolution higher than 2 ML. Under 002 dark field conditions, the image contrast is mainly sensitive to the chemical composition of the sample, due to the strong influence of the In composition on the structure factor of the $\text{In}_x\text{Ga}_{1-x}\text{As}$ lattice. The ratio $I_{\text{In}_x\text{Ga}_{1-x}\text{As}}/I_{\text{GaAs}}$ between the intensity of the $\text{In}_x\text{Ga}_{1-x}\text{As}$ layers and the intensity of the GaAs layer can be precisely calibrated in order to measure the concentration of In in the epitaxial structures [Saint-Girons 06b]. Figure 3.14(d) shows the In composition profile of the QDs capped by InGaAs along the $\langle 001 \rangle$ direction, through the QD center. QDs present a strong In gradient with a maximum In composition of 65% in the dot center and 35% at the bottom. Indium composition profile is very similar for QDs capped by GaAs, with an In content comprised between 62% and 35%. The mean In composition is estimated about 50.4% and 50.6% for GaAs-capped and InGaAs-capped sample. This shows that capping layer composition influence QD dimension rather than

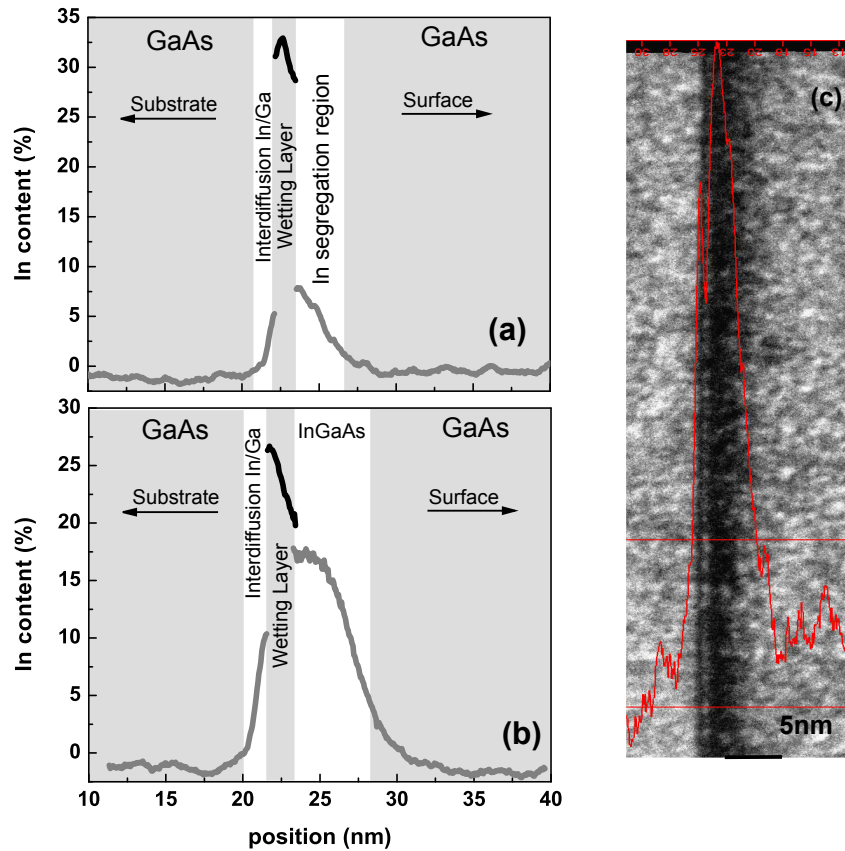


Figure 3.15: In profile across WL in case of QDs capped by (a) GaAs and (b) InGaAs layer. (c) TEM Cross-section image of wetting layer for GaAs-capped sample with evolution of image contrast.

QD composition. The In core presents an inverted-triangle shape as it has been already reported elsewhere [Liu 00, Lenz 02].

Study of In profile in the wetting layer reflects intermixing mechanisms between In and Ga occurring during or after growth. As shown on the figure 3.15(a), In profile is not homogeneous: above GaAs buffer layer, a first layer with an In content < 10% argues diffusion of Ga from the substrate to the QDs. Then a thin layer (2 nm) with around 30% of In can be attributed to the WL by itself. Finally a thicker layer shows a negative gradient of In composition from 10% to 0%, and testifies of In segregation phenomenon during the growth. In-profile is similar for sample with InGaAs capping, except that last layer is thicker (~5 nm) and richer in In due to the deposition of InGaAs capping layer. We notice that maximum

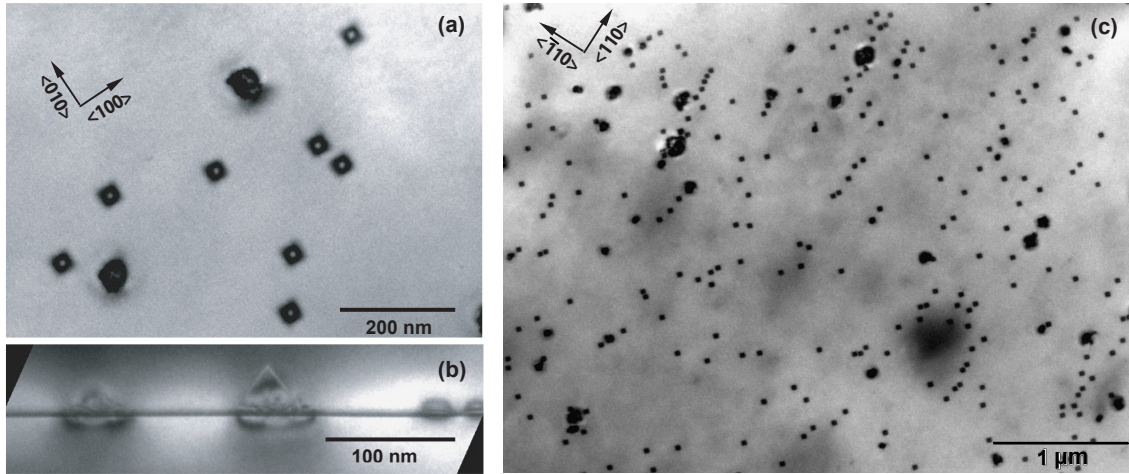


Figure 3.16: (a) and (c) plan view and (b) cross section images of QDs grown at low InAs growth rate (0.0015 ML/s) and capped by GaAs.

of In composition is higher for the GaAs-capped sample than for InGaAs-capped sample. This is surprising since InGaAs is expected to reduce In segregation and thus preserve In content in the WL.

Figure 3.16 shows large area plan-view and cross sectional images of QDs capped by GaAs. The dot density of $17 \cdot 10^8$ dots/cm² is similar to the density measured by AFM on an uncapped grown under the same conditions. The QDs have a square base and a mean width of 37.5 nm (36nm) with a standard deviation of 0.3 nm (1.4 nm) along $\langle 100 \rangle$ ($\langle 010 \rangle$) axis, respectively. This shows a very good size homogeneity. Besides, we observe on figure 3.16, that QDs have tendency to align along $\langle 110 \rangle$ direction. This is not conform to the preferential alignment along $\langle 100 \rangle$ which was predicted and observed for pyramidal QDs with base sides along $\langle 100 \rangle$ and $\langle 010 \rangle$ axis as well [Shchukin 99]. Besides, we observe that about 30% of QDs are dislocated and formed large clusters with nonuniform shape as we can see on figure 3.16(b). QD size appears to reach a critical value above which plastic relaxation happens. Then, under these growth conditions, attachment of adatoms to existing islands is favored as opposed to nucleation of new islands, even if it leads to the formation of relaxed clusters. The self size-limiting effect that has been observed in Ref. [Mukhametzhanov 99, Kaizu 01] seems here to be overcome by faster aggregation of adatoms.

Lastly, we note that the formation of these large clusters may also partially contribute to

the abrupt decrease of the dot density observed in figure 3.12(b), by consuming In adatoms.

3.5 Conclusion

In this chapter, a method to grow low density QDs emitting at 1300 nm at low temperature has been developed. A combination of very low InAs growth rate and an InGaAs capping layer has been used. QDs exhibit a larger size and higher In content than typically observed on InAs/GaAs quantum dots. Presence of a large proportion of dislocated clusters with a remarkable size homogeneity of coherent islands suggest that QD dimension reached a thermodynamic limit. Further incorporation of adatoms into the islands gives rise to plastic strain relaxation and formation of dislocations.

4

Characterization of QD ensembles

In the previous chapter, we have shown that a strong reduction of the InAs growth rate results in a decrease of the areal QD density. In this chapter, optical properties of these low density InAs/GaAs quantum dots (LDQDs) are investigated by means of photoluminescence (PL) at high excitation density, temperature-dependent photoluminescence, and time-resolved photoluminescence (TRPL) experiments. Luminescence efficiency, radiative properties of QD electronic states, and particularly the role of the wetting layer (WL) will be first studied by comparison with high density QD samples. Then, carrier relaxation and recombination processes will be investigated by time-resolved photoluminescence. Finally, temperature stability is examined.

4.1 Comparative studies

In very low density QDs, the filling behavior of QD states for increasing pump power is presumably different due to the low density of states. Moreover, it may be argued that the large interdot distance increases the capture time from the WL to the QDs, creating a “capture bottleneck” and reducing the radiative efficiency. In the following these issues will be addressed by continuous-wave and time-resolved PL experiments on different area densities, as a function of excitation power.

A series of samples with different InAs growth rates was grown. QDs were obtained by depositing 2.1 ML of InAs on a 500 nm-thick GaAs buffer. We varied the InAs growth rate in the range of 0.0012-0.16 ML/s. InAs QDs were then capped by 100 nm-thick GaAs

layer. Under the same growth conditions, a sample was also grown at low growth rate (0.0015 ML/s), with 5 nm-thick $\text{In}_{0.15}\text{Ga}_{0.85}\text{As}$ capping layer to test the influence of the capping layer.

4.1.1 Photoluminescence experiments

The experimental setup used for photoluminescence experiment at high excitation power has been presented in section 2.7. Figures 4.1(a), (b), (c), report PL spectra measured at low temperature (LT) on GaAs-capped QDs grown at 0.015 ML/s, 0.0015 ML/s and 0.0007 ML/s respectively, at different excitation intensities. The ground state (GS) and the two first excited states (ES) signals are well separated. QDs with lower area density present a saturation of the GS intensity and an increase of the ES and WL intensities at lower pump powers in comparison to the higher-density QDs due to the lower number of states. As expected, the saturated GS intensity also increases with the area density.

From these spectra we extract the evolution of the WL emission wavelength for different InAs growth rates presented in figure 4.2(a). We observe a redshift of about 12 nm between low and high growth rate which could be due to a reduced WL thickness at low growth rate. This suggests that mass transport from WL to the QDs is more important at low growth rates. The emission wavelength of the 2D layer (WL + capping layer) of LDQDs covered by InGaAs layer, also shown (black rectangle) in figure 4.2(a), is strongly red-shifted by about 65 nm, due to the increasing effective well thickness as observed by transmission electron microscopy.

We now turn to the investigation of the carrier capture from WL to QDs for low area densities. In figure 4.1, the WL emission is clearly more intense for low-density samples. We address the question of this is only due to the lower density of states, or also to a capture bottleneck in the WL (i.e. carriers would spend a longer time in the WL even if all QDs are not filled). Figure 4.2(b) shows the ratio of WL to GS intensities as a function of pump power density. The WL/GS ratio increases with pump power for all samples, due to saturation of QD states, and is larger for low-density samples where saturation occurs at lower powers. However, as shown in the inset of figure 4.2 for the low-density ($17 \cdot 10^8$ dots/cm²) InGaAs-capped sample, the WL/GS ratio tends to zero as the pump intensity is reduced. This proves that the capture time from the WL to the QD is still much shorter than the interband recombination time even in the lowest QD densities explored here. This result is important in view of the realization of efficient single-photon emitters,

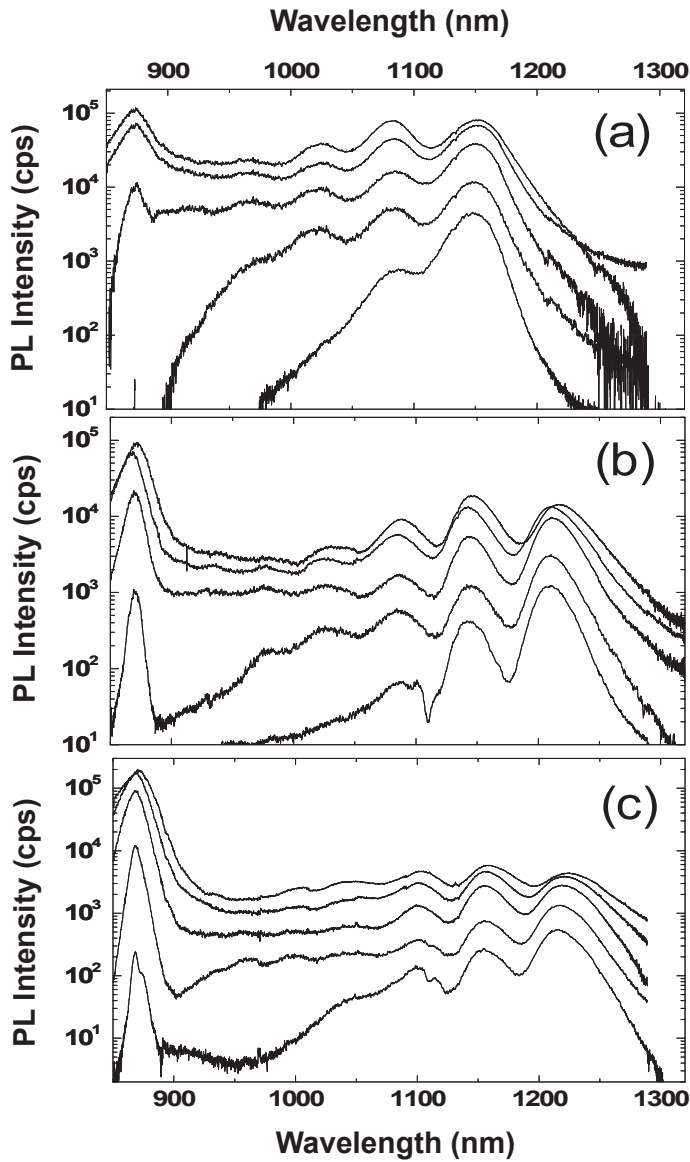


Figure 4.1: PL emission at 12K from GaAs capped-QDs grown with different InAs growth rate: (a) 0.015 ML/s, (b) 0.0015 ML/s. (c) 0.0007 ML/s. Excitation intensity varies between 900 W.cm^{-2} and 300 kW.cm^{-2} .

since a capture bottleneck in the WL would reduce the QD PL efficiency and strongly affect the emission properties of single excitons. Nevertheless, we note that a relatively strong WL emission is observed for excitation levels well below those corresponding to the saturation of QD confined states. This suggests a mechanism for carrier re-excitation from the QD state to the WL which is a function of carrier density (e.g. Auger effect).

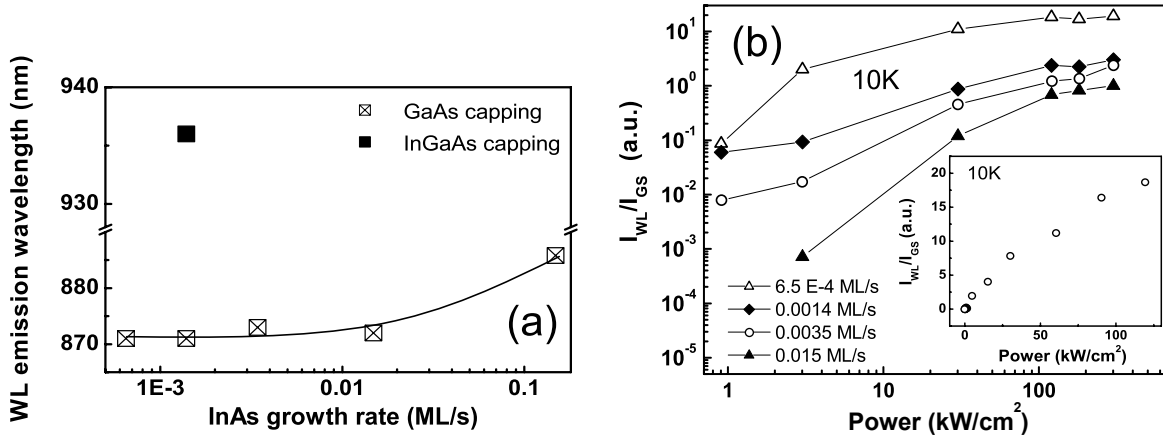


Figure 4.2: (a) Wetting layer emission wavelength as function of the InAs growth rate. The solid line is a guide to the eye. (b) Ratio between WL and GS PL integrated intensities at different InAs growth rate and as function of excitation power. Inset: Ratio between WL and GS PL integrated intensities as function of excitation power on the sample with InGaAs capping layer, on a linear scale.

4.1.2 Time-resolved photoluminescence experiments

The carrier relaxation and recombination processes in the LDQDs have been investigated through TRPL measurements. A sketch of the setup is shown in the section 2.8. The pump power was chosen so that the GS peak was far from saturation and the detection wavelength was set to correspond to the GS PL maximum using different bandpass filters with 12 nm width. The inset of figure 4.3(a) shows the measured PL transients for different growth rates at low temperature (12K). The rise dynamic for the high growth rate sample is limited by the temporal resolution of the setup (600 ps), however we observe an interesting delay of the GS luminescence for the low-density samples. As the GS is well below saturation at this excitation density, the delay cannot be related to carrier refilling from ES, as commonly observed in QD ensembles [Raymond 96]. Figures 4.4 and 4.5 show, behavior of the delay as function of the detection wavelength, temperature and excitation powers. On figure 4.4 we observe that the intensity of this delay can be very important depending on the GS signal intensity. For a detection wavelength at 1300 nm or at 1275 nm, where PL intensity of GS and first ES is intense, the delay is well distinguishable (the fact that the delay is visible in the ES transient confirms that it does not correspond to a refilling from ES). For a detection

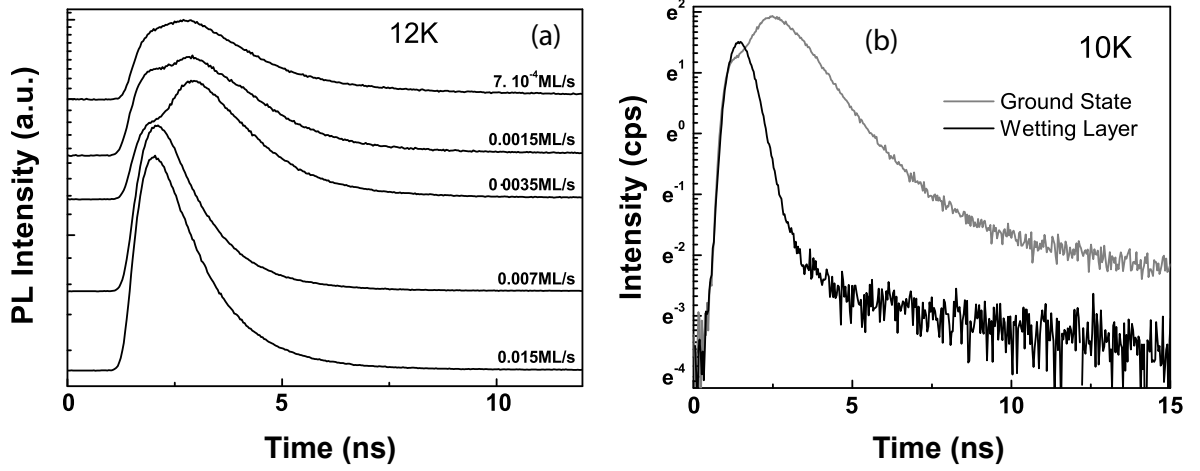


Figure 4.3: (a) TRPL transients measured on QDs capped by GaAs at different InAs growth rates. Excitation energy density: $1.7 \mu\text{J}\cdot\text{cm}^{-2}$ (b) TRPL transients measured on LDQDs (InAs growth rate=0.0015 ML/s) at the GS and WL energy. Excitation energy density: $6 \mu\text{J}\cdot\text{cm}^{-2}$ density

wavelength at 1275 nm and 1325 nm, the transient relative to the GS decay is less and less visible until it seems to disappear for a detection wavelength at 1325 nm.

As shown in figure 4.5(a) this delay disappears when the sample temperature exceeds 150K and at low excitation density (figure 4.5(b)). This would suggest the existence of an activation energy, and of an interaction between carriers in the QDs and carriers in the WL. This interaction would occur at high carrier density in the WL and would become more significant in low-density QDs due to the larger WL population as observed in continuous-wave (CW) PL. The initial part of the dynamic may be related to the emission of GS excitons in the presence of WL spectator carriers, which disappear at longer times, leaving the usual exciton decay. This hypothesis is supported by the observation (figure 4.3b) of WL emission (with ~ 400 ps decay time), under these experimental conditions. Finally we note that the presence of a similar delay is observed for a single quantum dot in the PL transient of the exciton and biexciton in the ground state (figure 4.6). This delay increases with the excitation intensity up to 4 ns and a fast emission appear. Its deconvoluted lifetime has been measured at 0.7 ns. This interaction between GS and WL carriers have not been previously observed to the best of our knowledge and could be a source of multiphoton emission which would limit the ability of QDs to operate as single photon source.

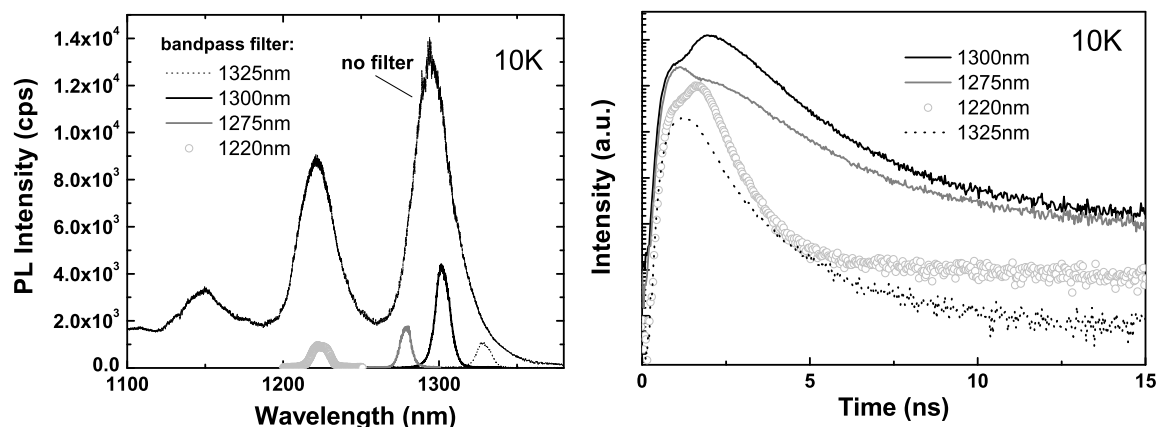


Figure 4.4: (a) PL spectra of LDQDs with different bandpass filters under pulsed excitation power at 80 MHz. (b) Corresponding TRPL transients. Excitation energy density: $2 \mu\text{J}\cdot\text{cm}^{-2}$

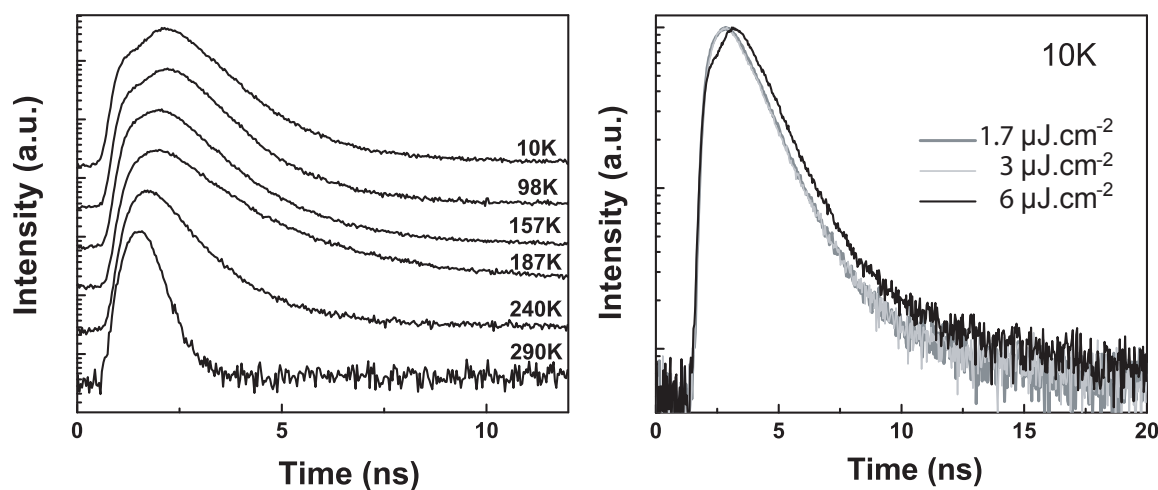


Figure 4.5: TRPL transients of LDQDs (a) at different temperatures (excitation energy density: $6 \mu\text{J}\cdot\text{cm}^{-2}$) and (b) at different excitation powers.

To observe the evolution of the decay time as function of the area QD density, the decay part of the TRPL shown in figure 4.3 was fitted with the convolution between a single-time constant exponential for the signal and the measured setup response function. Decay times are presented on figure 4.7 as function of growth rate. The decay time is observed to increase with increasing QD size. The increase of PL decay time indicates a reduction of the

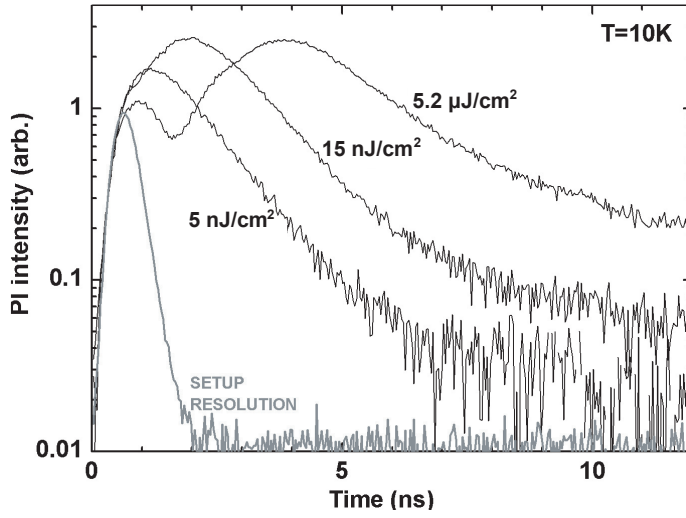


Figure 4.6: TRPL transients on biexciton emission from a single QD for increasing excitation intensity.

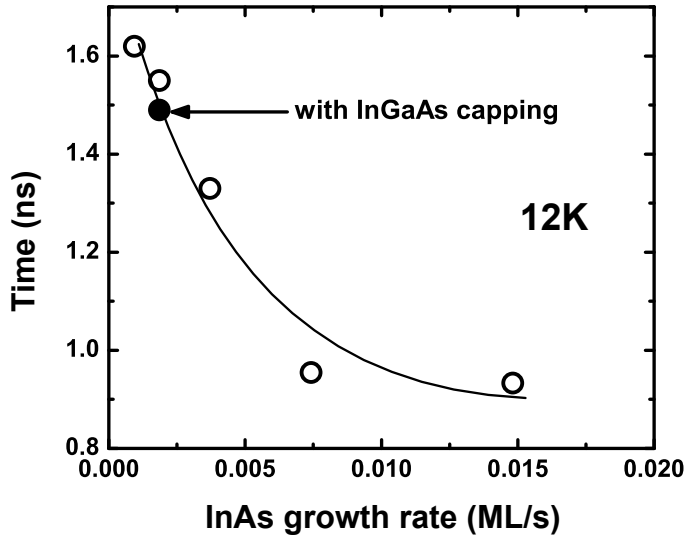


Figure 4.7: Evolution of decay times as function of InAs growth rate. Excitation energy density: $1.7 \mu\text{J}\cdot\text{cm}^{-2}$. The solid line is guide to the eye.

oscillator strength, which is likely related to a reduced electron-hole wavefunction overlap for large QD diameter [Karachinsky 04].

4.2 Temperature dependence

Finally we investigated the temperature stability of LDQD PL emission. PL measurements at different temperatures have been performed on two samples with QDs grown at the same growth rate (0.0015 ML/s) capped by InGaAs or by GaAs. The pump wavelength and the power density were fixed at 780 nm and $6 \text{ kW}\cdot\text{cm}^{-2}$ respectively. At this excitation power,

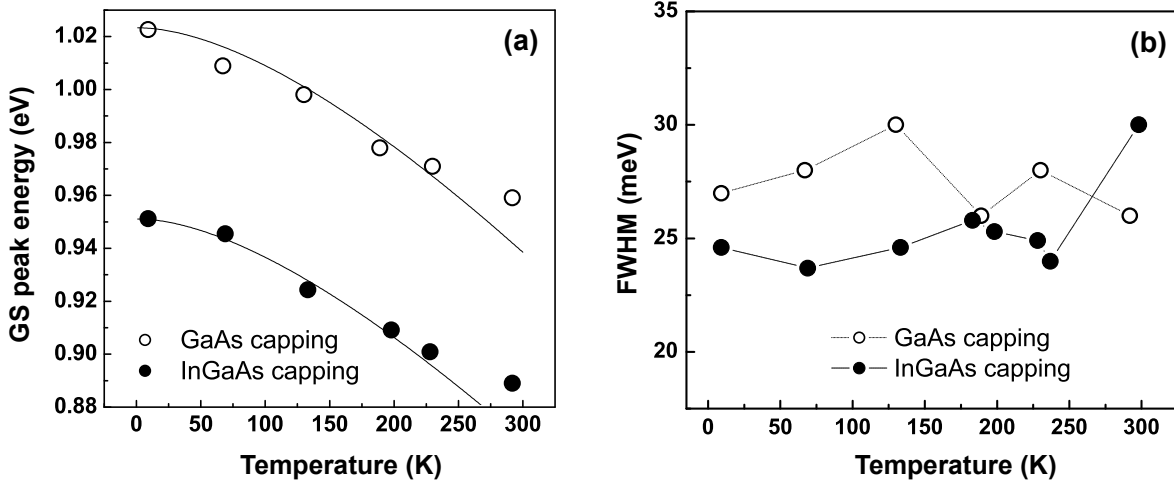


Figure 4.8: (a) Evolution for different temperatures of the GS energy peak. The solid lines show the temperature dependence of the bulk $\text{In}_x\text{Ga}_{(1-x)}\text{As}$ bandgap with $x=0.35$ and 0.41 , following Ref. [Paul 91]. (b) Evolution of the FWHM of the GS peak.

first ES is populated and GS is not saturated. Figure 4.8 shows the evolution of the GS peak energy and the FWHM as a function of temperature. Temperature dependence of PL integrated intensity (including intensity from GS and excited state signals) is presented on figure 4.9. The peak shift is similar for both samples with a redshift of 64 meV between 10K and 300K as shown on figure 4.8(a). We fit this red-shift with the empirical relation [Paul 91] for the temperature dependence of $\text{In}_x\text{Ga}_{(1-x)}\text{As}$ bandgap, with $x=0.35$ and 0.41 for the GaAs-capped and InGaAs-capped QDs respectively. For comparison, TEM measurements indicate a mean In composition of 50.4% and 50.6% for GaAs-capped and InGaAs-capped sample, respectively. In-content inhomogeneity in the QDs, which is not taken into account in Ref. [Paul 91], can explain this composition difference.

FWHM evolution with temperature is similar for the two different capping layers. Its overall variation is smaller than 5 meV ($\sim 20\%$) which highlights the high size homogeneity of the LDQDs [Yamaguchi 02].

We observe on figure 4.9a that PL intensity quenches by a factor of 100 (25) for QDs capped by GaAs (InGaAs) between low and room temperature. We note that the quenching is lower by using an InGaAs capping layer, although the carrier confinement is higher for QDs capped by GaAs. For $T > 100\text{K}$, the temperature dependence of the luminescence intensity can be

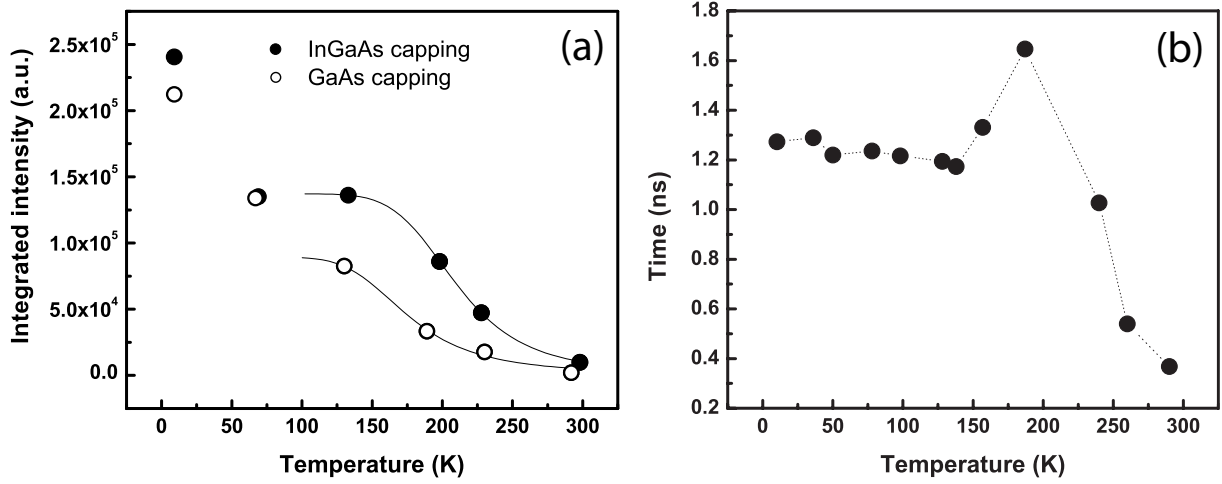


Figure 4.9: (a) Integrated intensity as a function of temperature for InGaAs- and GaAs-capped QDs grown at 0.0015 ML/s, under an excitation density of $6 \text{ kW}\cdot\text{cm}^{-2}$. Fitting curves are represented by the solid lines. (b) Evolution of decay time for QDs capped by InGaAs as function of temperature. Excitation energy density: $6 \mu\text{J}/\text{cm}^{-2}$.

expressed with a single activation energy E_a as:

$$I \propto \frac{1}{1 + B \cdot \exp(-E_a/kT)}$$

The fits provide E_a values of 130 meV and 156 meV for QDs capped by GaAs and InGaAs respectively. This activation energy is much smaller than the energy difference between the QD GS and the WL, so that the PL quenching cannot be attributed to the thermal escape of excitons to the WL, contrary to what is observed in smaller QDs [Sanguinetti 99]. Due to the absence of a confining heterostructure around the photoexcited GaAs region, the PL temperature dependence may also reflect the carrier diffusion to non-radiative states on the surface and in the substrate. In order to isolate the intrinsic nonradiative characteristics of QDs, we measured the QD carrier lifetime as a function of temperature. Figure 4.9b shows the measured lifetime at the GS energy of a sample containing LDQDs with InGaAs capping as function of temperature. By comparison with figure 4.3, we used a higher excitation power in this experiment and we observe a shorter lifetime. This can be attributed to an enhancement of Auger recombination process with excitation density [Morris 99]. We observe that the lifetime is independent of temperature for $T < 150\text{K}$, increases up to 1.7 ns at 180K, then decreases to 0.4 ns at RT. This type of behavior has already been reported

and interpreted [Fiore 00, Pulizzi 04, Adler 96]. The temperature independence of the lifetime between 10K and 150K [Wang 94] is a consequence of the quantized energy structure. From this, we can deduce that the reduction of the luminescence intensity observed for temperatures below 100K, is rather due to carrier capture by defects before recombination in the QDs than to nonradiative recombination in the QDs. The subsequent increase of the lifetime with temperature can be attributed to thermal population of a dark exciton state [Yang 97, Gurioli 06] consisting of an electron in the GS and a hole in the ES. At temperature above 200K, the PL-decay time drops due to the enhanced influence of nonradiative recombination channels, which confirms the existence of non-radiative recombination channels thermally activated for $T > 150\text{K}$, as also observed in continuous-wave PL. Asymmetric escape of hole or electron could contribute to the reduction of the lifetime.

4.3 Conclusion

PL investigations of QDs grown at different InAs growth rates and a study of the relative intensity of GS and WL signals show an efficient carrier capture mechanism into the QDs even for densities as low as few QDs/ μm^2 . Nevertheless, the effect of WL carriers in LDQDs at moderate excitation densities is evidenced in a complex PL rise dynamics which is not for the moment fully understood and is tentatively associated to the presence of carriers in the WL which becomes more significant in low-density QDs. Temperature dependence measurements performed on LDQDs capped by InGaAs show a good stability of their luminescence intensity and a lifetime evolution, at the GS energy, which is similar to those reported for higher-density QDs samples.

5

Single quantum dot spectroscopy

As described in the previous chapter, the growth of low-density QDs emitting at 1300 nm has been optimized. The study of recombination mechanisms occurring in these QDs and their thermal stability has shown them as reliable light emitter for optoelectronic devices. This chapter will now focus on their possibilities to be used as single photon source. The first part is devoted to the spectroscopy of single QDs. The study of signals corresponding to single electronic transitions in a QD is performed by continuous wave (CW) and time-resolved (TR) photoluminescence experiments. Experiment of antibunching will give further information on the quality of the single photon source through the measure of the second-order correlation function. Finally, the last section gathers first results on single QDs embedded in a microcavity.

5.1 Characterization technique

The microphotoluminescence setup used for the detection of single photons is presented in detail in section 2.5. A beam splitter with a transmission/reflection efficiency of 90%/10% is used at the exit side of the microscope objective to improve the collection efficiency. The spot size is estimated at $\sim 4 \mu\text{m}$. Even with the low QD density that was obtained, this excitation area is too large to detect a signal from a single QD. The following methods have been tested to decrease the background signal:

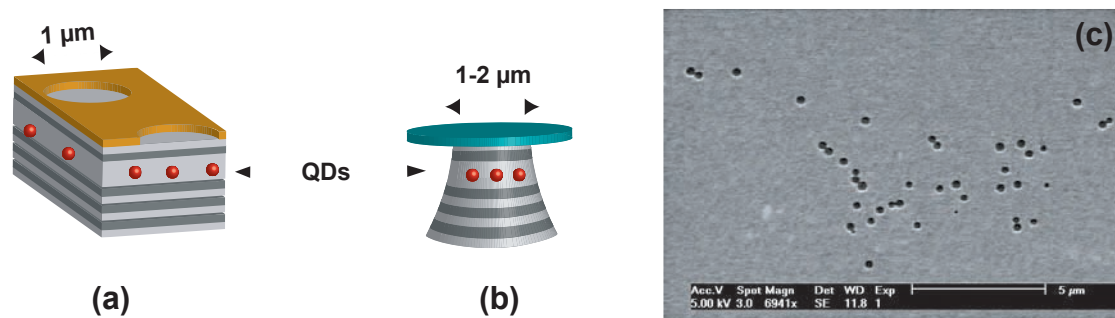


Figure 5.1: Sketch of isolation techniques for single QD spectroscopy: (a) metal aperture, (b) mesa etching. (c) SEM picture of metal apertures with diameter $<1\mu\text{m}$ using mask with polymer-nanospheres.

5.1.1 Isolation of single quantum dot

Metal Aperture (figure 5.1(a)):

The deposition of a thin metal layer on the surface with small apertures of $1\mu\text{m}$ diameter in the metal layer allows for the selection of the emission from a few QDs only. These small apertures have been realized by using polymer nano-spheres deposited on the sample surface by spinning and a subsequent deposition of a thin metal layer. The lift-off technique developed by U. Håkanson [Håkanson 03] was then used to selectively open the metal surface. Nanoapertures with diameter below 500 nm have been obtained using this technique as shown on the figure 5.1(c). Since the QD density in our samples is of the order of $2\cdot\mu\text{m}^{-2}$, an aperture size of $1\mu\text{m}$ is sufficiently small for our purpose. But the random location of the apertures makes their identification difficult in the microPL system. E-beam lithography was rather used to define apertures with diameter ranging between 1 and $2\mu\text{m}$.

Mesa etching (figure 5.1(b)):

The second possibility was to etch mesa of $1\mu\text{m}$ diameter through the active layer. Optical lithography or e-beam lithography have been used to define a mask prior to etching (by wet- or reactive-ion etching) of the mesa.

Both techniques have been tested in the framework of the present study, optical lithography and nanosphere techniques have been done in EPFL, e-beam lithography has been done in CNF-IFN in Rome. No significant difference in PL response was observed between QDs

isolated with these two methods.

5.1.2 Insertion in a microcavity

In a microcavity, the light emitting active region is placed in an optical cavity with a resonance wavelength close to the wavelength of emission. As detailed in section 5.3, when an optical cavity is in resonance with the internal emission, the spontaneous emission process is modified. The result is an increased directionality of the QD emission, a higher extraction efficiency. Also, the cavity resonance allows to control the emission lifetimes; this phenomenon, called Purcell effect, will be discussed later.

The simplest cavity consists of a planar active region sandwiched between two parallel mirrors (Fabry-Perot cavity). The spacing of the mirrors determines the optical resonance modes and can thus be used to “tune” the cavity to the emission wavelength. The reflectors can be constituted by a semiconductor-air interface, metallic reflectors or Distributed Bragg Reflectors (DBRs). This kind of cavities will be employed in the following section. More complex microcavities provide optical confinement in all three dimensions. Preliminary experimental results on micropillar and photonic crystal structures will be presented in the last section.

5.2 Characterization of single quantum dots

Low-density QDs were incorporated at the center of an epitaxied $1-\lambda$ microcavity with a 13.5 pair (1 pair) $\text{Al}_{0.9}\text{Ga}_{0.1}\text{As}/\text{GaAs}$ bottom (top) Bragg mirror respectively. This resulted in a 13-fold increase in the PL signal collected into the microscope objective as shown on the figure 5.2. $1\ \mu\text{m}^2$ mesas were processed by photolithography and wet etching to isolate QDs. Mesa etching provides a lateral confinement. However, the quality factor in such structure is low so that the effect of the confinement on the emission wavelength is negligible. A Ti-Sa laser emitting at 835 nm was used as a pump source. Single-QD spectroscopy under optical pumping has been performed by Carl Zinoni.

5.2.1 Pump power dependence

PL spectra at 10K obtained on one of these mesas are presented in figure 5.3 for different excitation powers. We selected a mesa showing two sets of lines, corresponding to the

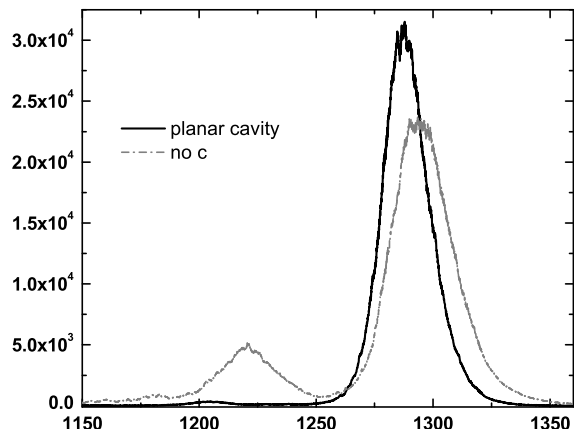


Figure 5.2: (a) SEM cross-section picture of the planar cavity used for single photon spectroscopy (b) PL spectra on QD ensemble (10K) evidencing the luminescence enhancement caused by the microcavity.

emission of two single QDs, noted as QD1 and QD2, which highlights the consistency of the observed behavior and the reproducibility of the QD emission.

Two sharp lines at 957.9 meV and 956.8 meV can be attributed to exciton (X) and biexciton (XX) recombinations, respectively, in a single QD (QD1), as evidenced by their excitation power dependence: at very low pump power only the X line is present, this line corresponds to the recombination of a single electron-hole pair in the ground state of the QD (figure 5.4(a)). With increasing excitation power, the XX line appears, it corresponds to the recombination of an electron-hole pair when two electron-hole pairs are present in the ground state (figure 5.4(b)). Exciton and biexciton recombination energies are different due to the coulomb interaction between the carriers. The same behavior is observed in QD2 for the two peaks at 953.4 meV and 952.7 meV . The integrated intensities of X and XX lines of QD1 are plotted in figure 5.5 as a function of the excitation power. Ideally, the intensity of X signal is proportional to the probability of injection of a single electron-hole pair and this probability increases linearly with the power in the low excitation regime. Concerning the XX signal intensity, it is proportional to the probability of injection of two electron-hole pairs and thus, it is expected to increase quadratically with the excitation power. At low excitation power, we observe that the PL intensity dependence on the laser

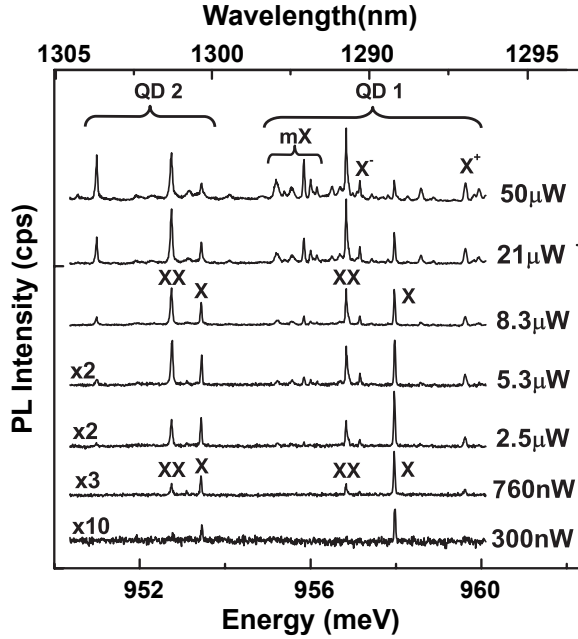


Figure 5.3: PL spectra (10K) of QDs embedded in a microcavity ($1\mu\text{m}$ -diameter mesa) at different excitation powers. Peaks X and XX are attributed to exciton and biexciton emission.

power P can be fitted (lines) by the relation $I_{X,XX} \propto P^n$, with $n=0.71$ and 1.4 for X and XX lines respectively. The deviation from the ideal linear and quadratic dependencies has been observed before in QDs capped with InGaAs [Kaiser 02] and GaAs/AlAs type II superlattices [Nakayama 95] and has been interpreted in terms of fast scattering processes induced by defects and impurities. However the fact that $I_{XX} \propto I_X^2$ (see inset in figure 5.5) confirms that the XX line corresponds to biexciton emission.

At high excitation power, we observe that X intensity saturates, which corresponds to the regime where one electron-hole pair is injected per exciton lifetime. If we further increase the excitation power, X peak intensity decreases because the injection rate is higher than the exciton recombination rate and the probability to have one electron-hole pair in the ground state decreases. The same phenomenon occurs for the XX line. A quantitative description of the recombination mechanism as function of the excitation power through a rate equation model can be found in the PhD thesis of E. Moreau [Moreau 02]. The biexciton binding energy of about 1 meV falls within the wide range reported for self-organized In(Ga)As/GaAs QDs (from negative values up to about 5 meV [Rodt 03]) as determined by the balance of Coulomb interaction, correlation and exchange. For higher excitation power, other sharp lines appear. On the basis of their energy position [Landin 99, Kiraz 02] two of them can be attributed to negative (X^-) and positive (X^+) charged excitons (figure 5.4(c)). Moreover, we observed on several mesas other lines (mX) which appear concomitantly with the

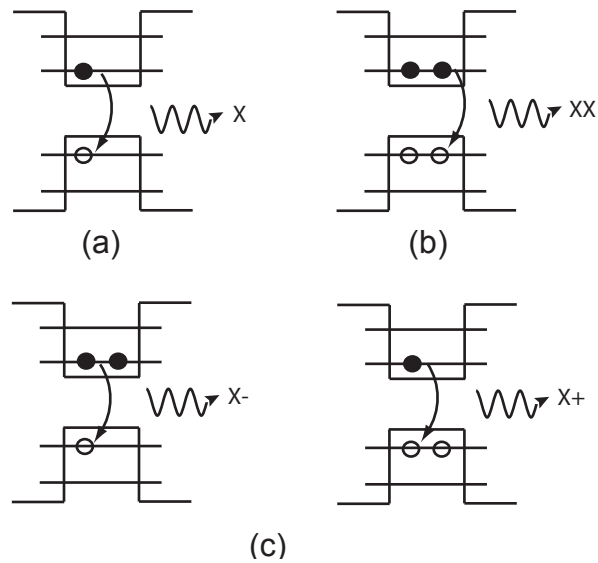


Figure 5.4: Recombination in a single quantum dot: (a) exciton, (b) biexciton, (c) charged (positively and negatively) exciton.

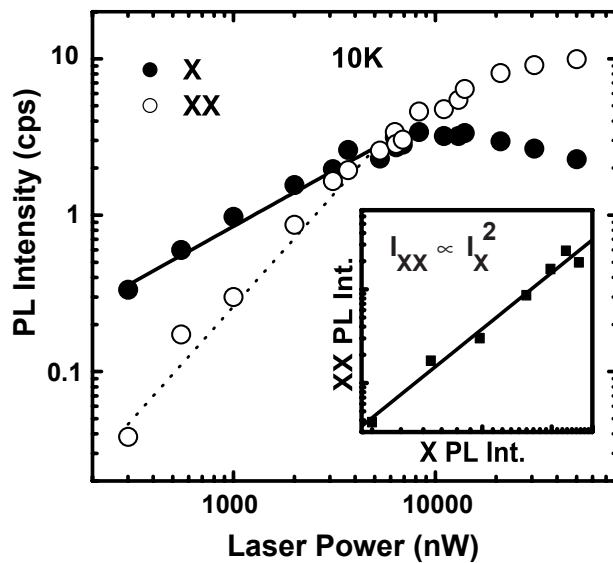


Figure 5.5: Integrated intensities of X and XX peaks as a function of the laser excitation power, under continuous wave excitation. Solid (dashed) line shows the fitted power dependence of X (XX) intensity and the inset reports the dependence of the XX-PL intensity versus the X-PL intensity in log-log scale.

excited state emission and can therefore be attributed to multiexciton emission [Finley 01]. The ensemble of these observations confirms that the emission of a single QD in the 1300 nm region is clearly identified.

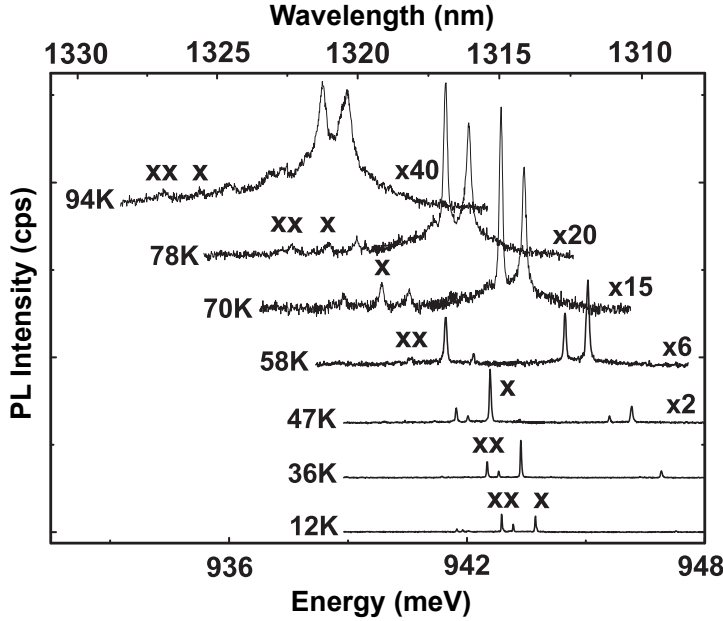


Figure 5.6: PL spectra of a single QD in a microcavity (1 μm -diameter mesa) at different temperatures (excitation power=1 μW , pump wavelength=850 nm).

5.2.2 Temperature dependence

We further investigated the temperature stability of the single QD emission. Figure 5.6 presents PL spectra obtained on a 1 μm -diameter mesa at different temperatures: Sharp lines arising from discrete electronic states are seen at temperatures well above 77K. As the temperature is raised, the X linewidth increases from 36 μeV (12K, resolution-limited) to 160 μeV (70K), due to phonon-induced homogeneous broadening [Bayer 02]. Moreover, the charged exciton lines increase at the expense of the X line, as previously reported [Karlsson 02].

5.2.3 Time-resolved experiment

Another way to make the distinction between exciton and biexciton signal is to study their evolution in time-resolved photoluminescence. Details about the setup are given in section 2.5. and Ref. [Zinoni 06]. Figures 5.7(a) and (b) show PL spectra of a single QD as function of pulsed excitation power a 80 MHz and the corresponding lifetime measurements on the exciton and biexciton lines. A fiber-coupled bandpass filter (tunable between 1270 and 1310 nm with a full width at half maximum (FWHM) of 0.8nm) is used for selecting the excitonic emission. The black lines in figure 5.7 show the least square fits to the decaying part of the PL for the X and XX after dark noise subtraction. The delay in the onset of

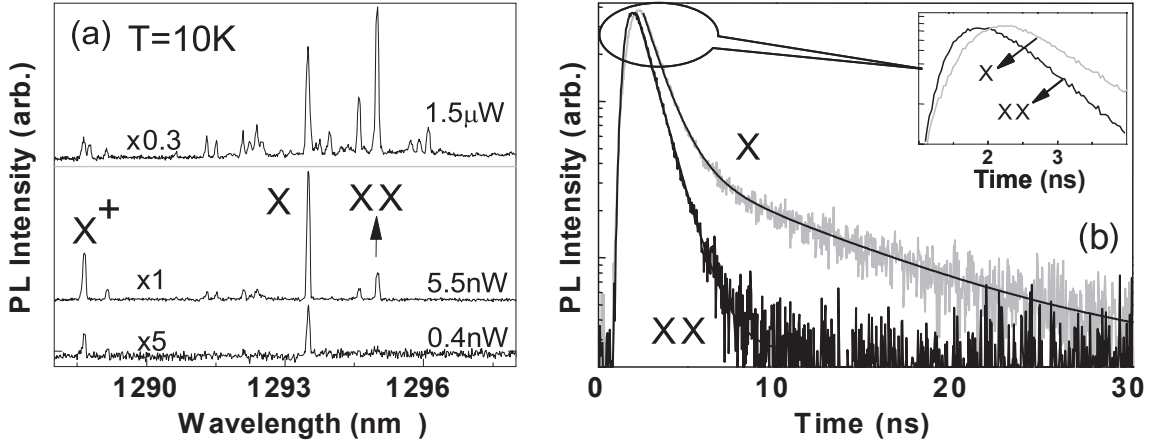


Figure 5.7: (a) PL spectra of the single QD used for time-resolved PL measurement (b) Lifetime measurements of the exciton (X) and biexciton (XX) with fits (black solid lines). The inset is a detailed view of the initial dynamics. [Zinoni 06]

the decay of the X emission compared to the XX one is evidence for cascade emission and validates the peak assignment (inset of Fig 5.7(b)). The exciton lifetime is characterized by a double exponential decay of 1.1 and 8.6 ns: the fast component derives from the recombination of a bright exciton (figure 5.8(a)), while the slower decaying part suggests the presence of a dark exciton state (figure 5.8(b)) that is repopulating the allowed exciton transition [Patton 03, Finley 01]. A measurement of the temperature dependence of the exponential decay will be required to validate this conclusion. The XX decay time was measured to be 1.0 ns. The ratio of 1.1 between the exciton and biexciton lifetimes is consistent with previous studies on single QDs [Bacher 99].

5.2.4 Antibunching experiment

Principle

Single QD emission has been clearly identified, however, antibunching experiment is required to prove that the QD emit photons one by one. Moreover, the second-order correlation function $g^{(2)}(\tau)$ is used to characterize the quality of the single photon sources. In semiclassical theory, it is defined as [Teich 88]:

$$g^{(2)}(\tau) = \frac{\langle I(t)I(t+\tau) \rangle}{\langle I(t) \rangle^2} \quad (5.1)$$

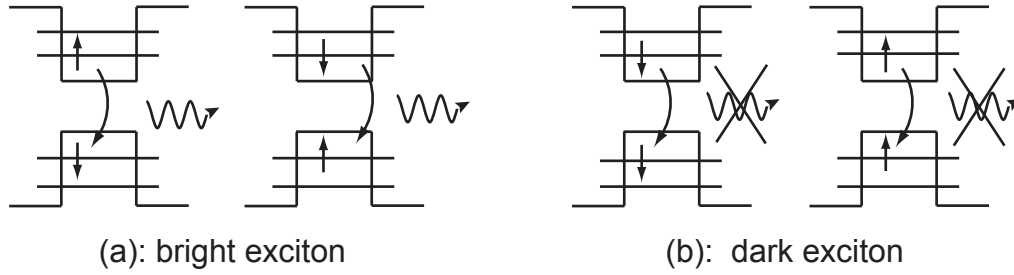


Figure 5.8: Scheme of the different states of an exciton. (a) bright exciton (total angular momentum= ± 1): the recombination is radiative. (b) dark exciton (total angular momentum= ± 2): the recombination is non radiative.

with $I(t)$ being the intensity at time t and $\langle \rangle$ indicates averaging over t . This expression satisfies the following inequalities :

$$g^{(2)}(0) \geq 1 \quad (5.2)$$

$$g^{(2)}(\tau) \leq g^{(2)}(0) \quad (5.3)$$

A classical beam of coherent light (a laser for example), will have a constant correlation function $g^{(2)}(\tau) = 1$, while a thermal light has $g^{(2)}(0) = 2$

In quantum theory, the electromagnetic field is described using operators rather than algebraic quantities and the correlation function is defined as:

$$g^{(2)}(\tau) = \frac{\langle \hat{a}^\dagger(t) \hat{a}^\dagger(t+\tau) \hat{a}(t+\tau) \hat{a}(t) \rangle}{\langle \hat{a}^\dagger(t) \hat{a}(t) \rangle^2} \quad (5.4)$$

Where \hat{a} and \hat{a}^\dagger are the annihilation and creation operators, respectively. In this approach, an infringement of inequalities (1.2) and (1.3) is allowed. A correlation function $g^{(2)}(\tau) = 1$ means that the probability of coincidence of a photon emission at time t and another one at $t + \tau$ equals the product of probabilities of an event at each time i.e. the two events are uncorrelated. The situation $g^{(2)}(\tau) < 1$ corresponds to a situation where the probability to detect a photon is lower, when a first photon has been previously detected. Photons are thus *antibunched*, which is not allowed by the semi-classical theory. The observation of antibunching effect thus provided an unarguable evidence of the quantum theory of light [Kimble 77].

At zero delay, the correlation function $g^{(2)}(0)$ for a single mode field is given by [Loudon 83]:

$$g^{(2)}(0) = \frac{\langle \hat{a}^\dagger \hat{a}^\dagger \hat{a} \hat{a} \rangle}{\langle \hat{a}^\dagger \hat{a} \rangle^2} = \frac{\langle \hat{n}(\hat{n} - 1) \rangle}{\langle \hat{n} \rangle^2} \quad (5.5)$$

Where \hat{n} is the photon number operator. Indeed, an ideal single-photon emitter produces a Fock state $|1\rangle$ such that $\hat{n}|1\rangle = |1\rangle$ and therefore has $g^{(2)}(0) = 0$.

A 2-photons source produces a Fock state $|2\rangle$, which corresponds to a $g^{(2)}(0) = \frac{1}{2}$.

We deduce from this that a source with a $g^{(2)}(0) < 0.5$ can be called a *single photon source*.

Practically, the $g^{(2)}(0)$ is measured using the Hanbury-Brown and Twiss setup [Hanbury-Brown 56] where the light is split in two modes 1 and 2 by a 50/50 beamsplitter, and two single photon detectors are placed in the two exit arms. This allows measuring the autocorrelation function by counting coincidences of detection events on the two detectors.

Anticorrelation measurement

The experimental setup is the same as for the time-resolved photoluminescence experiment excepted that the QD emission is sent to a 50/50 fibre beam-splitter and then to two single-photon InGaAs avalanche photodiodes (APD). Scheme of the setup is shown in figure 5.9. When a laser pulse excites a QD, a single photon is emitted and collected by one of the two APDs, this starts the data acquisition. When a second photon is detected after a second excitation pulse it is recorded as a “stop”. Numerous repetitions of this measurement constitute an histogram of the coincidence detection events as a function of the delay, in multiples of the laser repetition period. A careful gating of the APDs was necessary to maximize the signal-to-noise ratio (SNR), since InGaAs APDs present a much higher dark count rate as compared to the equivalent silicon modules. The histogram of coincidences as a function of delay is shown in figure 5.10 for a pump power of 0.6 nW, 2.5 nW and 350 nW. The $g^{(2)}(0)$ is extracted as the ratio of zero-delay coincidences and the average of coincidences at multiples of the laser period. At 0.6 nW, a $g^{(2)}(0) = 0.38$ is measured which is a strong evidence that on average the QD is emitting less than two photons per pulse. By deducing the SNR (dark counts are estimated with the laser switched off) $g^{(2)}(0)$ is reduced to 0.24. The remaining correlation counts are attributed to stray light entering the setup and imperfect filtering. At higher excitation power $g^{(2)}(0)$ becomes higher than 0.5. At these powers, PL emission becomes broader due to the presence of multi-exciton states, presumably related to the presence of carriers in higher-energy states, including the wetting

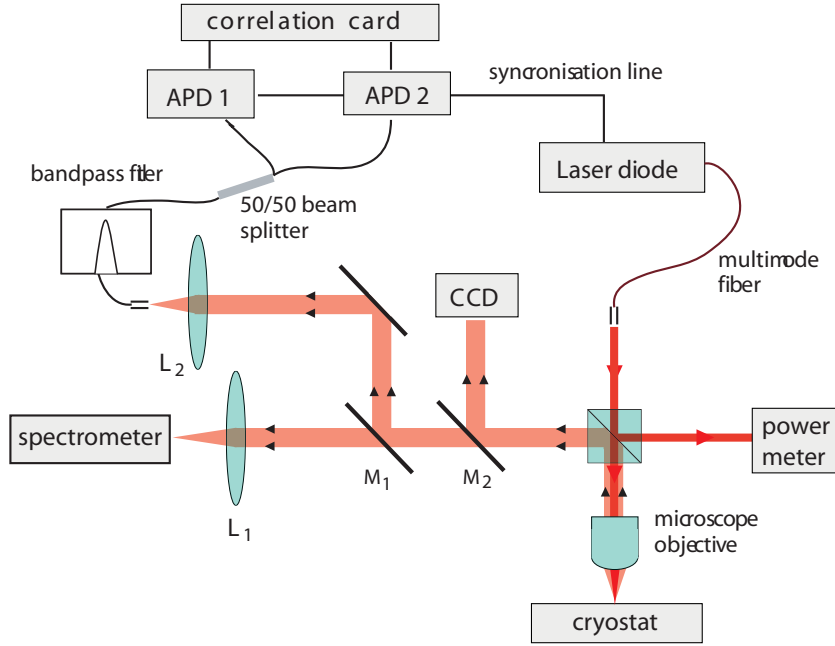


Figure 5.9: Sketch of the experimental setup used for anticorrelation experiment.

layer which superpose to the X, XX, and charged X lines. The same observation was made at elevated temperature ($>50\text{K}$) [Zinoni 06]. This stray emission increases the $g^{(2)}(0)$ and thus limits the operating temperature of QD-based single-photon sources. Its effect may be reduced by resonant pumping, to avoid generating carriers in the WL, or a careful tuning of the charge state in and around the QD.

5.3 Insertion of low-density quantum dots in a high quality factor microcavity

5.3.1 Spontaneous emission in a microcavity in the weak coupling regime

Spontaneous emission can be described correctly only by the quantized theory of electromagnetic field. Semiclassically, it can be described as an emission “stimulated” by a “vacuum” electric field related to the non-zero energy of the electro-magnetic ground state. From the quantized theory, the vacuum field in a material with refractive index n is given by $E_{vac} = \sqrt{\frac{\hbar\omega_0}{2\epsilon_0 n^2 V_c}}$, with $V_c = \frac{\int \int \int |E(r)|^2 d^3r}{|E|_{max}^2}$ is the effective cavity volume. The SE rate can

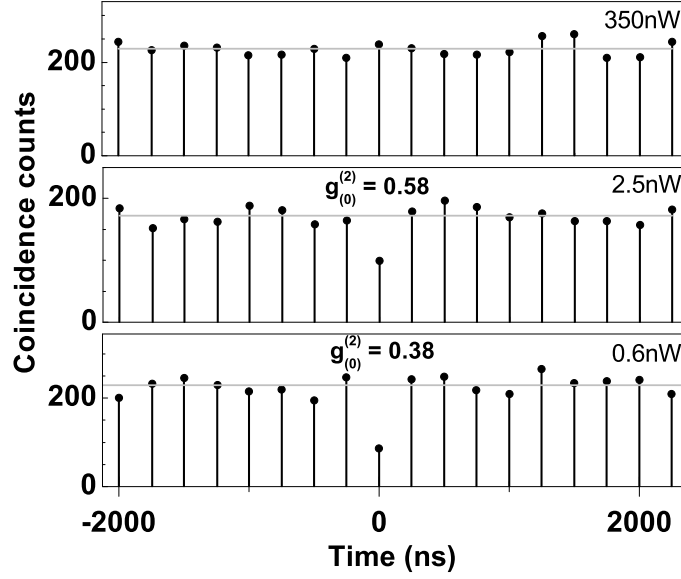


Figure 5.10: Coincidence counts as a function of delay at various pump powers (P corresponds the saturation power of the exciton) on the X line of a QD having similar spectral features as the QD shown in figure 5.7 [Zinoni 06].

then be calculated as the transition rate due to an electric field $E_{vac}(\vec{r}, t)$ corresponding to the vacuum fluctuation in the cavity. If we consider an exciton in a QD having two states $|i\rangle$ and $|f\rangle$ separated by an energy $\Delta E = E_f - E_i = \hbar\omega_0$, the transition probability per unit time can be derived from Fermi's golden rule as:

$$\frac{dP}{dt} = \frac{2\pi}{\hbar} |W_{if}|^2 \rho(\omega_0) \quad (5.6)$$

with $\rho(\omega)$ is the optical density of states and W_{if} is the matrix element of the perturbation. In the electric dipole approximation we can write: $|W_{if}| = \langle i | -\vec{D} \cdot \vec{\epsilon} | f \rangle = -\vec{D}_{if} \cdot \hat{\epsilon}(\vec{r}) E_{vac}$ with \vec{D} is the dipole moment, and $\hat{\epsilon}(\vec{r})$ is the spatial dependence of the electric field. The SE rate is then given by:

$$\frac{1}{\tau} = \frac{dP}{dt} = \frac{\pi}{\hbar\epsilon_0} \frac{\omega_0}{n^2 V_c} |\vec{D}_{if} \cdot \hat{\epsilon}(\vec{r})|^2 \rho(\omega_0) \quad (5.7)$$

For the case of emission in a homogeneous bulk medium, with refractive index n , the density of states is $\rho(\omega) = \frac{\omega^2 n^3 V_c}{\pi^2 c^3}$. Thus we have:

$$\frac{1}{\tau_{bulk}} = \frac{n\omega_0^3}{\pi\hbar\epsilon_0 c^3} \langle |\vec{D}_{if} \cdot \hat{e}(\vec{r})|^2 \rangle \quad (5.8)$$

$\langle |\vec{D}_{if} \cdot \hat{e}(\vec{r})|^2 \rangle$ represents the average over the polarization of all the possible cavity modes.

We have:

$$\langle |\vec{D}_{if} \cdot \hat{e}(\vec{r})|^2 \rangle = \frac{|D_{if}|^2}{3} \text{ and } \frac{1}{\tau_{bulk}} = \frac{n\omega_0^3}{3\pi\hbar\epsilon_0 c^3} |D_{if}|^2$$

This is the usual expression for the spontaneous emission lifetime in the absence of cavity effects. We observe that it does not depend on the volume V_c .

In contrast, in a microcavity with well separated modes (frequency spacing between the cavity modes is larger than their linewidth), optical density of states can be written as:

$$\rho(\omega) = \frac{2}{\pi\Delta\omega_c} \frac{\Delta\omega_c^2}{4(\omega - \omega_c)^2 + \Delta\omega_c^2} \quad (5.9)$$

assuming that the optical mode has a lorentzian lineshape centred at ω_c with a FWHM $\Delta\omega_c$.

Then we obtain a cavity lifetime:

$$\frac{1}{\tau_{cav}} = \frac{2}{n^2\hbar\epsilon_0 V_c} \frac{\omega_0}{\Delta\omega_c} |\vec{D}_{if} \cdot \hat{e}(\vec{r})|^2 \frac{\Delta\omega_c^2}{4(\omega_0 - \omega_c)^2 + \Delta\omega_c^2} \quad (5.10)$$

The term $|\vec{D}_{if} \cdot \hat{e}(\vec{r})|^2$ corresponds to the coupling between the emitter and the electric field. When the field is maximum at the emitter position and is parallel to the dipole moment, then $|\vec{D}_{if} \cdot \hat{e}(\vec{r})|^2$ reaches its maximum value $|D_{if}|^2$. At resonance, the emitter frequency (ω_0) equals the mode frequency (ω_c), and thus:

$$\frac{1}{\tau_{cav}} = \frac{2}{n^2\hbar\epsilon_0 V_c} \frac{\omega_c}{\Delta\omega_c} |\vec{D}_{if} \cdot \hat{e}(\vec{r})|^2 \quad (5.11)$$

Now, if we compare the maximum SE rate in a cavity mode with SE rate obtained in a bulk material, we obtain:

$$\frac{\tau_{bulk}}{\tau_{cav}} = \frac{3}{4\pi^2} \left(\frac{\lambda_0}{n}\right)^3 \frac{Q}{V_c} \frac{|\vec{D}_{if} \cdot \hat{e}(\vec{r})|^2}{|D_{if}|^2} \quad (5.12)$$

The factor $F_p = \frac{3}{4\pi^2} \left(\frac{\lambda_0}{n}\right)^3 \frac{Q}{V_c}$ is called Purcell factor and has been defined in 1946 [Purcell 46]. It varies with the inverse of the effective cavity volume V_c and with the quality factor $Q = \frac{\omega_c}{\Delta\omega_c}$. These calculations are correct when the spectral width of the emitter on resonance is smaller than the mode width.

Moreover the perturbation approach which is the basis of equation 5.6 is valid in the weak coupling regime, when the emitter is coupled to a continuum of modes or when the escape time in the cavity is shorter than the coupling time (Rabi period) between emitter and confined field. This implies that the emitted photon escapes from the cavity before being reabsorbed. The process is then irreversible.

5.3.2 Micropillar

With a confinement of light in only one dimension, such as a planar microcavity having a mirror separation larger than $\lambda/2$, the increase in the spontaneous emission rate is at most a factor of 3 [Abram 98]. Confinement in two or three dimensions is required to increase this factor. Microcavity structures such as microdisks [Kiraz 01, Vuckovic 03, Peter 05], micropillars [Reithmaier 04, Moreau 01a] or photonic crystals [Badolato 05, Englund 05, Yoshie 04] are commonly used. In this section, preliminary results on low-density QD embedded in a micropillar structure are presented. More detailed studies are under way.

Structure

The studied micropillar structure consists of an active region with low density QDs emitting at 1300 nm embedded between 25 (15) bottom (top) AlGaAs/GaAs DBRs.

DBRs consist in a periodic stack of two dielectric layers of low and high refractive index material, with an optical thickness of a quarter wave for the designed wavelength λ_{bragg} . The high number of DBR pairs allows a high reflectivity ($> 99\%$) in a narrow spectral region (called “stop band” region). The active region has an optical thickness of λ so that the structure forms a Fabry-Perot cavity. The reflections from the two DBR’s form a standing wave, whose antinode is located in the center of the spacer layer. With 15 (25) top (bottom) DBR pairs, a quality factor Q about 3200 is expected for this structure. This value would allow an enhancement of the spontaneous emission as well as a good extraction efficiency. The top DBR pair number is smaller than the bottom DBR pair number in order to collect the luminescence from the top. Reflectivity measurement of such structure before the etching of the micropillars is shown on the figure 5.11. At the center of the stop band, the cavity mode appears as a very narrow peak. Outside the stop band, a rather pronounced peak structure appears. These minima in reflectivity can be interpreted as confined modes called “leaky modes” other than the main cavity mode [Savona 98]. These modes act as very efficient channels for emission into the substrate, where the light is

absorbed and consequently lost. They constitute the main limitation of the overall efficiency of microcavity light emitting devices. From an epitaxial viewpoint, full parameter control over the duration of sample preparation is necessary to meet quality requirements. The flux of Al and Ga should be carefully controlled in order to obtain the proper thickness and interface quality to maximize the reflectivity and tune the cavity wavelength to 1300 nm. Al and Ga fluxes were calibrated immediately before growing the structure. As we can see on the figure 5.11, the resonance of the planar cavity is tuned to the long-wavelength side of the QD emission peak (1300 nm at low temperature) particularly at the center of the wafer. In fact, growth of such structure was performed by taking several points into account: First, the cavity wavelength blueshifts of about 10 nm when the temperature decreases from room temperature to 10K. Second, as we will see in the following, cavity wavelength decreases with etching of small ($<2 \mu\text{m}$) diameter mesa. Third, inhomogeneity of fluxes results in a thickness gradient on the substrate. This leads to a cavity wavelength variation of about 15 nm between the center and the edge of the wafer. Considering all these parameters, we choose to grow the structure with a cavity resonance measured at 1335 nm in the center of the wafer. After the growth, the micropillars are processed in the Laboratoire d'Optique

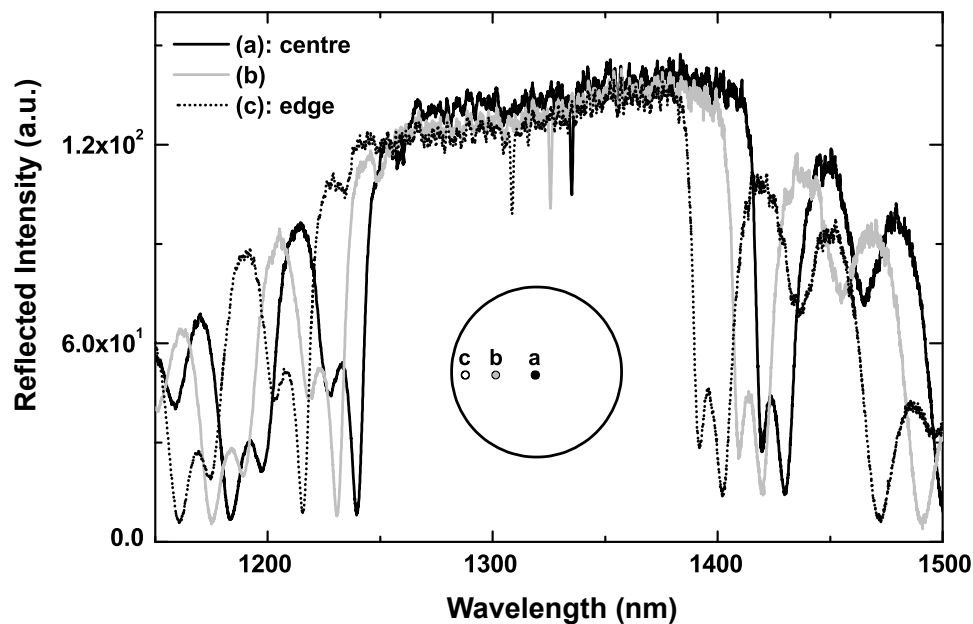


Figure 5.11: Reflectivity spectra of the micropillar structure before pillar processing on different positions a, b, c, on the wafer.

sur Silicium in Grenoble. E-beam lithography followed by dry etching with RIE is used to realize micropillars with diameter size ranging between $5\ \mu\text{m}$ and $0.9\ \mu\text{m}$. Figure 5.12 shows two SEM pictures of micropillars with $2.5\ \mu\text{m}$ and $1.2\ \mu\text{m}$ diameter. Si_3N_4 used as mask for lithography is still present on the top of the pillars.

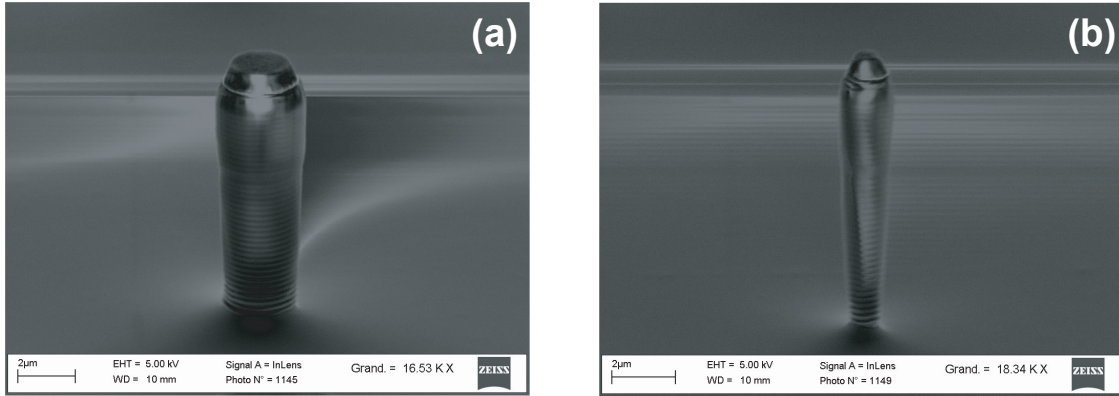


Figure 5.12: SEM pictures of micropillars with (a) $2.5\ \mu\text{m}$ and (b) $1.2\ \mu\text{m}$ diameter.

Photoluminescence measurements

First photoluminescence measurements have been performed on mesa with different diameters. A relatively high excitation power ($50\ \mu\text{W}$) was used to obtain a broad emission spectrum from the QDs and thus determine our cavity modes. Sharp lines of cavity modes are visible on figure 5.13(a). On figure 5.13(a) and (b) we observe that the mode wavelength blueshifts with decreasing pillar diameter and that the energy difference between the modes increases at the same time, which is a signature of optical confinement: the effective refractive index of the mode decreases and the overlap between the mode and the semiconductor core decreases [Gayral 01]. We also observe that the spectral width of the mode increases when the diameter gets smaller. This implies a decrease of the quality factor. This trend is due to the increased efficiency of light scattering on the pillar sidewalls. The highest quality factor (calculated by a Lorentzian fit on the cavity mode) of 3000 has been obtained on $2\ \mu\text{m}$ diameter mesa as presented in figure 5.14(a). By considering the modes in the micropillar as a linear combination of guided modes of a GaAs cylinder [Gérard 96], we can estimate their effective height ($\sim 2\lambda_c/n$) and area ($\sim \pi R^2/4$) with R being the pillar radius. We thus

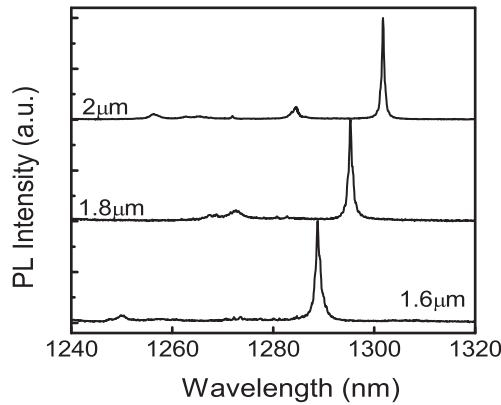


Figure 5.13: Normalized PL spectra of micropillars with different mesa diameters, excitation power: $50 \mu\text{W}$.

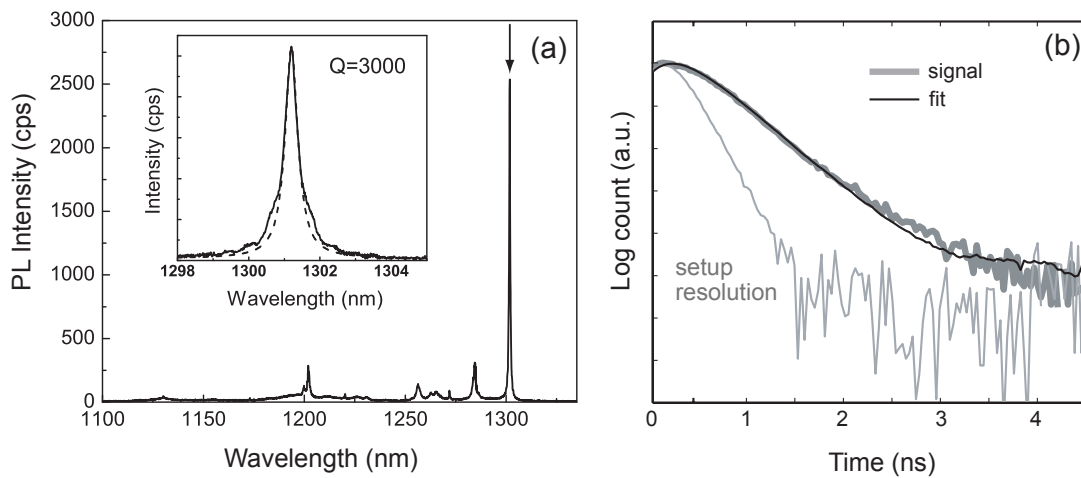


Figure 5.14: (a) PL spectra of a micropillar with diameter of $2 \mu\text{m}$, excitation power: $50 \mu\text{W}$. Inset: High resolution spectrum of the cavity mode ($Q=3000$) (b) PL transient of QDs on resonance with the cavity. Arrows on figure (a) show the corresponding spectral position of the decay measurements. Excitation energy density: $1 \mu\text{J}/\text{cm}^2$.

calculate for the fundamental mode a theoretical Purcell factor of about 20 which is in the order of reported values on similar structure [Gérard 98, Bennett 05c].

Experimental evidence of the Purcell effect in our structures can be obtained through time-resolved experiments. For an important Purcell effect, the emitter will radiate much faster in the cavity than in free space. A shortening of the PL decay is expected when QDs are in resonance with the fundamental mode of the micropillar. Time-resolved measurements have been done on the $2 \mu\text{m}$ diameter mesa on the spectral position of the fundamental mode under an excitation energy density of $1 \mu\text{J}/\text{cm}^2$. Transient is shown in figure 5.14. After

deconvolution of the setup response, the decay time is estimated around 0.42 ns which is much lower than the radiative lifetime (>1 ns) measured on QD ensembles and single QDs. This is consistent with our expectation, however this results should be considered with caution since at this excitation power, the QD emission is broader than the width of the cavity mode. Further investigations will be needed to isolate single QDs in resonance with the cavity mode.

5.3.3 Photonic crystal microcavity

A photonic crystal is a dielectric structure created in 1987 from works of Yablonovitch [Yablonovitch 87] and John [John 87] by analogy with a crystal structure. It consists of a dielectric medium that is patterned into a regular three-dimensional structure with a length scale on the order of the optical wavelength. Light is Bragg-scattered by the periodic structure of the crystal. For a proper crystal design, light cannot propagate in any direction within the crystal. The range of optical frequencies that are excluded from the material is called the photonic bandgap, in analogy to the electronic bandgap in semiconductor materials. As in a semiconductor, a defect in the crystal structure will lead to a localized state within the bandgap. For example, if one of the voids in the photonic crystal is filled in with dielectric material, light will be trapped at that point. Such a defect mode could thus serve as a three-dimensional optical cavity with a small mode volume. Optical properties of photonic crystal are well explained in the Ref. [Sadoka 01].

Design and optical measurements reported in the following have been done by Laurent Balet. As it is very difficult to fabricate a 3D photonic crystal cavity, a 2D photonic crystal with a 1D vertical confinement by total internal reflection in a waveguide has been studied. The structure consists of a single layer of low density QDs grown at the center of a 320 nm-thick GaAs membrane on top of a 1500 nm-thick $\text{Al}_{0.7}\text{Ga}_{0.3}\text{As}$ sacrificial layer. We note that the QD density used in this case ($\sim 2 \cdot 10^9/\text{cm}^2$) is higher than the density usually employed in this work ($\sim 2 \cdot 10^8/\text{cm}^2$) in order to increase the probability of spatial coupling between QDs and the cavity mode. Processing of the structure has been done in the Institute of Photonics and Nanotechnology in Roma [Gerardino]. Two dimensional photonic crystal is realized by e-beam lithography, reactive ion etching (RIE) of a SiO_2 mask, RIE of the GaAs/AlGaAs and wet etching of the AlGaAs sacrificial layer. An optical cavity is created with “L3”-type point defect i.e. three missing holes in a line as shown on the figure 5.15(a). This assures the in-plane confinement of the light. The vertical one is achieved by removing

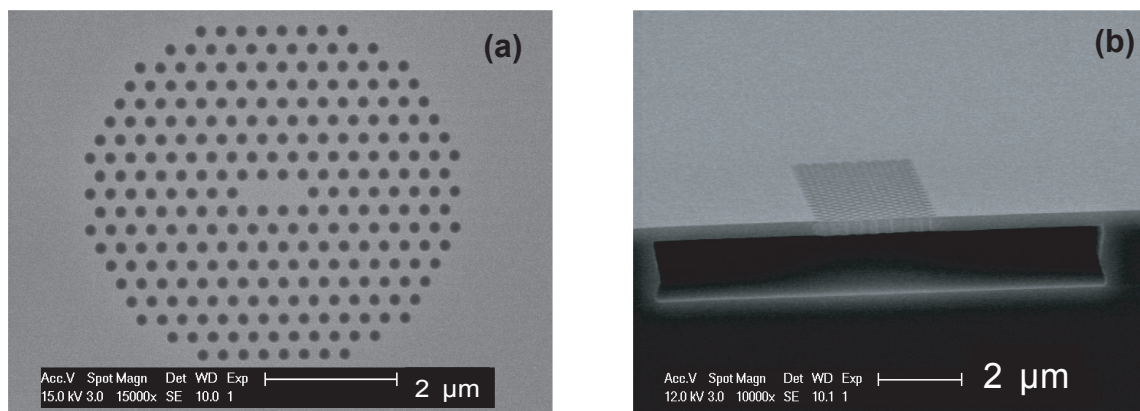


Figure 5.15: SEM picture of (a) photonic crystal microcavity with “L3”-type optical cavity and (b) cross-section of the GaAs membrane obtained after removing of the AlGaAs sacrificial layer.

with wet-etching method, the AlGaAs sacrificial layer creating reflections at the interfaces air/semiconductor. Such GaAs membrane can be seen in cross-section on the figure 5.15(b). Figure 5.16(a) shows a photoluminescence spectra obtained at 10K under a excitation power of 12W. The sharp line observed is attributed to a cavity mode since emission of single QDs is relatively broad at this high pumping level. The quality factor of the resonant mode is estimated at 9440.

In order to observe the effect of the cavity on the emission intensity of the QDs, photoluminescence measurements at different temperatures have been done: in fact, the cavity wavelength is less sensitive to the temperature than the QD emission wavelength, which allows us to clearly separate the emission from the QDs and from the cavity mode. Figure 5.16(b) presents PL spectra done under an excitation power of $12 \mu\text{W}$ at temperatures ranging between 10K and 35K. QD and cavity signal are clearly distinguishable, however we do not observe an obvious enhancement of the QD signal. This implies that the QD is not spatially well coupled to the cavity mode. Further experiments are currently under way on microcavities with lower density QDs.

5.4 Conclusion

We have isolated the luminescence of a single quantum dot emitting at 1300nm, clearly identified the different spectral lines in the emission and studied their evolution as a function

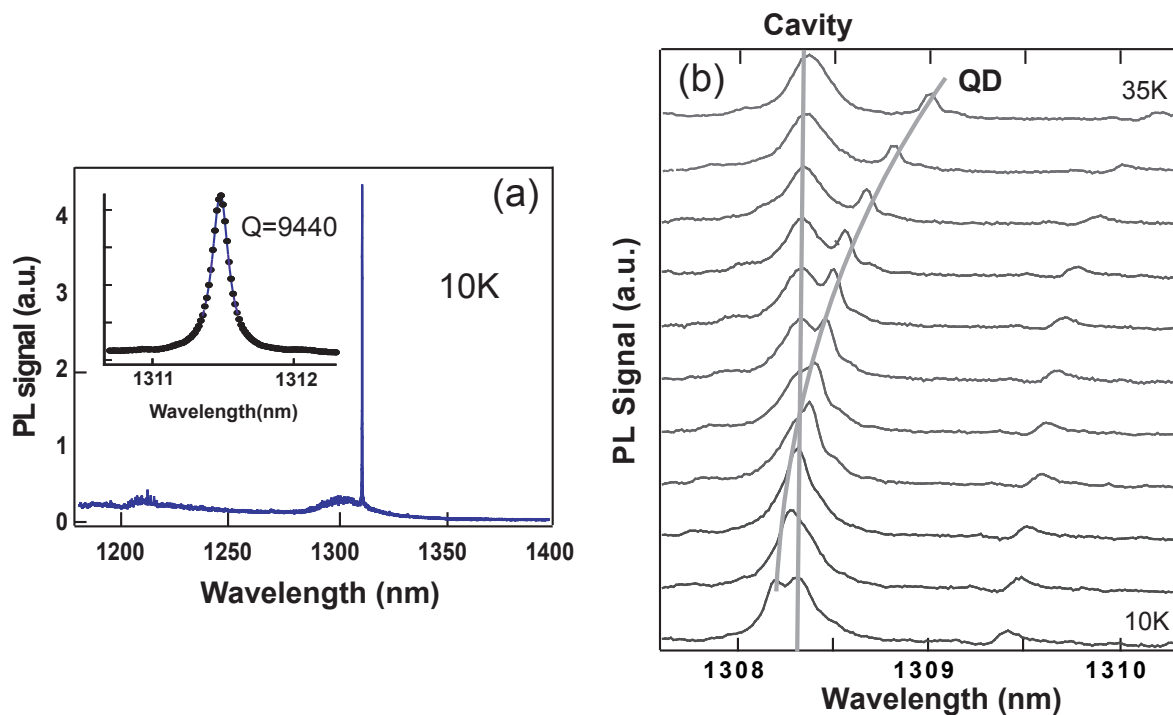


Figure 5.16: (a) PL spectra of a L3 photonic crystal cavity at 10K. Excitation power: $70 \mu\text{W}$ (b) PL spectra performed at temperatures ranging between 10K and 35K, under an excitation power of $12 \mu\text{W}$.

of excitation power and temperature. Antibunching experiments have shown that the low-density QDs constitute a real single-photon source, moreover, resonant excitation would allow the realization of antibunching experiment at even higher temperature by decreasing the background signal. Experiment on QDs inserted in three dimensional microcavity are currently under way, in order to increase the extraction efficiency and thus, the signal-to-noise ratio.

6

Single quantum dots in light emitting diodes

Single-photon emission under electrical pumping is the last requirement to obtain a practical single-photon device. Electrically pumped single-photon sources were first reported using quantum dots formed by etched mesoscopic heterojunctions [Kim 99]. However, low temperatures of the order of 50 mK were required. First electroluminescence (EL) from single quantum dot has been obtained in 2002 by insertion of quantum dots into an intrinsic region of a conventional p-i-n structure [Yuan 02]. This showed how a single InAs/GaAs QD can be incorporated into a conventional semiconductor light emitting diode (LED). In order to excite or to collect luminescence of a single QD, the active device size should be well below $1\ \mu\text{m}$, which represents a challenge for both device design and fabrication. Two approaches are adopted for the fabrication of a single-photon LED:

Post-filtering of QD emission: This method consists for example in using micro-size apertures in an opaque metal contact to select emission from a few QDs located underneath [Yuan 02, Bennett 05a, Ward 04].

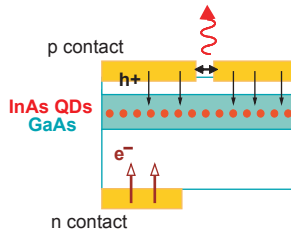
Restriction of the number of excited QDs: This has been realized by several ways depending on the processing techniques [Baier 04, Xu 04]; for example, cross shape devices [Itskevich 00, Schmidt 06] selectively inject current in a small active area, mesa etching reduces the volume of active area and increases the light confinement at the same time, while oxide aperture [Huffaker 98, Fiore 02, Ellis 06] is used to confined electrical injection.

At the beginning of this thesis, only one demonstration of single photon emission under electrically pumping was reported [Yuan 02], and thus, at an emission wavelength at 900 nm. As present, the few demonstrations of single QD LEDs so far are still mainly restricted to the wavelength range lower than $1 \mu\text{m}$. Considering the advantages and limits of these different approaches, we will expose briefly our first results on LEDs with metal aperture, including low-density QDs emitting at 1300 nm in the active region. Then we will propose a method of selective current injection using AlGaAs oxidation. Fabrication and electrical characterization of the devices will be developed, low-temperature EL measurements will be reported. This approach will be extended in the last part to LEDs with strong optical confinement in order to improve the extraction efficiency.

6.1 Comparison of different approaches

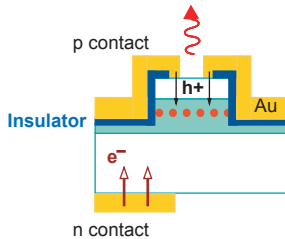
The different methods exposed in the last paragraph present several advantages and limits as follow:

Metal aperture:



This method provides a good filtering of the QD ensemble emission. Processing steps are easy to realize but high-resolution lithography is required to define mesa with sufficiently small diameter. Moreover, the diffraction at the metal aperture limits the extraction efficiency when the signal is coupled into a single mode fiber. Additionally, external quantum efficiency is lowered by the lack of spatial restriction for carrier injection.

Restriction of the active area:

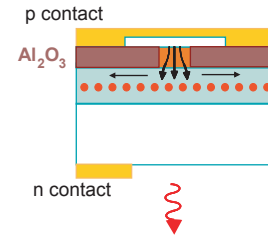


The realization of cross-shape devices to inject current selectively in a single QD, requires complex processing techniques (for example, focused ion beam implementation of doping in GaAs substrate to define a submicron wide bottom contact stripe [Schmidt 06]). A more common technique is to etch a mesa through the active

region: current injection and light are confined but nonradiative recombinations at etched sidewalls strongly reduce the efficiency as the perimeter/area ratio increases. Moreover it requires a high resolution lithography technique.

Restriction of current path by a current blocking layer:

A typical blocking layer is an Aluminium oxide layer. This has the strong advantage to restrict the emitting QD number, by creating a small aperture without appealing high-resolution lithography, and avoiding creation of defect by etching. On the other hand, the current spreading between the blocking layer and the active region can increase the effective active diameter by several micrometers and carrier diffusion in the active region increases the effective radius by the diffusion length, typically, 1-2 μm [Fiore 02].



As a first approach, a top emitting LED using metal aperture was realized. Considering luminescence results, we decided to fabricate a single QD LED structure which relies on nanoscale current injection through an oxide aperture.

6.2 Metal aperture light emitting diodes

6.2.1 First structure: metal aperture

The first grown structure is a classical p-i-n junction as represented on the figure 6.1. It is designed for an emission at 1300 nm at 5K with an extraction efficiency estimated at 0.62% at 1300 nm by using a simulation software based on the dipole source-term method [Benisty 98]. Before the metal evaporation on both side of the sample, electron beam lithography, performed at the Institute of Photonics and Nanotechnology, CNR, in Roma, was used to define large p-contacts pads of $\sim 0.1 \text{ mm}^2$ area with metal aperture in the center. Diameters of the apertures range between 10 and 1 μm .

6.2.2 Measurements

The current-voltage characteristic shows an exponential increase of the current with a threshold voltage around 2V. Sample was then mounted in the cryostat for EL measurement at

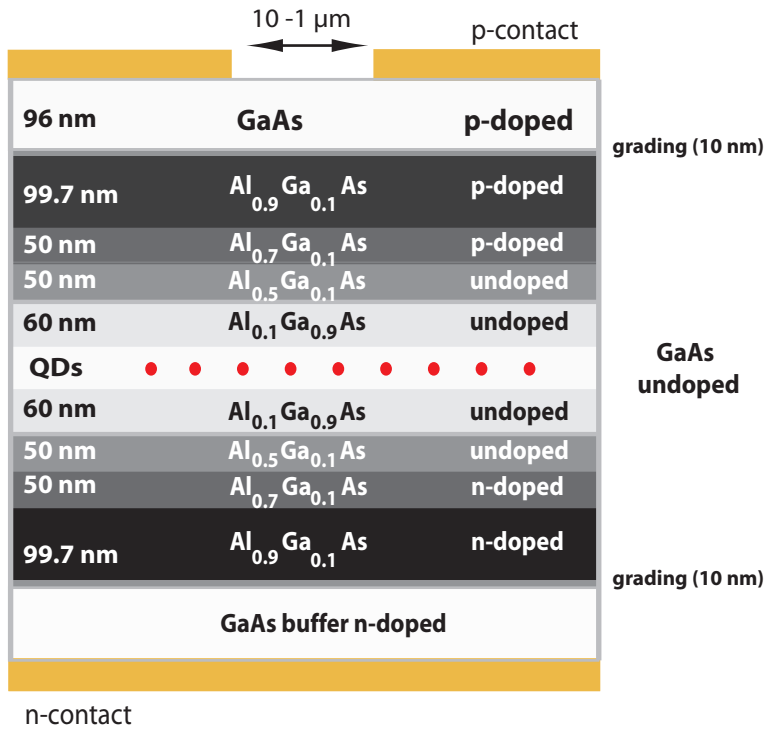


Figure 6.1: Sketch of the LED structure with metal aperture.

low temperature. Figure 6.2(a) and (b) summarizes the results for $10\ \mu\text{m}$ and $2\ \mu\text{m}$ diameter mesa aperture, respectively at different current intensities. On figure 6.2(a) spectra are measured at 22K for a current between 13.2mA and 20mA. Ground state, first excited state and WL emission appear clearly. At 20mA ground state is clearly saturated. Inset shows 1 spectra measured under electrical excitation and 1 spectra under optical excitation by using a laser diode at 650nm. This last spectra shows already sharp lines which are not visible on the EL spectra. On figure 6.2(b), for comparative injection current, EL intensity is lower due to the small aperture diameter. On the inset we observe that WL totally disappears at 16mA. For the same current ES emission is very weak. This would further confirms our optical observations detailed in chapter 4 which shows that carrier capture from QL into the QDs is efficient. At 15mA no signal is detected. This evidences a problem of injection over a large area due to current spreading and a problem of optical losses by light generated in the lateral wave guide.

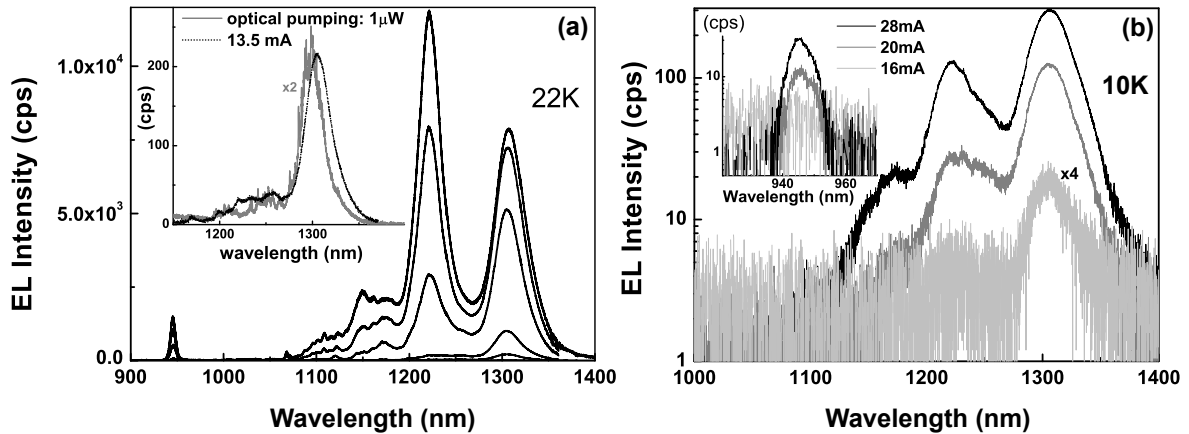


Figure 6.2: (a) Electroluminescence spectra from $10 \mu\text{m}$ aperture diameter, with excitation current between 20 mA and 13.2 mA. Inset: Electroluminescence spectra at 13.5 mA with photoluminescence spectra at $1 \mu\text{W}$ excitation power. (b) Electroluminescence spectra from $2 \mu\text{m}$ aperture diameter. Inset: Wetting layer emission spectra.

6.2.3 Second structure: metal aperture and mesa etching

Another structure similar to the previous one is grown with, in addition, 14.5 pairs of bottom n-doped distributed $\text{Al}_{0.9}\text{Ga}_{0.1}\text{As}/\text{GaAs}$ Bragg reflector to increase extraction efficiency. (Extraction efficiency of such structure was estimated at 8.1%).

A shallow mesa ($>20 \mu\text{m}$ diameter) is etched through the active region to suppress QD emission outside the active area and a metal aperture is performed using electron beam lithography with an aperture diameter ranging between 10 and $1 \mu\text{m}$. An isolating layer of Si_3N_4 deposited by PECVD separates the etched mesa from the metallic layer. Final device is sketched on the figure 6.3(b).

As shown on figure 6.4(a), EL measurements do not allow to observe distinguishable sharp lines. We observe important light leaks on the mesa side (figure 6.4(b)) in spite of successive metal depositions, which contribute to an important signal background. This leak corresponds to scattering of wave-guided light at the mesa sidewalls. A possible improvement could be to use wet etching to fabricate mesa with oblique sidewalls. This would reduce the scattering and facilitate the metal adherence.

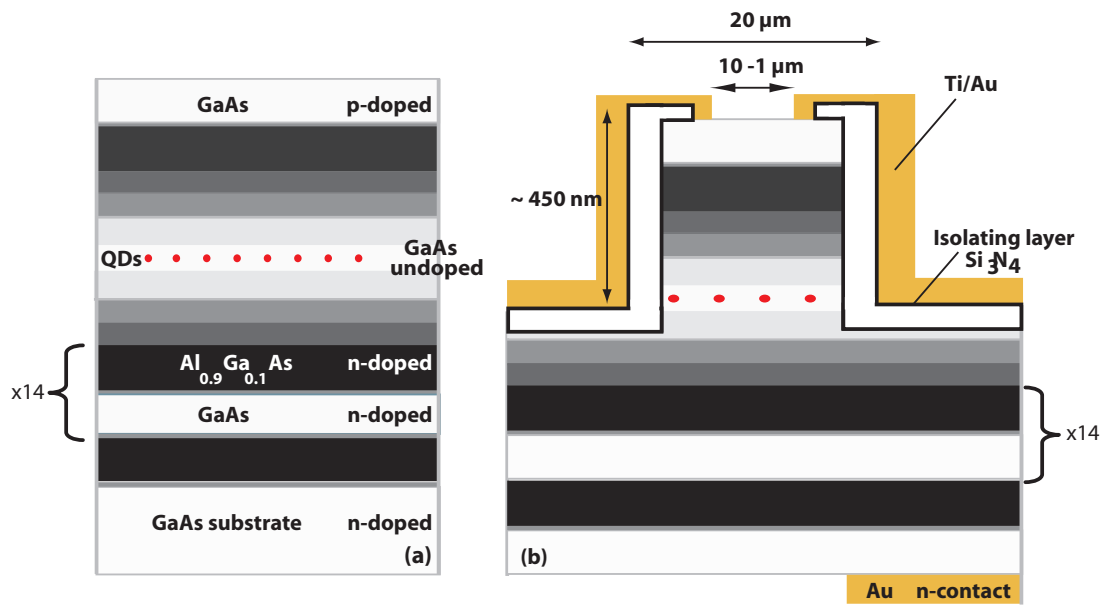


Figure 6.3: Sketches of (a) the epitaxial structure, (b) processed device, of LED structure with metal aperture and mesa etching through the active region.

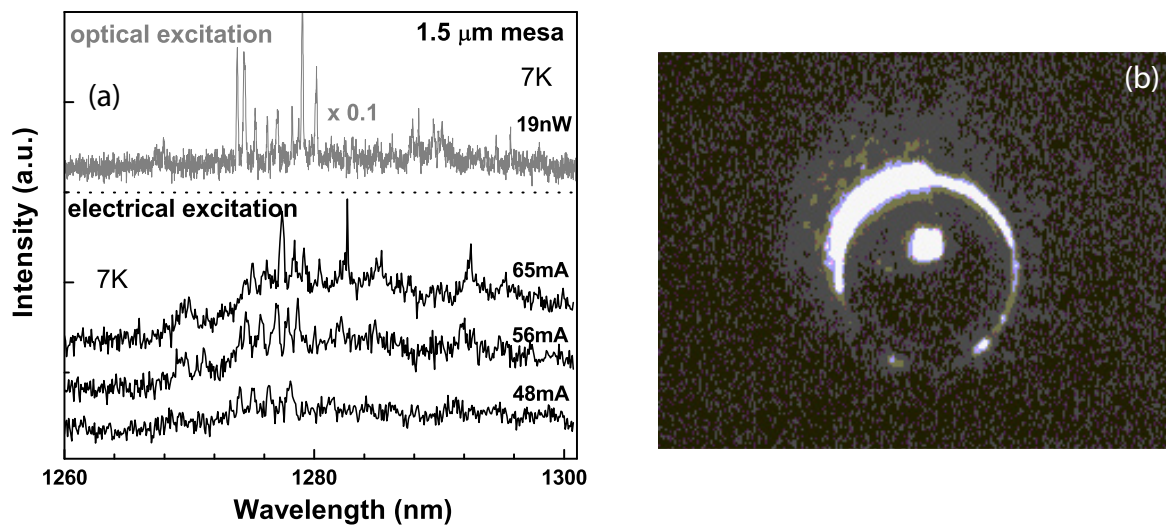


Figure 6.4: (a) Electroluminescence and photoluminescence spectra on $1.5 \mu\text{m}$ metal aperture. (b) Picture of $10 \mu\text{m}$ diameter mesa with metal aperture in the center under electrical excitation. Light leaks are clearly seen on the edge of the mesa.

6.2.4 Conclusion

These first investigations points out the major problem of metal aperture due by the absence of current confinement: A lot of light is generated in the wave-guide which results in a scattering at the aperture and mesa sidewalls. It appears then suitable to selectively inject current in a small area. We then turned to another approach which allows a selective current injection using oxide aperture. The LED design which will be employed in the following has been previously proposed by our group[Fiore 02] and tested on high-density QDs.

6.3 Current-aperture LEDs

6.3.1 Structure

LDQDs have been inserted in the middle of a GaAs p-i-n diode grown by MBE onto an n-doped GaAs (001) wafer. The QD layer is surrounded by a bottom n-doped distributed $\text{Al}_{0.9}\text{Ga}_{0.1}\text{As}/\text{GaAs}$ Bragg reflector (3.5 pairs) and a top hole injector composed of a 32 nm undoped AlGaAs layer (composition linearly graded from 0% to 85%, from bottom to top). Above this hole injector, an $\text{Al}_{0.85}\text{Ga}_{0.15}\text{As}$ current aperture (to be oxidized) and a heavily-doped cap GaAs contact complete the epitaxial structure. Except for the bottom 20nm in the $\text{Al}_{0.85}\text{Ga}_{0.15}\text{As}$, which are undoped, the rest of those two top layers are p-doped($p=2 \cdot 10^{18}\text{cm}^{-3}$). Optimization of the doping profile will be discussed later.

6.3.2 Processing steps

Device processing (see figure 6.5 starts with the definition of shallow mesa with diameters ranging between $1 \mu\text{m}$ and $10 \mu\text{m}$ by a standard optical lithography and dry etching. This etch step exposes the sidewalls of the current-aperture $\text{Al}_{0.85}\text{Ga}_{0.15}\text{As}$ layer located on top of the QDs. This layer is then oxidized following the procedure described in chapter 2. The oxidation starts at the exposed surface and then penetrates laterally under the GaAs capped layer, defining a remaining unoxidized current-aperture region, whose diameter can be controlled by oxidation time with 100 nm accuracy. The aperture diameter scales with the initial mesa size so that devices with different current apertures are created in a single step. After an additional Si_3N_4 isolation-step above the Al_2O_3 layer and around the mesas, a broad area Ti/Au layer is evaporated on top of the devices. Ti/Au was chosen instead of pure Au for a better adherence of the metal contact. This final step is performed without any

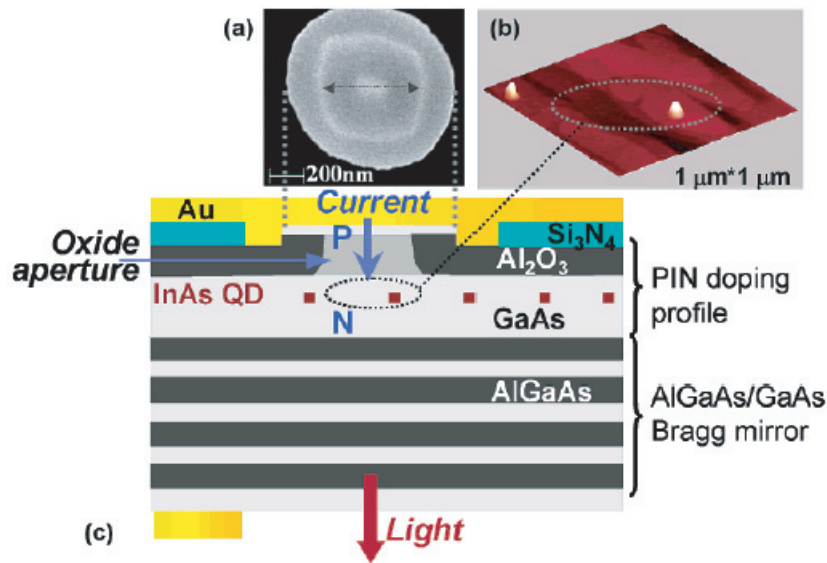


Figure 6.5: (a) SEM top view of a LED device before metal evaporation: the oxidation of a 200nm-wide area around the mesa leaves an unoxidized aperture diameter of around 600nm. (b) A typical atomic force microscopy image of the uncapped InAs/ GaAs quantum dots displaying a surface density as low as two dots in a $1 \times 1 \mu\text{m}^2$ surface. (c) A schematic cross section of the quantum dot bottom-emitting LED. [Monat 06]

critical alignment due to the Al_2O_3 oxide layer, which forces the current to flow through the nonoxidized area of the mesas. the weak microcavity defined by the top Au mirror and the bottom Bragg mirror (quality factor =20) is designed to enhance the extraction of 1300 nm- radiation from the bottom device. Extraction efficiency has been estimated theoretically at 4.5%. The current aperture diameters of the devices have been measured by SEM before metal evaporation and range from $0.6 \pm 0.005 \mu\text{m}$ to $10 \pm 0.005 \mu\text{m}$. Final structure is presented on the figure 6.5.

6.3.3 Limitation: current spreading and carrier diffusion

A study performed in our group on a similar structure with an active region consisting on high density QDs, points out the distinct effects of current spreading and carrier diffusion [Fiore 04]. As shown on the figure 6.6, carrier diffusion, in the contrary of current spreading, occurs in the active region. Current spreading can be changed by a proper design

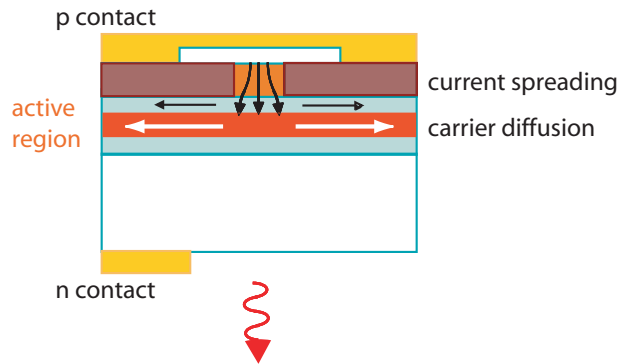


Figure 6.6: Sketch of current spreading and carrier diffusion mechanisms

of doping profile while carrier diffusion depends on the nature of the active region. Both mechanism can be distinguished by analysis of current-voltage(I-V) and light-current(L-I) characteristics.

Current spreading is determined by the ratio of the lateral and vertical impedance: particularly at low bias, when the diode impedance is large, current can find a lower impedance path by flowing laterally (parallel to the layers) and spreading on a much larger area. As the bias is reduced, and thus the diode impedance increases, lateral current flow becomes more significant and the effective device area increases, leading to a higher current. In contrast carrier diffusion does not depend on bias level and produces a bias-independent increase in the active diameter.

To suppress current spreading, the layers between the oxide aperture and the active layer were not doped in order to increase the lateral resistance. This doping profile was compared to another structure in order to estimate the importance of the current spreading in our LED structure. In this second structure, the 32 nm-thick undoped graded injector and the 20 nm-thick undoped $\text{Al}_{0.85}\text{Ga}_{0.15}\text{As}$ layer were replaced by a 20 nm-thick p-doped $\text{Al}_{0.3}\text{Ga}_{0.7}\text{As}$ layer, which acts as a current spreading layer. Figure 6.7 shows sketch of the both structures ((a) and (b)) and the band diagram around the active region under an applied bias of 1V, calculated by the Simwindows simulation package [Winston], assuming a 5 nm-thick InAs QW as the active layer. With a composition gradient of the AlGaAs layer, the potential barrier in the valence band between the p-doped layer and the active region can be avoided which facilitates hole injection in the QDs. I-V curves were measured and current density was derived using the measured current aperture area. Its dependence versus voltage is presented on the figure 6.8.

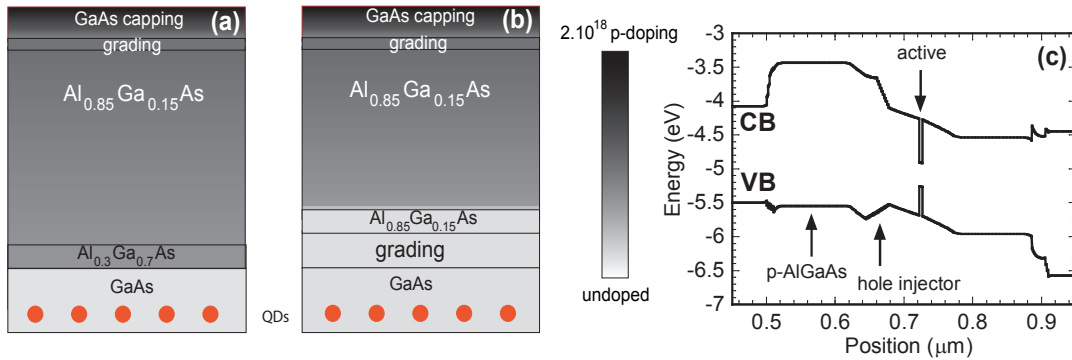


Figure 6.7: Top-part structures of QD LED with (a) doped current spreading layer and (b) optimized injection region. (c) Band diagram (CB: conduction band; VB: valence band) around the active region of the QD under an applied bias of 1 V, calculated by Simwindows [Winston], assuming a 5 nm-thick InAs QW as the active layer. The 32 nm-thick AlGaAs with Al composition linearly graded from 0% to 85% acts as a hole injector by accelerating holes toward the active layer.

The LEDs with optimized graded undoped injector show exponential diode characteristics, except at high bias, where the current becomes limited by the series and contact resistance. The scaling of current with aperture area is very good: the current density versus voltage curves superpose over three orders of magnitude of current in the low bias range. In contrast, LED with current spreading layer has strongly nonexponential I-V characteristic and does not show proper scaling with current aperture area. The absence of scaling is related to the fact that the effective device area is larger than the current aperture. The nonexponential behavior of I-V characteristics is a strong evidence of current spreading. As the bias is reduced, and thus the diode impedance increases, lateral current flow becomes more significant and the effective device area increases, leading to a higher current than in the undoped injector structure. The comparison of the doped versus undoped injector structure shows that the p-injector plays a major role in the current-voltage characteristics of LEDs and lasers.

6.3.4 Diffusion coefficient and diffusion length

The diffusion length sets the ultimate limit on the active device diameter. The diffusion process depends strongly on the dimensionality of the active region: While 3D carrier diffusion is possible in a bulk unconfined active region, diffusion is restricted in a plane for a 2D

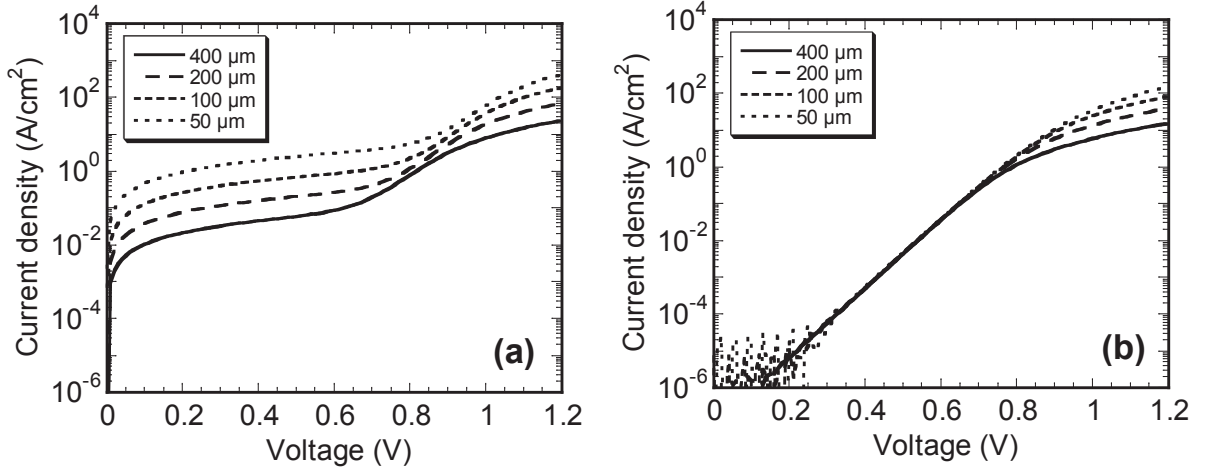


Figure 6.8: Measured J-V characteristics of (a) QD LEDs with a doped current spreading layer, and (b) QD LEDs with an optimized injection region. The current density is obtained by dividing the current by the oxide aperture area.[Fiore 04]

quantum well, to a single direction for a quantum wire and finally carriers are completely localized in an ideal QD. A comparative investigation of diffusion, performed in our group, in semiconductor heterostructures having different dimensionality, shows a significant in-plane diffusion in high quality QWs and a suppressed carrier diffusion in QDs and disordered QWs [Fiore 04].

To design the LED structure it is important to understand the nature of the diffusion process, ie. if it involves a single type of carriers (unipolar diffusion) or both (ambipolar diffusion). In case of a symmetric injection of electrons and holes, difference of mobility between electrons and holes, leads to an imbalance of electrons and hole concentrations which produces an electric field that contributes to charge transport through a drift term. The transport including diffusion and drift can be described as a purely diffusive process with an effective ambipolar diffusion coefficient given, for a nondegenerate semiconductor, by [Seeger 85]:

$$D_a = 2 \frac{D_n D_p}{D_n + D_p} \quad (6.1)$$

Where D_n and D_p are the electron and hole diffusion coefficient, respectively. However, in case of a localized injection of holes from an aperture or a mesa, situation is different since carrier injection is asymmetric [Joyce 82]. For our case, injection of holes from the p side is localized and electron injection from the n side is uniform. A similar derivation as in the

case of ambipolar diffusion leads to describing both transport and diffusion with an effective diffusion coefficient [Joyce 82]:

$$D_e \approx 2D_p \quad (6.2)$$

In case of confined electrons the diffusion coefficient becomes: $D_e \approx 2D_n$. As $D_n \ll D_e$, it is preferable to localize the injection of holes to minimize the diffusion.

6.3.5 Current-voltage measurements

We now describe the characteristics of the current-aperture LEDs with low-density QDs. The room temperature I-V curves of the devices with varying diameters are displayed in figure 6.9(a), showing exponential diodes characteristics, limited at high bias by the series resistance of the p-doped mesa. For each devices, the diameter of the current aperture was measured by SEM during the process and used to calculate the current density. We observe there is no scaling with the current aperture area: smaller devices have an apparently higher current density. This is due to the fact that active area is increased by the diffusion of carriers along the active layer. We then deduce the diffusion length from the scaling of I-V characteristics with device area, the active radius is then be given by the radius of the unoxidized region increased by a diffusion length L_d . The current for device n is then given by:

$$I_n(V) = J_0(V)S_n = J_0(V)\pi(r_{aper,n} + L_d)^2 \quad (6.3)$$

Where S_n is the effective active area, $r_{aper,n}$ is the aperture radius, and J_0 is the current density in a planar device (where L_d is negligible compared to the aperture radius). As a starting point, we take J_0 as the current density calculated from the largest device using the current aperture area. For each device, we calculated $L_d=L_d(V)$ from equation 6.3. L_d value is be independent of the voltage in a certain range. The procedure is then iterated by using this value in the calculation of J_0 , until a self-consistent value of L_d is found. Figure 6.9(b) shows the scaling of $J(V)$ characteristic obtained by assuming $L_d = 1.2 \mu\text{m}$, indicating an effective injection area larger than the current aperture. This is significant as compared to the negligible ($<100 \text{ nm}$) diffusion length calculated for similar LEDs with high density QD in the active region [Fiore 02]. The possibility of fitting the J-V curves over almost 4 orders of magnitude of current (between 0.4 and 1.1V) and more than 2 orders of magnitude of device area with a single L_d parameter allows us to conclude that the involved mechanism depends on the active material and not on the device size and the applied voltage. To explain the increased effective area, we express the measured diffusion

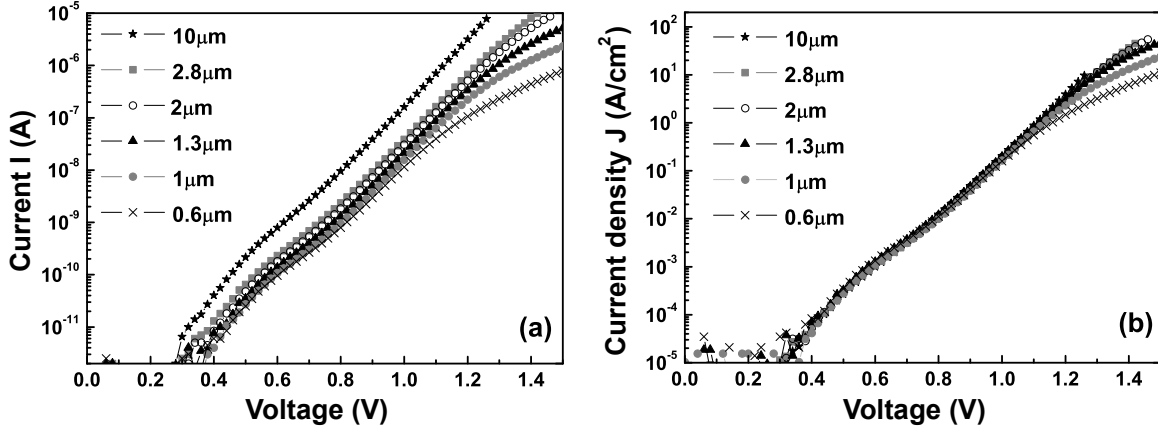


Figure 6.9: ((a) Current vs voltage (I-V) curves at room temperature for LED devices with current-aperture diameters ranging from 600 nm to 10 μm . (b) Room-temperature current density vs voltage (JV) curves deduced from the I-V curves by taking into account the current-aperture radius measured by SEM increased by a constant L_d of 1.2 μm . [Monat 06]

length with the diffusion coefficient D_e seen in last paragraph. Since $I - V$ curves shows an exponential behavior, current spreading is negligible, we thus attribute the increased effective area to carrier diffusion in the wetting layer (WL) prior to capture in the QDs. In fact, the diffusion length in the WL, $L_{diff} \approx \sqrt{D_e \tau_c}$ (D_e being an effective diffusion coefficient and τ_c the capture time) is expected to be more significant in low-density QDs because capture is likely to be slower.

6.3.6 Light-current measurements

Light current measurements at room temperature (RT) were taken using a calibrated Ge detector with an active area of 1 cm² positioned close to the sample backside, in order to collect most of the optical power emitted by the LEDs. Lock-in techniques are used to accurately measure the low-power levels produced by these small devices. Power versus current characteristics measured on the QD are shown on the figure 6.10 The external quantum efficiency η_{QE} , calculated as $\eta_{QE} = (e/h\nu) \cdot (P/I)$ is plotted on the figure 6.10(b) as a function of the effective current density (current divided by the effective active area assuming a diffusion length of 1.2 μm). The external quantum efficiency ($\sim 10^{-4}$) is independent of mesa diameter excepted for the largest device. For the largest device, efficiency is lower since this device operates at a lower effective current density in this current range, with a corresponding

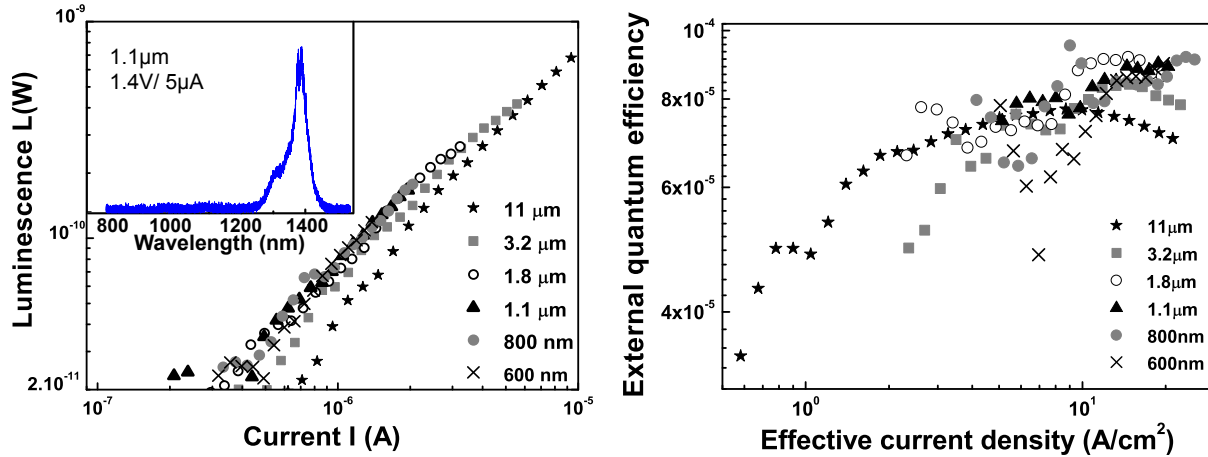


Figure 6.10: (a) Luminescence vs current (L - I) characteristics at room temperature for LED devices with current-aperture diameters ranging from 600 nm to 11 μm . The inset shows a typical spectrum, here related to a 1.1 μm current-aperture device under a $5 \mu\text{A}$ current injection. (b) external quantum efficiency vs effective current density. Current density is calculated assuming a diffusion length $L_d = 2.7 \mu\text{m}$

lower radiative efficiency. We observe a first increase of the efficiency with current density due to the population of QD states and an increase of the radiative recombinations, then efficiency saturates and decreases for a current density higher than $9 \text{ A}\cdot\text{cm}^{-2}$. This is due to a fulfill of QD electronic levels and a proportional increase of non-radiative recombination processes. The fact that efficiency is not degraded for the smallest devices implies that the oxide aperture does not introduce any defects in the active region, which would systematically degrade the performance as the area is reduced. The RT external quantum efficiency is limited by the mismatch in the cavity resonance (the device is designed for optimized extraction at 1300 nm at low temperature) and by the RT radiative efficiency in these low density QDs.

A typical spectrum, plotted as an inset of figure 6.10(a), for a 1.1 μm wide LED under a relatively high current injection of $5 \mu\text{A}$ ($130 \text{ A}/\text{cm}^2$), shows a predominant emission from the QD ground state at 1380 nm and no emission from the WL. This confirms that most of the current is funnelled into the QDs, despite their low surface density.

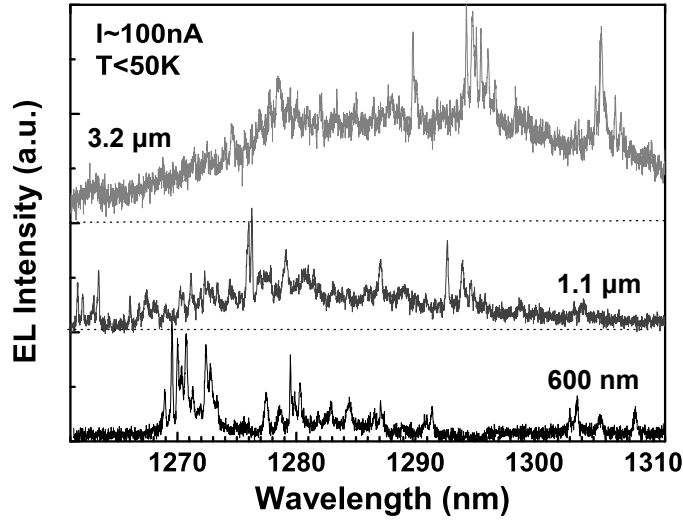


Figure 6.11: Low-temperature electroluminescence spectra for three devices with different oxide apertures, respectively, of 600 nm (I) 200 nA), 1.1 μm (I) 200 nA), and 3.2 μm (I) 30 nA) from bottom to top. Different offsets, which are indicated by a dotted line, have been added to the curves for clarity.

6.3.7 Electroluminescence measurements at low temperature

Devices are wire-bonded before to be introduced in the cryostat. The wire-bonding was a problematic step of the processing: due to the small area of the metallic contact pads, adherence of the Au-wires was difficult and pads were often torn out. This led us to deposit an Si_3N_4 layer between AlGaAs oxidized layer and metal contact. Indeed, metal adherence on the AlGaAs oxidized layer was not strong enough.

After bonding the devices, EL has been measured in the low-temperature microphotoluminescence setup, presented in chapter 2. The EL signal is collected from the bottom part of the device into the microscope objective. Low-temperature ($\sim 40\text{K}$) EL spectra are shown in figure 6.11 for different device sizes. For comparable injected currents (between 30 and 200 nA), the number of observed lines varies strongly with the size of the device. Despite a lower current density, the larger device (3.2 μm oxide aperture) displays densely packed peaks which cannot be resolved properly, whereas smaller devices (1.1 μm and 600 nm oxide aperture) provide EL spectra with clearly distinct features.

Figure 6.12 displays EL spectra, which have been measured on the smallest device and for different currents. At low current, the spectrum is dominated by a single line (at 1277.3 nm)

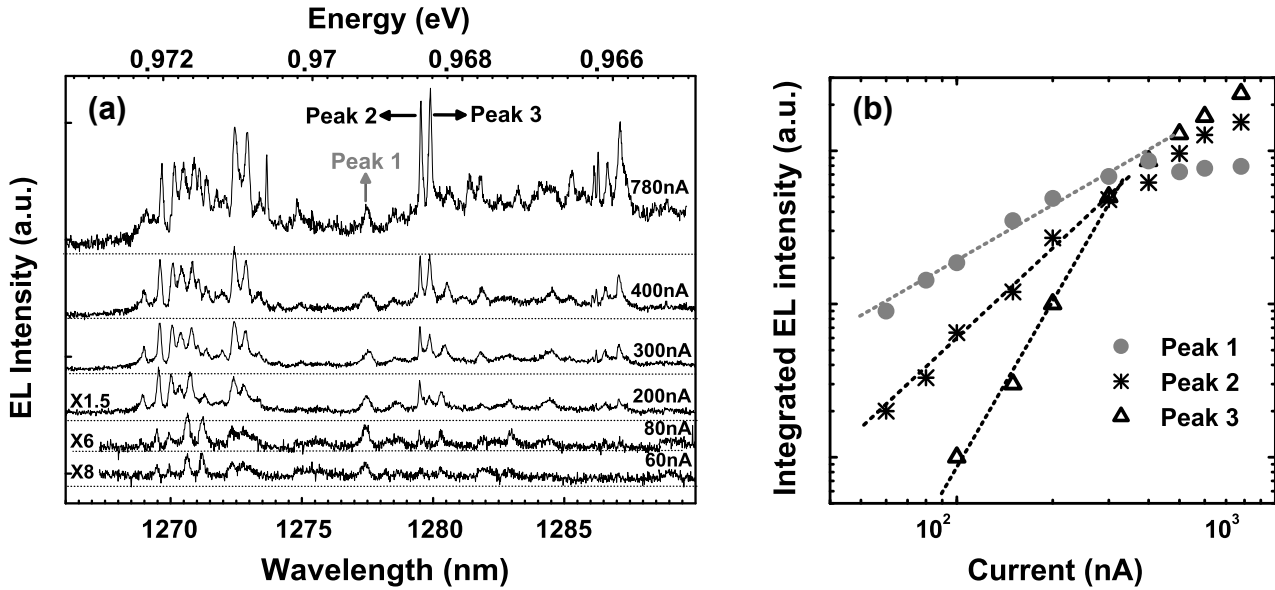


Figure 6.12: (a) Low-temperature electroluminescence (EL) spectra of the 600 nm current-aperture device for increasing current injection. Different offsets, which are indicated by a dotted line, have been added to the curves for clarity. (b) Integrated intensity of three different lines as a function of the injected current. [Monat 06]

associated to the recombination of a single exciton in one QD. An increase of the current results in a growing number of narrow lines, accompanied by the complex dynamics of their relative intensities, which is characteristic of the emission from single QDs. Carriers populate the QD states gradually when current injection increases, giving rise to spectra that display more numerous lines. In Figure 6.12(b), the integrated intensities of three peaks are plotted as a function of the injected current. The intensity, I_1 , of peak 1 at 1277.3 nm (full width at half-maximum, FWHM $\sim 230 \mu\text{meV}$) exhibits a roughly linear dependence ($I_1 \propto I^{1.2}$) on the current, until it saturates around 300 nA. Such a behavior enables us to assign this peak to the exciton state. We note that the amount of current required to saturate the QD exciton state is very low compared to other approaches ([Xu 04, Yuan 02, Bennett 05a]), which shows higher injection efficiencies in our devices. The intensity, I_2 , of peak 2 at 1279.9 nm (FWHM $\sim 75 \mu\text{eV}$) shows a nearly quadratic dependence on I ($I_2 \propto I^{1.95}$), suggesting emission from a biexciton state. The other peaks (such as the peak 3 in Figure 6.12(a)), which appear at higher current, may be attributed to multiexcitonic states (possibly charged) on the basis of their nonlinear dependence on the current. The larger spectral widths (75-

200 μeV), as compared to PL spectra on the same QDs, shown in the chapter 5 may be due to the higher temperature inside the active region of the LED, which should be decreased by optimizing the mounting of the bottom-emitting devices and reducing the contact resistance.

6.3.8 Conclusion

These results show the possibility of selectively injecting current into one or few QDs by the use of oxide aperture. Scattering due to current spreading, which was the principal problem of metal-aperture LEDs, is suppressed in this approach. However diffusion length in the active region is significant regarding the smallest mesa diameter. Considering the small variation of quantum efficiency at different mesa diameters, we conclude that oxide aperture does not enhance nonradiative recombinations. To further improve the efficiency of the device, this LED configuration could be combined with a wavelength-scale high-quality factor microcavity, using the oxidized current aperture to also provide a lateral optical confinement. The next section develops our preliminary results on such 3D-confined microcavity LED.

6.4 Microcavity light emitting diode

As mentioned in the precedent chapter, the extraction efficiency of the QDs can be improved by inserting them in a 3D-confined microcavity LED, through a modification of the spontaneous emission rate by coupling with the cavity mode (Purcell effect). Oxidized aperture technique was used together with DBRs to confine at the same time the carrier injection and the optical mode in a submicrometer volume. We present in this section our first results obtained with high density QDs in the active region.

6.4.1 Structure

The structure has been processed from a planar microcavity grown on (001) oriented n-doped GaAs substrate. The active region consists of a single array of self-assembled QDs formed from 3 monolayers of InAs (InAs growth rate : 0.16 ML/s) and capped with a 5 nm strain-reducing $\text{In}_{15}\text{Ga}_{85}\text{As}$ layer to extend the emission into the near infrared. The density is estimated to be $3 \cdot 10^{10}$ dots/ cm^2 from atomic force microscopy on similar uncapped samples. The QDs are embedded in undoped GaAs. The injection design is the same as for the current-aperture LED: lateral current and optical confinement is provided

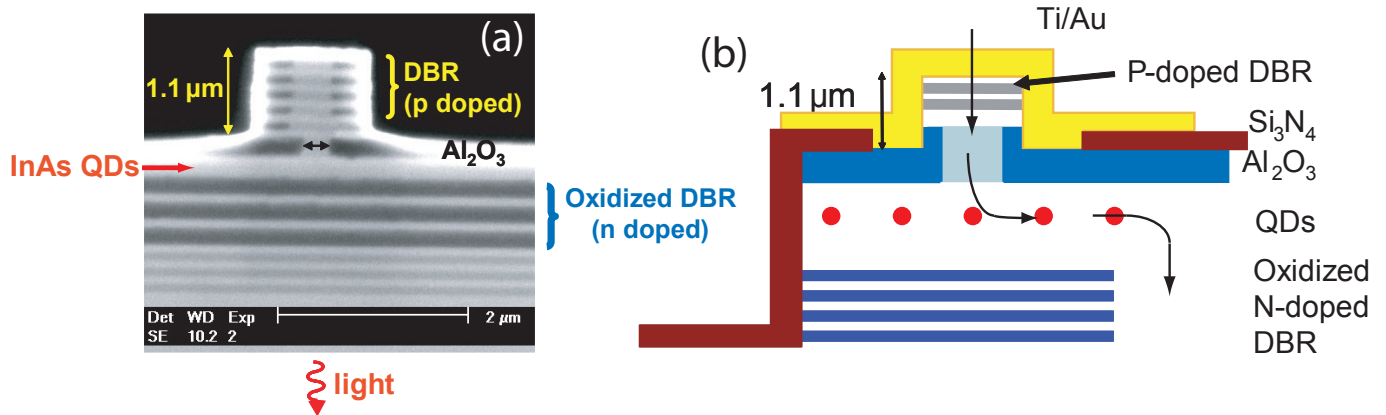


Figure 6.13: (a) SEM cross-sectional image of an aperture of 360 nm (b) Sketch of the processed structure. Black arrows show the current path around the oxidized bottom DBRs.

by an $\text{Al}_{0.85}\text{Ga}_{0.15}\text{As}$ layer, deposited on the top (p-side) of the GaAs layer. The optical cavity is obtained by embedding the active region between a top mirror composed of 5 $\text{Al}_{0.75}\text{Ga}_{0.25}\text{As}/\text{GaAs}$ quarter-wave pairs plus a top Au layer, and a bottom (output) mirror composed of three pairs of oxidized AlAs/GaAs and three pairs of $\text{Al}_{0.9}\text{Ga}_{0.1}\text{As}/\text{GaAs}$. Use of oxidized AlAs/GaAs DBR allows to reduce number of DBR pairs due to the lowest refractive index of oxidized AlAs and at the same time, to enhance the vertical confinement of the optical mode. The target Q (from a one-dimensional simulation neglecting lateral loss) is estimated at 1000.

Using optical lithography and reactive ion etching we fabricated cylindrical mesa structures with diameters ranging from 10.5 down to 1.2 μm . The etching was stopped in the $\text{Al}_{0.85}\text{Ga}_{0.15}\text{As}$ aperture layer, which was then oxidized, at 400°C for 90 min in an H_2O atmosphere. In the same oxidation step the AlAs layers were laterally oxidized from trenches etched at 20 μm distance from the mesa. The etched surface was electrically insulated with a Si_3N_4 layer deposited by plasma-enhanced chemical-vapor deposition. Au pads were deposited on the mesas to form the p-contact and a layer of Au on the substrate was used as n-contact. In order to determine the aperture area, a first estimation of the lateral oxidized distance was obtained on etched stripes from cross-sectional scanning electron microscope (SEM) images, as shown in figure 6.13(a). Sketch of the processed structure presented on the figure 6.13(b) shows the current path.

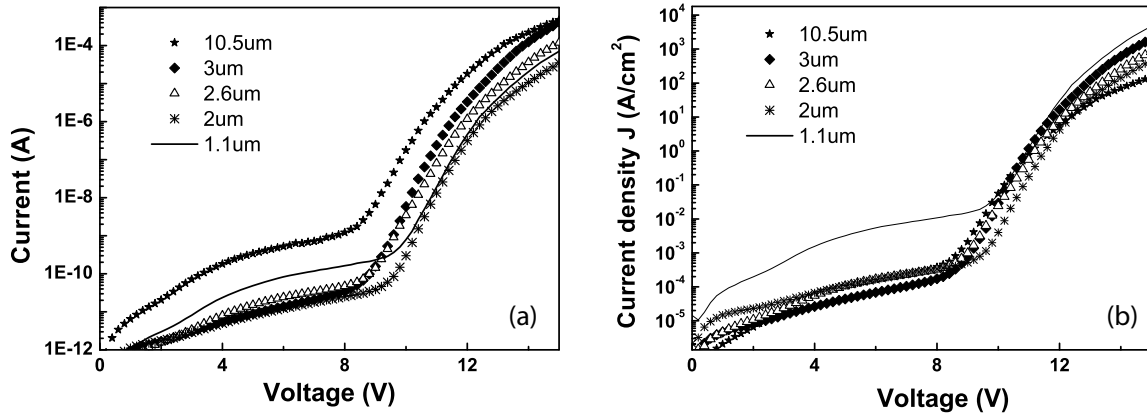


Figure 6.14: (a) Current versus voltage characteristics for different mesa diameter (b) Current density versus voltage deduced from the I-V curves with an oxidation length = 500 nm.

6.4.2 Current-voltage characteristics

Oxide aperture measured by SEM present a strong dispersion that could be attributed to an inhomogeneous depth etching of the sample surface. The aperture diameter in the mesa was further verified by measuring the scaling of the current-voltage characteristic for different nominal device diameters. As shown on figure 6.14(a), a high turn-on voltage is observed and is attributed to potential barriers in the DBRs due to unoptimized composition and doping profile. We suspected that resistance could come from low doping level of p-doped DBR but SIMS measurements presented a high doping level ($7 \cdot 10^{19}$ atoms/cc maximum) with also a high amount of Oxygen (up to $\cdot 10^{20}$ atoms/cc maximum) which could have an influence on the resistivity of the DBRs. Curves are fitted with a single oxidized length parameter (figure 6.14(b)), scaling is correct for all curves except for the smallest mesa, which shows that oxidation length is higher in this case.

6.4.3 Light-current characterisation

Figure 6.15 reports light versus current characteristics at room temperature for a range of devices with different oxide apertures, showing that light is extracted from devices as small as 400 nm in diameter. The measured efficiency is $3.1 \cdot 10^{-4}$ for the largest devices ($9.5 \mu\text{m}$) and decreases to $1.4 \cdot 10^{-4}$ for the 400 nm LEDs. The low efficiency is mostly due to the mismatch between the cavity linewidth and the source spectral width: the QD emission is limited by the inhomogeneous broadening. The QD LEDs are designed to be efficient

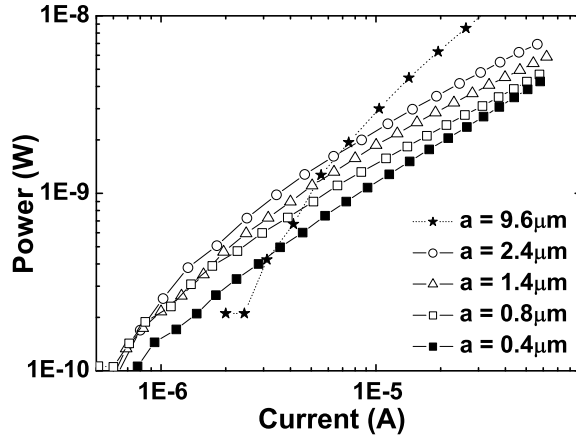


Figure 6.15: Light vs current characteristics (293K) for devices with different aperture diameter a . [Zinoni 04]

devices only for the one or few QDs that are resonant with the cavity mode: the ultimate goal is to demonstrate enhancement of spontaneous emission from a single emitter which requires high quality factors and small mode volumes.

6.4.4 Spectral characterization

The CW electroluminescence spectra at 293K are presented in logarithmic scale in figure 6.16 for devices with decreasing oxide apertures. The devices were individually contacted on the Au pads and the luminescence was collected with a $100 \mu\text{m}$ core optical fiber close to the substrate side, and dispersed into the spectrometer. The individual measurements are characterized by several spectral lines corresponding to the resonant cavity modes. When compared to the single peaked spectra of the planar cavity at 1180 nm, this is evidence of strong optical confinement. The ground state transition of the QD is centered at 1245 nm (at 293K), the cavity modes are therefore pumped by the excited states of the QDs. The inhomogeneous broadening of the QD emission (measured to be 25 nm on similar samples without cavity) ensures that the narrow spectral features are related to the cavity modes and not to QD electronic states. As the diameter of the current aperture is reduced we observe a blueshift of the cavity ground state transition (Figure 6.16(b)) and an increase in the splitting between cavity modes consistent with the conventional theoretical trend for increased lateral confinement. We stress that the energy shift (45 meV for the $0.7 \mu\text{m}$ -diam devices) is much larger than the shift commonly measured in VCSELs and comparable to the shift observed in micropillars.

In order to model the cavity modes, we applied the “effective index” method which is

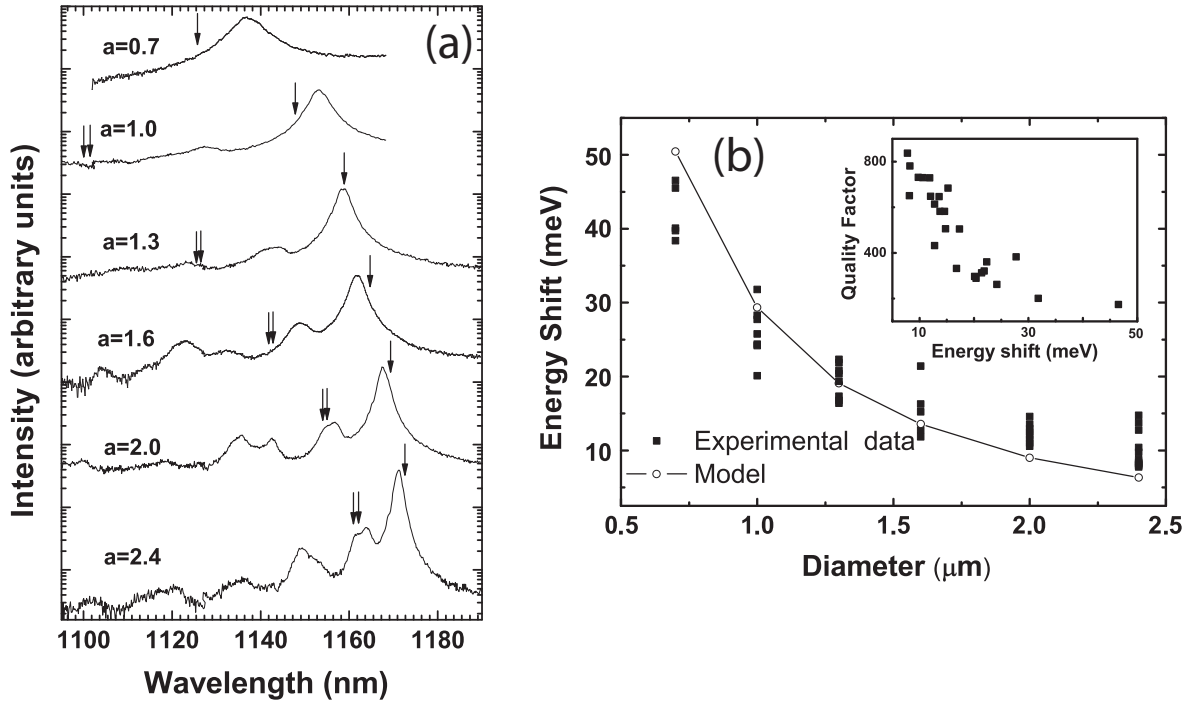


Figure 6.16: (a) Electroluminescence spectra (293K) of microcavities with different oxide apertures (aperture diameter is indicated for each spectra). The blueshift of the resonant line and the increased mode separation for smaller diameters are characteristic of strong optical confinement in 3D. The arrows indicate the positions of the modes predicted by the effective index model. The modes indicated on each spectrum are, respectively, from right to left: HE11, HE21, and EH01, according to the standard convention [Yariv 91] (b) Comparison of the experimental shift of the fundamental cavity resonance (dots) and prediction by the effective index model (continuous line). Inset: cavity quality factor is plotted as a function of the shift in energy with respect to the planar cavity emission.[Zinoni 04]

based on the assumption that the transverse component of the resonant electromagnetic field is independent of the longitudinal component, an assumption usually correct for planar cavities or three-dimensional (3D) cavities with lateral dimensions larger than the wavelength [Yariv 91]. In this *effective index* approach [Hadley 95] the cavity is treated as a two-dimensional circular waveguide with core and cladding indexes given by an effective index weighted by the standing field in the axial direction. In this framework, we solved numerically the eigenvalue equation for the longitudinal standing wave in the core (unoxidized

region) approximated to a planar cavity. The resonant wavelength obtained was 1193 nm while the averaged refractive index weighted with the standing field intensity was 3.053. For the cladding (oxidized region) the refractive index was calculated to be 2.757 from the relation:[Hadley 95] $\Delta\lambda/\lambda=\Delta n/n$. Using these values we applied the numerical methods used for evaluating the confined modes for a step index optical fiber [Yariv 91] (shown as arrows in Figure 6.16(a) and as a continuous line in Figure 6.16(b). Good agreement was found between experimental evidence and calculated modes for apertures down to $2.0\ \mu\text{m}$. Below this value, the cavity dimensions become comparable to the resonant wavelength and we observe a significant difference between the experimental and theoretical splitting of the cavity modes, thus confirming that the confinement of the transverse component becomes substantial in the smaller devices where the approximation in the effective index model is no longer valid. It is interesting to note that model predicts single mode propagation when the normalized frequency falls below 2.405 (the first zero in the Bessel J_0 function) which corresponds to an oxide aperture of 690 nm in our devices. In figure 6.16(a) the QD LEDs with apertures estimated at $0.7\ \mu\text{m}$ indeed do not show any evidence of multimode confinement, at least within the broad emission spectrum of the QDs.

We observe a significant spread in the resonant energies for devices with the same nominal diameter. This can be attributed to variations in the mesa diameters and oxidized length. The design quality factor for the QD cavity is 1000, however as we have discussed in the previous chapter, this value can be reduced in practice due to scattering at the oxide interfaces in small devices and waveguiding in the bottom DBR. Because actual diameters can vary among nominally identical devices we plot in the inset to figure 6.16(b) the quality factor measured over 40 devices as a function of the resonant energy shift. Beside the variations in the Q value, probably due to the fluctuating quality of the mesa etching (the dimensions being comparable to the resolution of our optical lithography), a clear trend of decreasing Q for increasing lateral confinement is observed. The bests Q values are 850 for large (planar) structures, down to 150–200 for the smallest ($0.7\ \mu\text{m}$ diameter apertures).

These quality factors are smaller than those obtained with micropillar structure, this will be confirmed by simulations described in the last section. Since micropillar structure is not well adapted to current injection du to the vertical sidewalls, and small contact area on the top of the micropillar, we decided to investigate another approach that we called "planarized micropillar" as an alternative to the oxide aperture approach.

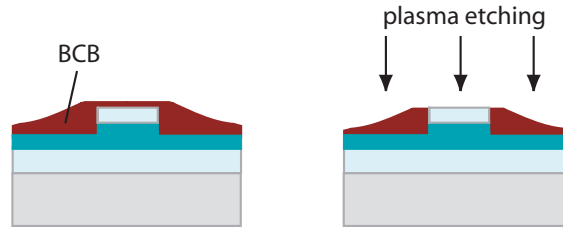


Figure 6.17: Deposition (a) and dry etching (b) of BCB resin

6.4.5 Alternative approach: planarized micropillar

Electrical and strong optical confinement have been achieved at the same time in a cavity defined laterally by a thick oxide layer. However results presents some limitations.

- A large scattering of oxidation length, possibly due to an inhomogenous etching depth on the sample results in a poor reproducibility of the optical and electrical response.
- We observe a parasitic oxidation of top DBR despite of its lower Al composition.
- We observe on the I-V characteristics a high threshold voltage.
- The quality factors are too low to observe an enhancement of the spontaneous emission

We tried to find procedure avoiding oxidation aperture to test if the poor quality factor can be related to it. We processed two structures with and without oxide aperture by using a polymer derived from B-staged bisbenzocyclobutene (BCB) monomers. This resin is an isolant and can be substituted to the Si_3N_4 . The advantage of BCB is that it planarizes the surface on which it is spined. BCB is deposited after mesa etching step. It smoothes the surface as shown on the figure 6.17. BCB thickness is then not homogeneous on the surface, thinner on the top of the mesa than on the AlGaAs layer. An etching process removed the BCB on the top on the mesa but not on the AlGaAs. We compare one process with BCB deposition, oxidation of bottom DBR without oxidation of AlGaAs surface and partial oxidation of top DBR (process A), and one process with BCB deposition and oxidation of AlGaAs layer on surface together with bottom DBR (process B). Final structure after processing are sketched on the figure 6.18.

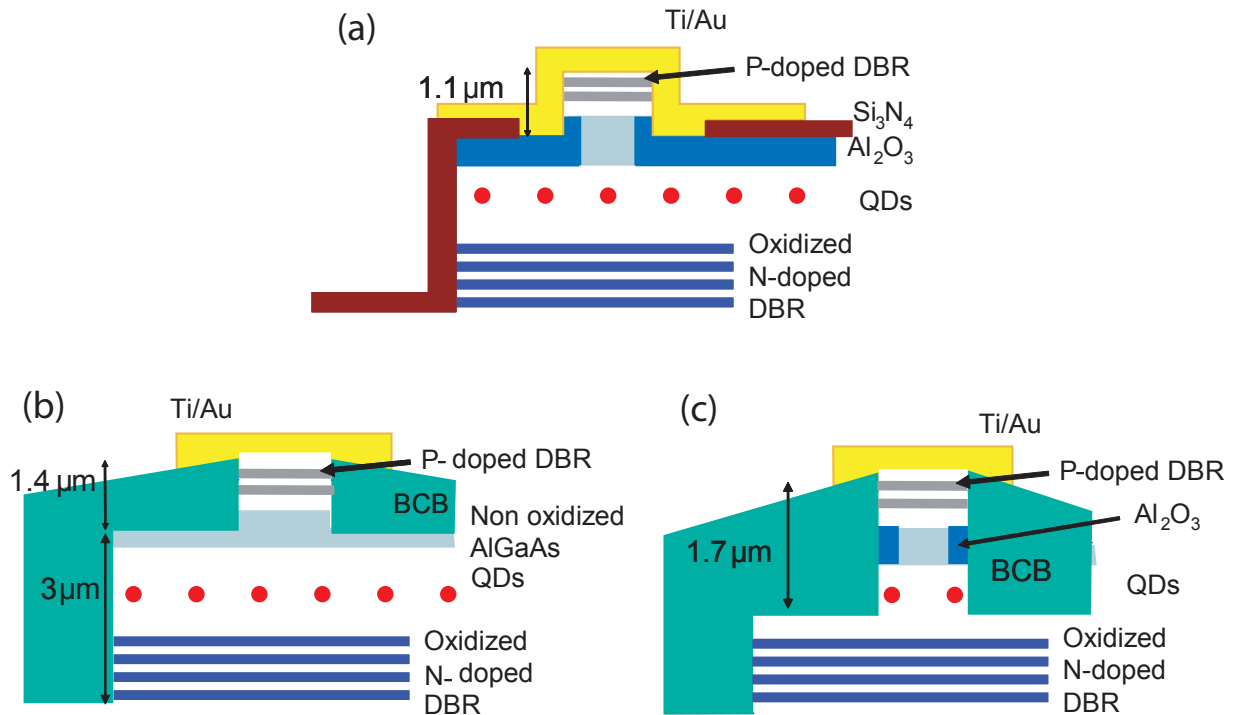


Figure 6.18: (a) First process with Si_3N_4 and oxide aperture (b) process A: BCB and oxidation of bottom DBR (c) process B: BCB and oxide aperture

Results

I-V curves have been measured from both devices and show a similar voltage threshold at 10V as compared to the first approach.

Luminescence versus current (figure 6.19) shows a luminescence efficiency comparable to the first structure. We note that luminescence efficiency is slightly higher for the structure without oxide aperture, which would tend to suppose that oxide aperture enhances non radiative recombination.

Electroluminescence spectra (figure 6.20) at room temperature for different device sizes between 2 and 10 μm diameter. Planar quality factor (figure 6.21(a)) is lower for both structures as compared to the first process, probably due to a lower DBR reflectivity on those structures, but follows the same trend with energy shift as shown on figure 6.21(b) which shows that radiative losses mechanisms are similar for all processes.

These investigations allowed us to give some conclusions:

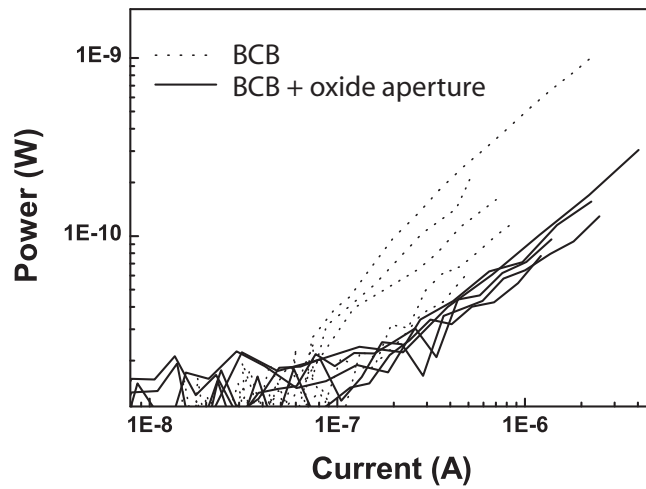


Figure 6.19: Luminescence power versus excitation power for mesa with diameter ranging from 2 to 10 μm . Dotted lines correspond to process B, black lines to process A.

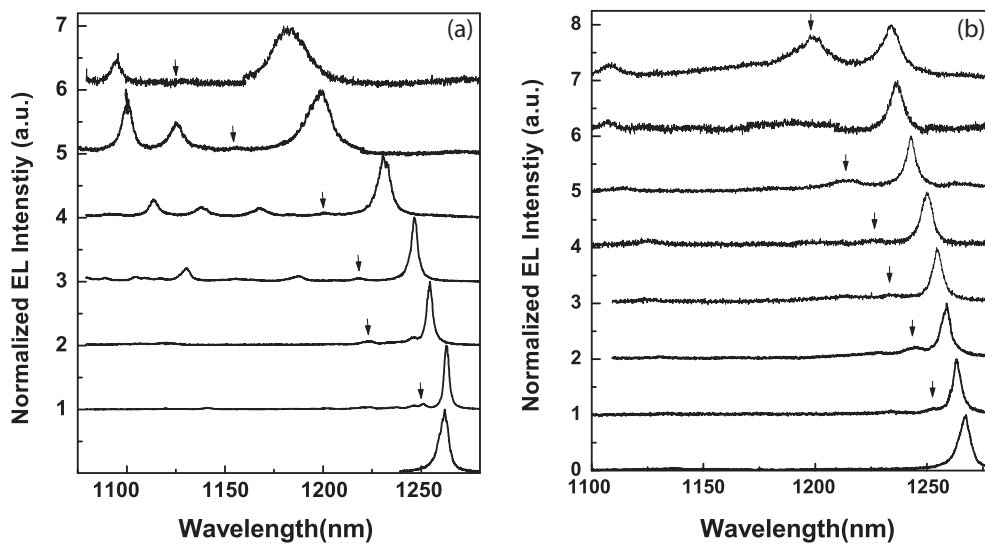


Figure 6.20: Electroluminescence spectra from mesa with diameter ranging from 2 to 10 μm . Excitation current between 0.5 and 1 μA (a) process A with BCB (b) process B with BCB and oxide aperture. Arrows show the second optical mode measured on the spectra to evidence the energy shift.

Process of planarized micropillars has been performed and allow to obtain electroluminescence spectra which evidence of an optical confinement.

Q factors are still low because etching is not deep enough as compared to a micropillar structure.

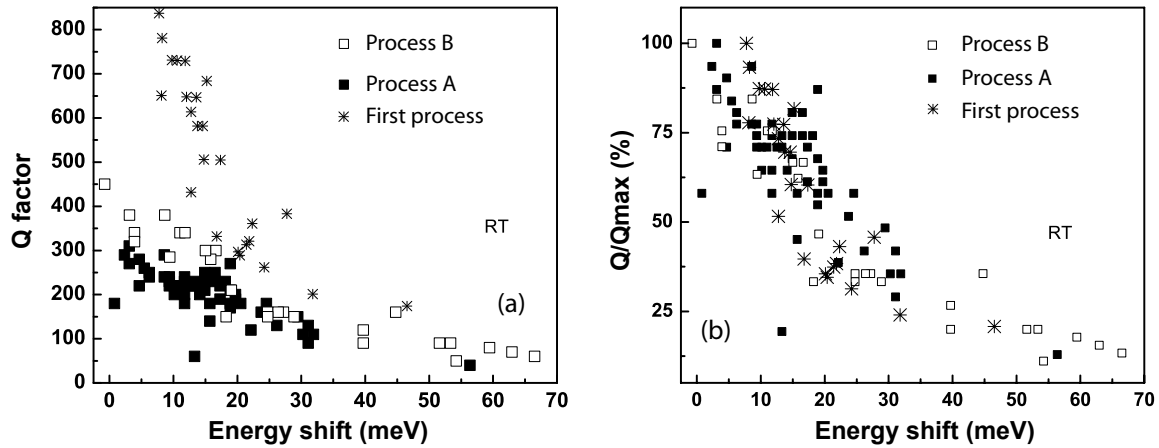


Figure 6.21: (a) Quality factor and (b) normalized Q factor, as function of the energy shift for the three processes.

The lower external efficiency of the sample type B shows the influence of non-radiative recombinations by etching the active region.

Comparison with simulations results

Simulation of optical mode confinement in our oxide confined structure have been done thanks to the collaboration with M. Streiff and B. Witzigmann from Swiss Federal Institute of technology (ETHZ) in Zurich. Maxwell's vectorial wave equation has been solved in the frequency domain by vectorial finite elements, subject to an open boundary, taking into account diffraction and radiation of electromagnetic waves. The optical mode solver was calibrated with measured the electroluminescence spectra of the first structure structure with oxide diameters ranging from 2.4 to $0.7 \mu\text{m}$. Excellent agreement was achieved between measurements and simulations as shown on figure 6.22. The mode field was also simulated for the oxidized microcavity LED and a more conventional micropillar structure. As shown on figure 6.23, mode confinement appears more effective in micropillar structure. Q factor was also found superior for micropillar than for oxide aperture approach. This leads to suppose that excessive diffraction losses for oxide confinements with diameters smaller than $1 \mu\text{m}$ are the main cause of degradation of the cavity Q factor and, hence, the Purcell factor in the oxide confined microcavity.

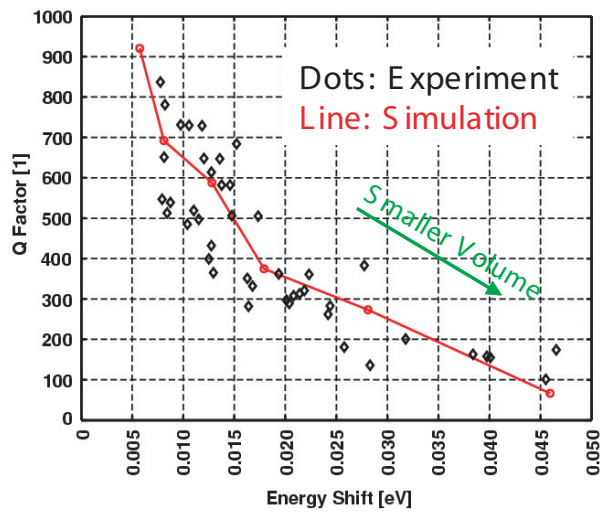


Figure 6.22: Simulation (solid line) and measurement (diamonds) of the cavity Q factor versus energy shift (with respect to $1.0508 \text{ eV} \equiv 1180 \text{ nm}$) of HE11 type optical mode for oxide radii from $0.35 \mu\text{m}$ to $1.2 \mu\text{m}$. [Streiff 05]

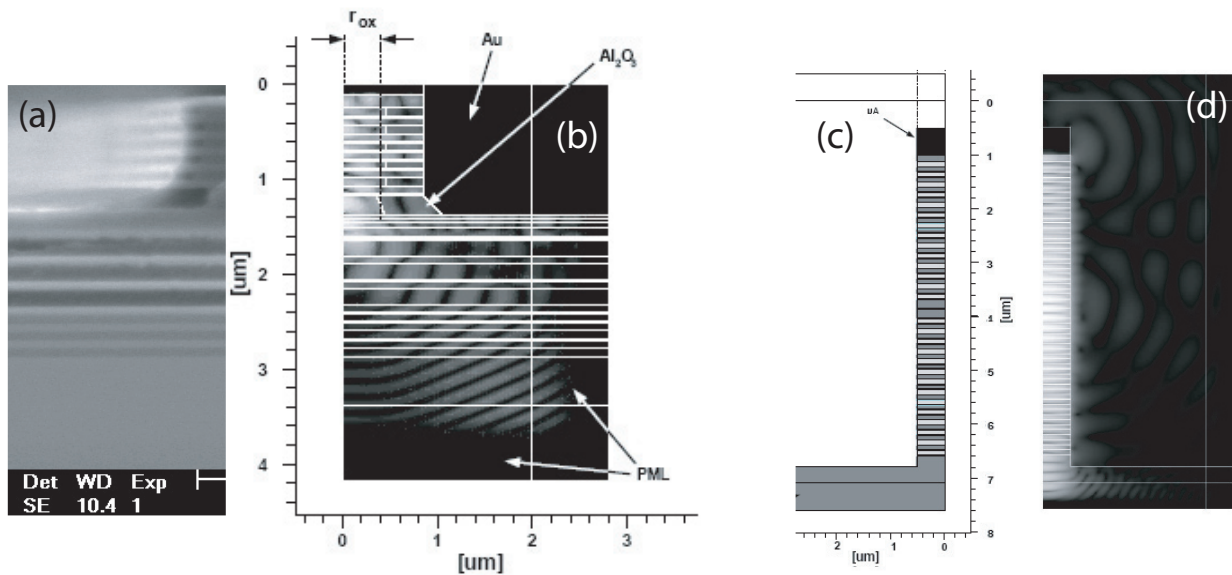


Figure 6.23: Oxide confined microcavity device structure used for calibration: (a) SEM picture of sample, (b) absolute value of real part of HE11 type electric field shown on logarithmic gray scale. PML: Perfect Matched Layers. Micropillar device structure used for comparison: (top DBR: 14, bottom DBR: 13.5), (c) micropillar device structure, (d) absolute value of real part of HE11 type electric field shown on logarithmic gray scale. [Streiff 05]

6.5 Conclusion

This chapter shows evolution of different investigations performed to fabricate a single quantum dot LED.

We first studied LEDs with weak optical confinement. The metal-aperture approach for filtering QD emission was not satisfying due to the difficulty to suppress stray light from wave-guided modes.

The oxide aperture approach provides a selective current injection and single QD emission around 1300 nm have been performed. However number of excited QDs is still too high for anticorrelation experiment. Moreover bottom emitting structure gives technical problem for the sample mounting inside the cryostat and for the sample cooling down to 4K. A top emitting structure with annular contact to provide both n-and p-contacts at the top side has been grown, processes are under way.

Study of LEDs with strong optical confinements, shows a too much scattering at the oxide aperture due to the high variation of refractive index at the interface with Al_2O_3 layer. We encountered also some problem with current injection through DBRs, probably to a high amount of Oxygen in the structure. Finally etching through the active region is shown to degrade the radiative efficiency. Since micropillar and oxide aperture designs appear not suitable for our application, we now concentrate on an alternative approach as a photonic crystal LED structure. This structure avoids problems related to the etched sidewalls and oxide aperture. The structure is grown and processing is under way.

Conclusions

The aim of this thesis was to realize and characterize a single photon source from self-assembled quantum dots (QDs) emitting at 1300 nm. The small number of publications in this field shows that this topic is still at its beginning. Indeed, it poses a twofold challenge for epitaxial growth and optical measurements. Both sides have been addressed in the framework of this thesis.

First, the areal quantum dot density has to be low in order to easily isolate a single quantum dot in a device. But a long emission wavelength requires also a large quantum dot size. This combination can not be obtained by the common approach consisting of reducing the InAs thickness: it results in a lower QD density but also in a decreasing QD size which leads to a blueshift of the emission wavelength. Chapter 3 shows that this dilemma can be solved by drastically reducing the InAs growth rate. A low-density QD ($2 \cdot \mu\text{m}^{-2}$) is obtained with an emission wavelength at 1200 nm at low temperature (10K). The further redshift to 1300 nm is reached by using a 5 nm-thick $\text{In}_{0.15}\text{Ga}_{0.85}\text{As}$ capping layer after the QD layer deposition. Structural characterization by transmission electron microscopy (TEM) shows that the quantum dot dimensions (~ 10 nm height) and In content ($> 60\%$) are much larger than the typical values for InAs self-assembled QDs. Our growth method has the advantage to provide a single distribution of QDs, with a very good size homogeneity, which is important for device reproducibility.

Due to the low areal QD density, carrier capture from the wetting layer (WL) to the QDs is expected to be less efficient, potentially leading to an accumulation of carriers in the WL and a reduced luminescence efficiency. Chapter 4 reports optical characterizations with continuous-wave and time-resolved photoluminescence measurements of these low-density QDs as compared to higher densities. The excitation power dependence of the relative intensity of ground state and wetting layer signals shows an efficient carrier capture mechanism into the QDs even for densities as low as few QDs/ μm^2 . However, the effect of WL carriers in low-density QDs at moderate excitation densities is evidenced in a complex PL rise dynamics which is not for the moment fully understood: A delay of the GS luminescence is observed for the low-density samples and is especially important at high excitation power.

A similar delay is observed for a single quantum dot in the PL transient of the exciton in the ground state. Temperature dependence measurements performed on low-density QDs capped by InGaAs show a good stability of their luminescence intensity. The evolution with temperature of the lifetime at the GS energy is similar to that reported for higher-density QDs samples. Our low-density QDs appear thus suitable for further applications in single quantum dot devices.

The second challenge concerns the detection of single photons 1300 nm. For the near-infrared range, InGaAs or Ge avalanche photodiodes must be used, with a much lower quantum efficiency and much higher noise than silicon-based detection system. Chapter 5 and 6 concentrate on the single quantum dot spectroscopy under optical and electrical pumping, respectively.

In chapter 5, microphotoluminescence spectroscopy at low-temperature reveals emission lines which are characteristic of a single QD emission. Exciton-biexciton signals are observed up to a temperature of 80K. Antibunching experiments demonstrate that our low-density QD are an efficient source of single photons. However, an increasing background does not allow anticorrelation experiments for temperatures higher than 50K and high excitation power. Resonant excitation should improve the signal-to-noise ratio in these measurements.

Finally, single photon emission under electrical pumping is the last requirement for the practical application of single quantum dot devices. Chapter 6 shows our progress in this field. Electrical injection requires a more complex fabrication process and gives further problems relative to the current spreading and carrier diffusion. After testing a simple LED structure with only a filtering of the QD emission through a metallic aperture, we observed that detection of single quantum dot emission required a control of current injection as well. A current restriction using an oxide aperture as current blocking layer was finally the more successful approach. Sharp lines corresponding to single electronic transitions have been observed. Improvement of the thermal contact of the sample would lead to a decreasing background signal and allow anticorrelation experiments.

This work has then shown that it is possible to realize a single-photon source for fiber-based quantum communications from self-assembled InAs/GaAs quantum dots, which is an important progress on its own and for the future application of single quantum dot devices. The next step is to work on the localization of the QDs: As we observed through our first measurements on low-density QD in three-dimensional microcavities, this would make

the coupling between QD and the cavity mode easier, result in a higher reproducibility, a higher extraction efficiency and thus would facilitate the detection. Recent development of single-photon detectors based on NbN superconducting nanostructures [Gol'tsman 01] has moreover given a strong impetus to the detector technology in terms of sensitivity and efficiency which is very promising for future applications of single-photon sources.

Bibliography

- [Abram 98] I. Abram, I. Robert & R. Kuszelewicz. *Spontaneous emission control in semiconductor microcavities with metallic or Bragg mirrors*. IEEE Journal of Quantum Electronics, vol. 34, pages 71–76, 1998. 88
- [Adler 96] F. Adler, M. Geiger, A. Bauknecht, F. Scholz, H. Schweizer, M. H. Pilkuhn, B. Ohnesorge & A. Forchel. *Optical transitions and carrier relaxation in self-assembled InAs/GaAs quantum dots*. Journal of Applied Physics, vol. 80, page 4019, 1996. 74
- [Alloing 05] B. Alloing, C. Zinoni, V. Zwiller, L.H. Li, C. Monat, M. Gobet, G. Buchs, A. Fiore, E. Pelucchi & E. Kapon. *Growth and characterization of single quantum dots emitting at 1300 nm*. Applied Physics Letters, vol. 86, page 101908, 2005. 22
- [Ambrose 94] W. P. Ambrose, P. M. Goodwin, J. C. Martin & R. A. Keller. *Single molecule detection and photochemistry on a surface using near-field optical excitation*. Physical Review Letter, vol. 72, pages 160–163, 1994. 18
- [Arakawa 82] Y. Arakawa & H. Sakaki. *Multidimensional quantum well laser and temperature dependence of its threshold current*. Applied Physics Letters, vol. 40, pages 939–941, 1982. 13
- [Bacher 99] G. Bacher, R. Weigand, J. Seufert, V. D. Kulakovskii, N. A. Gippius, A. Forchel, K. Leonardi & D. Hommel. *Biexciton versus Exciton Lifetime in a Single Semiconductor Quantum Dot*. Physical Review Letters, vol. 83, page 4417, 1999. 82
- [Badolato 05] A. Badolato, K. Hennessy, M. Atatüre, J. Dreiser, E. Hu, P. M. Petroff & A. Imamoglu. *Deterministic Coupling of Single Quantum Dots to Single Nanocavity Modes*. Science, vol. 308, page 1158, 2005. 88

- [Baier 04] M. H. Baier, C. Constantin, E. Pelucchi & E. Kapon. *Electroluminescence from a single pyramidal quantum dot in a light-emitting diode*. Applied Physics Letters, vol. 84, page 1967, 2004. 95
- [Barabasi 97] Albert-Laszlo Barabasi. *Self-organized superlattice formation in II-IV and III-V semiconductors*. Applied Physics Letters, vol. 70, no. 6, pages 764–766, 1997. 44
- [Bartelt 92] M. C. Bartelt & J. W. Evans. *Scaling analysis of diffusion-mediated island growth in surface adsorption processes*. Physical Review B, vol. 46, page 12675, 1992. 56
- [Basché 92] Th. Basché, W. E. Moerner, M. Orrit & H. Talon. *Photon antibunching in the fluorescence of a single dye molecule trapped in a solid*. Physical Review Letters, vol. 69, pages 1516–1519, 1992. 18
- [Bayer 02] M. Bayer & A. Forchel. *Temperature dependence of the exciton homogeneous linewidth in $In_{0.60}Ga_{0.40}As/GaAs$ self-assembled quantum dots*. Physical Review B, vol. 65, page 041308, 2002. 81
- [Benisty 98] H. Benisty, R. Stanley & M. Mayer. *Method of source terms for dipole emission modification in modes of arbitrary planar structures*. Journal of Optical Society of America A, vol. 15, page 1192, 1998. 97
- [Bennett 92] C. H. Bennett, G. Brassard & A.K. Eckert. *Quantum cryptography*. Scientific American, vol. 267, pages 50–57, 1992. 14
- [Bennett 05a] A. J. Bennett, D. C. Unitt, P. See, A. J. Shields, P. Atkinson, K. Cooper & D. A. Ritchie. *Microcavity single-photon-emitting diode*. Applied Physics Letters, vol. 86, page 181102, 2005. 95, 110
- [Bennett 05b] A. Bennett, D. Unitt, P. Atkinson, D. Ritchie & A. Shields. *High performance single photon sources from photolithographically defined pillar microcavities*. Optics Express, vol. 13, pages 50–55, 2005. 38
- [Bennett 05c] A.J. Bennett, D.C. Unitt, P. Atkinson, D.A. Ritchie & A.J. Shields. *High-efficiency single-photon sources based on $InAs/GaAs$ quantum*

- dots in pillar microcavities*. *Physica E*, vol. 26, pages 391–394, 2005. 91
- [Boschetti 00] C. Boschetti. <http://www.las.inpe.br/cesar/Infrared/rheed.htm>, 2000. 30
- [Brassard 00] G. Brassard, N. Lütkenhaus, T. Mor, & B. C. Sanders. *Limitations on Practical Quantum Cryptography*. *Physical Review Letters*, vol. 85, pages 1330–1333, 2000. 16
- [Bruls 02] D. M. Bruls, J. W. A. M. Vugs, P. M. Koenraad, H. W. M. Salemink, J. H. Wolter, M. Hopkinson, M. S. Skolnick, Fei Long & S. P. A. Gill. *Determination of the shape and indium distribution of low-growth-rate InAs quantum dots by cross-sectional scanning tunneling microscopy*. *Applied Physics Letters*, vol. 81, page 1708, 2002. 59
- [Buttler 98] W. T. Buttler, R. J. Hughes, P. G. Kwiat, G. G. Luther, G. L. Morgan, J. E. Nordholt, C. G. Peterson & C. M. Simmons. *Free-space quantum-key distribution*. *Physical Review A*, vol. 57, pages 2379–2382, 1998. 16
- [Chu 99] L. Chu, M. Arzberger, G. Böhm & G. Abstreiter. *Influence of growth conditions on the photoluminescence of self-assembled InAs/GaAs quantum dots*. *Journal of Applied Physics*, vol. 85, page 2355, 1999. 48
- [Coleiny 03] G. Coleiny & R. Venkat. *Theoretical study of In desorption during MBE growth of InGaAs/GaAs*. *Journal of Crystal Growth*, vol. 250, page 22, 2003. 59
- [Convertino 04] A. Convertino, L. Cerri, G. Leo & S. Viticoli. *Growth interruption to tune the emission of InAs quantum dots embedded in InGaAs matrix in the long wavelength region*. *Journal of Crystal Growth*, vol. 261, pages 458–465, 2004. 53
- [Dobbs 97] H. T. Dobbs, D. D. Vvedensky, A. Zangwill, J. Johansson, N. Carlsson & W. Seifert. *Mean-Field Theory of Quantum Dot Formation*. *Physical Review Letters*, vol. 79, page 897, 1997. 31, 44

- [Dubrovskii 04] V. G. Dubrovskii, G. E. Cirlin & V. M. Ustinov. *The effective thickness, temperature and growth rate behavior of quantum dot ensembles*. *physica status solidi (b)*, vol. 241, page R42, 2004. 46
- [Ellis 06] D. J. P. Ellis, A. J. Bennett, A. J. Shields, P. Atkinson & D. A. Ritchie. *Electrically addressing a single self-assembled quantum dot*. *Applied Physics Letters*, vol. 88, page 133509, 2006. 95
- [Englund 05] D. Englund, D. Fattal, E. Waks, G. Solomon, B. Zhang, T. Nakaoka, Y. Arakawa, Y. Yamamoto & J. Vuckovic. *Controlling the Spontaneous Emission Rate of Single Quantum Dots in a Two-Dimensional Photonic Crystal*. *Physical Review Letters*, vol. 95, page 013904, 2005. 88
- [Fafard 99] S. Fafard & C. Nì. Allen. *Intermixing in quantum-dot ensembles with sharp adjustable shells*. *Applied Physics Letters*, vol. 75, page 2374, 1999. 51
- [Finley 01] J. J. Finley, A. D. Ashmore, A. Lemaître, D. J. Mowbray, M. S. Skolnick, I. E. Itskevich, P. A. Maksym, M. Hopkinson & T. F. Krauss. *Charged and neutral exciton complexes in individual self-assembled In(Ga)As quantum dots*. *Physical Review B*, vol. 63, page 073307, 2001. 80, 82
- [Finnie 02] P. Finnie, B. J. Riel & Z. R. Wasilewski. *Reflection high-energy electron diffraction observation of the dynamics of semiconductor quantum dot formation and decay*. *Journal of Vacuum Science and Technology B*, vol. 20, page 2210, 2002. 31
- [Fiore 00] A. Fiore, P. Borri, W. Langbein, J. M. Hvam, U. Oesterle, R. Houdré, R. P. Stanley & M. Ilegems. *Time-resolved optical characterization of InAs/InGaAs quantum dots emitting at 1.3 μm* . *Applied Physics Letters*, vol. 76, page 3430, 2000. 74
- [Fiore 02] A. Fiore, J. X. Chen & M. Ilegems. *Scaling quantum-dot light-emitting diodes to submicrometer sizes*. *Applied Physics Letters*, vol. 81, pages 1756–1758, 2002. 95, 97, 101, 106

- [Fiore 04] A. Fiore, M. Rossetti, B. Alloing, C. Paranthoen & J. X. Chen. *Carrier diffusion in low-dimensional semiconductors: A comparison of quantum wells, disordered quantum wells, and quantum dots*. Physical Review B, vol. 70, page 205311, 2004. 102, 105
- [Foxon 78] C.T. Foxon & B. A. Joyce. *Surface processes controlling the growth of $Ga_xIn_{1-x}As$ and $Ga_xIn_{1-x}P$ alloy films by MBE*. Journal of Crystal Growth, vol. 44, page 75, 1978. 59
- [Frank 49] F.C. Frank & J.H. van der Merwe. *One-dimensional dislocations. II. Misfitting monolayers and oriented overgrowth*. Proceedings of the Royal Society of London A, vol. 198, pages 216–225, 1949. 40
- [Gayral 01] B. Gayral. *Controlling spontaneous emission dynamics in semiconductor micro cavities*. Annales de Physique Française, vol. 26, pages 1–135, 2001. 90
- [Gerardino] A. Gerardino, M. Francardi, L. Balet, C. Monat, C. Zinoni, B. Alloing, L.H. Li, N. Le Thomas, R. Houdré & A. Fiore. *Fabrication and characterization of point defect photonic crystal nanocavities at telecom wavelength*. Microelectronic Engineering, submitted. 92
- [Goldstein 85] L. Goldstein, F. Glas, J. Y. Marzin, M. N. Charasse & G. Le Roux. *Growth by molecular beam epitaxy and characterization of $InAs/GaAs$ strained-layer superlattices*. Applied Physics Letters, vol. 47, page 1099, 1985. 40
- [Gol'tsman 01] G. N. Gol'tsman, O. Okunev, G. Chulkova, A. Lipatov, A. Semenov, K. Smirnov, B. Voronov, A. Dzardanov, C. Williams & R. Sobolewski. *Picosecond superconducting single-photon optical detector*. Applied Physics Letters, vol. 79, pages 705–707, 2001. 125
- [Gérard 95] J. M. Gérard, J. B. Génin, J. Lefebvre, J. M. Moison, N. Lebouché & F. Barthe. *Optical investigation of the self-organized growth of $InAs/GaAs$ quantum boxes*. Journal of Crystal Growth, vol. 150, pages 351–356, 1995. 53

- [Gérard 96] J. M. Gérard, D. Barrier, J. Y. Marzin, R. Kuszelewicz, L. Manin, E. Costard, V. Thierry-Mieg & T. Rivera. *Quantum boxes as active probes for photonic microstructures: The pillar microcavity case*. Applied Physics Letters, vol. 69, page 449, 1996. 90
- [Gérard 98] J. M. Gérard, B. Sermage, B. Gayral, B. Legrand, E. Costard & V. Thierry-Mieg. *Enhanced Spontaneous Emission by Quantum Boxes in a Monolithic Optical Microcavity*. Physical Review Letters, vol. 81, pages 1110–1113, 1998. 91
- [Gruber 97] A. Gruber, A. Dräbenstedt, C. Tietz, L. Fleury, J. Wrachtrup & C. von Borczyskowski. *Scanning Confocal Optical Microscopy and Magnetic Resonance on Single Defect Centers*. Science, vol. 276, page 2012, 1997. 18
- [Grundmann 95] M. Grundmann, J. Christen, N. N. Ledentsov, J. Böhrer, D. Bimberg, S. S. Ruvimov ‡, P. Werner, U. Richter, U. Gösele, J. Heydenreich, V. M. Ustinov, A. Yu. Egorov, A. E. Zhukov, P. S. Kop'ev & Zh. I. Alferov. *Ultrannarrow Luminescence Lines from Single Quantum Dots*. Physical Review Letters, vol. 74, no. 20, pages 4043–4046, May 1995. 45
- [Gurioli 06] M. Gurioli, A. Vinattieri, M. Zamfirescu, M. Colocci, S. Sanguinetti & Richard Notzel. *Recombination kinetics of InAs quantum dots: Role of thermalization in dark states*. Physical Review B (Condensed Matter and Materials Physics), vol. 73, no. 8, page 085302, 2006. 74
- [Hadley 95] G. R. Hadley. *Effective index model for vertical-cavity surface-emitting lasers*. Optics Letters, vol. 81, page 1756, 1995. 115, 116
- [Hanbury-Brown 56] R. Hanbury-Brown & R.Q. Twiss. *Correlation between Photons in two Coherent Beams of Light*. Nature, vol. 177, page 27, 1956. 84
- [Hartmann 97] A. Hartmann, L. Loubies, F. Reinhardt & E. Kapon. *Self-limiting growth of quantum dot heterostructures on nonplanar 111B substrates*. Applied Physics Letters, vol. 71, pages 1314–1316, 1997. 40

- [Heyn 05] Ch. Heyn, A. Boltz, T. Matlezopoulos, R. L. Johnson & W. Hansen. *Intermixing in self-assembled InAs quantum dot formation*. Journal of Crystal Growth, vol. 278, page 46, 2005. 59
- [Håkanson 03] U. Håkanson, J. Persson, F. Persson, H. Svensson, L. Montelius & M.K-J Johansson. *Nano-aperture fabrication for single quantum dot spectroscopy*. Nanotechnology, vol. 14, page 675–679, 2003. 76
- [Huffaker 98] D. L. Huffaker, L. A. Graham & D. G. Deppe. *Ultrannarrow electroluminescence spectrum from the ground state of an ensemble of self-organized quantum dots*. Applied Physics Letters, vol. 72, page 214, 1998. 95
- [Huttner 95] B. Huttner, N. Imoto, N. Gisin & T. Mor. *Quantum cryptography with coherent states*. Physical Review A, vol. 51, pages 1863–1869, 1995. 16
- [Itskevich 00] I. E. Itskevich, S. I. Rybchenko, I. I. Tartakovskii, S. T. Stoddart, A. Levin, P. C. Main, L. Eaves, M. Henini & S. Parnell. *Stark shift in electroluminescence of individual InAs quantum dots*. Applied Physics Letters, vol. 76, pages 3932–3934, 2000. 95
- [Jeffrey 06] C. A. Jeffrey, E. H. Conrad, R. Feng, M. Hupalo, C. kim, P. J. ryan, P. F. Miceli & M. C. Tringides. *Influence of Quantum Size Effects on Island Coarsening*. Physical Review Letters, vol. 96, page 106105, 2006. 56
- [Jesson 98] D. E. Jesson, G. Chen, K. M. Chen & S. J. Pennycook. *Self-Limiting Growth of Strained Faceted Islands*. Phys. Rev. Lett., vol. 80, no. 23, pages 5156–5159, Jun 1998. 44
- [John 87] S. John. *Strong localization of photons in certain disordered dielectric superlattices*. Physical Review Letters, vol. 58, page 2486, 1987. 92
- [Joyce 82] W.B. Joyce. *Carrier transport in double-heterostructure active layers*. Journal of Applied Physics, vol. 53, pages 7235–7239, 1982. 105, 106

- [Joyce 00] P. B. Joyce, T. J. Krzyzewski, G. R. Bell, T. S. Jones, S. Malik, D. Childs & R. Murray. *Effect of growth rate on the size, composition, and optical properties of InAs/GaAs quantum dots grown by molecular-beam epitaxy*. Physical Review B, vol. 62, page 10891, 2000. 46, 59
- [Joyce 01] P. B. Joyce, T. J. Krzyzewski, G. R. Bell & T. S. Jones. *Surface morphology evolution during the overgrowth of large InAs-GaAs quantum dots*. Applied Physics Letters, vol. 79, page 3615, 2001. 59
- [Kaiser 02] S. Kaiser, T. Mensing, L. Worschech, F. Klopf, J.P. Reithmaier & A. Forchel. *Optical spectroscopy of single InAs/InGaAs quantum dots in a quantum well*. Applied Physics Letters, vol. 81, page 4898, 2002. 22, 79
- [Kaizu 01] T. Kaizu & K. Yamaguchi. *Self Size-Limiting Process of InAs Quantum Dots Grown by Molecular Beam Epitaxy*. Japanese Journal of Applied Physics, vol. 40, pages 1885–1887, 2001. 62
- [Karachinsky 04] L. Ya. Karachinsky, S. Pellegrini, G.S. Buller, A.S. Shkolnik, N. Yu Gordeev, V. P. Evtikhiev & V. B. Novikov. *Time-resolved photoluminescence measurements of InAs self-assembled quantum dots grown on misorientated substrates*. Applied Physics Letters, vol. 84, page 7, 2004. 71
- [Karlsson 02] K. F. Karlsson, E. S. Moskalenko, P. O. Holtz, B. Monemar, W. V. Schoenfeld, J. M. Garcia & P. M. Petroff. *Temperature influence on optical charging of self-assembled InAs/GaAs semiconductor quantum dots*. Applied Physics Letters, vol. 78, page 2952, 2002. 81
- [Kim 99] J. Kim, O. Benson, H. Kan & Y. Yamamoto. *A single-photon turnstile device*. Nature, vol. 397, page 500, 1999. 18, 95
- [Kimble 77] H. J. Kimble, M. Dagenais & L. Mandel. *Photon Antibunching in Resonance Fluorescence*. Physical Review Letters, vol. 39, pages 691–695, 1977. 17, 83

- [Kiraz 01] A. Kiraz, P. Michler, C. Becher, B. Gayral, A. Imamoglu, Lidong Zhang & E. Hu. *Cavity-quantum electrodynamics using a single InAs quantum dot in a microdisk structure*. Applied Physics Letters, vol. 78, page 3932, 2001. 88
- [Kiraz 02] A. Kiraz, S. Fälth, C. Becher, B. Gayral, W. V. Schoenfeld, P. M. Petroff, L. Zhang, E. Hu & A. Imamoglu. *Photon correlation spectroscopy of a single quantum dot*. Physical Review B, vol. 65, page 161303, 2002. 79
- [Kitamura 95] M. Kitamura, M. Nishioka, J. Oshinowo & Y. Arakawa. *In situ fabrication of self-aligned InGaAs quantum dots on GaAs multiautomic steps by metalorganic chemical vapor deposition*. Applied Physics Letters, vol. 66, page 3663, 1995. 52
- [Knill 01] E. Knill, R. Laflamme & G.J. Milburn. *A scheme for efficient quantum computation with linear optics*. Nature, vol. 409, page 46, 2001. 15
- [Kobayashi 96] N. P. Kobayashi, T. R. Ramachandran, P. Chen & A. Madhukar. *In situ, atomic force microscope studies of the evolution of InAs three-dimensional islands on GaAs(001)*. Applied Physics Letters, vol. 68, pages 3299–3301, 1996. 44, 45
- [Krzyzewski 04] T. J. Krzyzewski & T. S. Jones. *Ripening and annealing effects in InAs/GaAs(001) quantum dot formation*. Journal of Applied Physics, vol. 96, pages 668–674, 2004. 58
- [Kuhn 02] A. Kuhn, M. Hennrich & G. Rempe. *Deterministic Single-Photon Source for Distributed Quantum Networking*. Physical Review Letters, vol. 89, page 067901, 2002. 17
- [Kurtsiefer 00] C. Kurtsiefer, S. Mayer, P. Zarda & H. Weinfurter. *Stable Solid-State Source of Single Photons*. Physical Review Letters, vol. 85, page 290, 2000. 18
- [Landin 99] L. Landin, M.-E. Pistol, C. Pryor, M. Persson, L. Samuelson & M. Miller. *Optical investigations of individual InAs quantum dots*:

- Level splittings of exciton complexes.* Physical Review B, vol. 60, page 16640, 1999. 79
- [Ledentsov 96] N. N. Ledentsov, M. Grundmann, N. Kirstaedter, O. Schmidt, R. Heitz, J. Böhrer, D. Bimberg, V. M. Ustinov, V. A. Shchukin, A. Yu. Egorov, A. E. Zhukov, S. Zaitsev, P. S. Kop'ev, Zh. I. Alferov, S. S. Ruvimov, A. O. Kosogov, P. Werner, U. Gösele & J. Heydenreich. *Ordered arrays of quantum dots: formation, electronic spectra, relaxation phenomena, lasing.* Solid State Electronics, vol. 40, pages 785–798, 1996. 47
- [Lee 98] H. Lee, R. Lowe-Webb, W. Yang & P. C. Sercel. *Determination of the shape of self-organized InAs/GaAs quantum dots by reflection high energy electron diffraction.* Applied Physics Letters, vol. 72, pages 812–814, 1998. 30
- [Lemaitre 04] A. Lemaitre, G. Patriarche & F. Glas. *Composition profiling of InAs/GaAs quantum dots.* Applied Physics Letters, vol. 85, page 3717, 2004. 60
- [Lenz 02] A. Lenz, R. Timm, H. Eisele, Ch. Hennig, S. K. Becker, R. L. Sellin, U. W. Pohl, D. Bimberg & M. Dähne. *Reversed truncated cone composition distribution of In_{0.8}Ga_{0.2}As quantum dots overgrown by an In_{0.1}Ga_{0.9}As layer in a GaAs matrix.* Applied Physics Letters, vol. 81, page 5150, 2002. 61
- [Leonard 94] D. Leonard, K. Pond & P. M. Petroff. *Critical layer thickness for self-assembled InAs islands on GaAs.* Physical Review B, vol. 50, pages 11687–11692, 1994. 45, 46, 52
- [Liu 00] N. Liu, J. Tersoff, O. Baklenov, A. L. Holmes, Jr. & C. K. Shih. *Nonuniform Composition Profile in In_{0.5}Ga_{0.5}As Alloy Quantum Dots.* Physical Review Letters, vol. 84, page 334, 2000. 61
- [Liu 05] Wei-Sheng Liu & Jen-Inn Chyia. *Optical properties of InAs quantum dots with InAlAs/InGaAs composite matrix.* Journal of Applied Physics, vol. 97, page 024312, 2005. 49

- [Loudon 83] R. Loudon. *The quantum theory of light*. Clarendon Press, Oxford, 1983. 84
- [Lounis 00] B. Lounis & W. E. Moerner. *Single photons on demand from a single molecule at room temperature*. *Nature*, vol. 491, page 491, 2000. 18
- [Martin 05] R. W. Martin, P. R. Edwards, R. A. Taylor, J. H. Rice, J. H. Na, J. W. Robinson, J. D. Smith, C. Liu & I. M. Watson. *Luminescence properties of isolated InGaN/GaN quantum dots*. *physica status solidi (a)*, vol. 202, page 372, 2005. 21
- [Marzin 94] J.-Y. Marzin, J.-M. Gérard, A. Izraël, D. Barrier & G. Bastard. *Photoluminescence of Single InAs Quantum Dots Obtained by Self-Organized Growth on GaAs*. *Physical Review Letters*, vol. 73, page 716, 1994. 45
- [Matsuda 01] K. Matsuda, K. Ikeda, T. Saiki, H. Tsuchiy, H. Saito & K. Nishi. *Homogeneous linewidth broadening in a $In_{0.5}Ga_{0.5}As/GaAs$ single quantum dot at room temperature investigated using a highly sensitive near-field scanning optical microscope*. *Physical Review B (Rapid Comm.)*, vol. 63, page 121304, 2001. 20
- [Maurer 04] C. Maurer, C. Becher, C. Russo, J. Eschner & R. Blatt. *A single-photon source based on a single Ca^+ ion*. *New Journal of Physics*, vol. 6, page 94, 2004. 17
- [Maximov 00] M. V. Maximov, A. F. Tsatsul'nikov, B. V. Volovik, D. S. Sizov, Yu. M. Shernyakov, I. N. Kaiander, A. E. Zhukov, A. R. Kovsh, S. S. Mikhrin, V. M. Ustinov, Zh. I. Alferov, R. Heitz, V. A. Shchukin, N. N. Ledentsov, D. Bimberg, Yu. G. Musikhin & W. Neumann. *Tuning quantum dot properties by activated phase separation of an InGa(Al)As alloy grown on InAs stressors*. *Physical Review B*, vol. 62, pages 16671–16680, 2000. 49
- [McGee 06] W. M. McGee, T. J. Krzyzewski & T. S. Jones. *Atomic scale structure and morphology of (In, Ga) As-capped InAs quantum dots*. *Journal of Applied Physics*, vol. 99, page 043505, 2006. 60

- [McKeever 04] J. McKeever, A. Boca, A. D. Boozer, R. Miller, J. R. Buck, A. Kuzmich & H. J. Kimble. *Deterministic Generation of Single Photons from One Atom Trapped in a Cavity*. *Science*, vol. 303, page 1992, 2004. 17
- [Michler 00a] P. Michler, A. Imamoglu, M. D. Mason, P. J. Carson, G. F. Strouse & S. K. Buratto. *Quantum correlation among photons from a single quantum dot at room temperature*. *Nature*, vol. 406, pages 968 – 970, 2000. 21
- [Michler 00b] P. Michler, A. Kiraz, C. Becher, W. V. Schoenfeld, P. M. Petroff, L. Zhang, E. Hu & A. Imamoglu. *A Quantum Dot Single-Photon Turnstile Device*. *Science*, vol. 290, page 2282, 2000. 22
- [Min 98] B. Don Min, Y. Kim, E. K. Kim, S.-K Min & M. J. Park. *Suppression of Ostwald ripening in $In_{0.5}Ga_{0.5}As$ quantum dots on a vicinal (100) substrate*. *Physical Review B*, vol. 57, page 11879, 1998. 53
- [Miyazawa 05] T. Miyazawa, K. Takemoto, Y. Sakuma, S. Hirose, T. Usuki, N. Yokoyama, M. Takatsu & Y. Arakawa. *Single-Photon Generation in the 1.55- μ m Optical-Fiber Band from an InAs/InP Quantum Dot*. *Japanese Journal of Applied Physics*, vol. 44, page L620, 2005. 21
- [Monat 06] C. Monat, B. Alloing, C. Zinoni, L. H. Li & A. Fiore. *Nanostructured Current-Confined Single Quantum Dot Light-Emitting Diode at 1300 nm*. *Nano Letters*, vol. 6, pages 1464–1467, 2006. 22, 102, 107, 110
- [Moreau 01a] E. Moreau, I. Robert, J. M. Gérard, I. Abram, L. Manin & V. Thierry-Mieg. *Single-mode solid-state single photon source based on isolated quantum dots in pillar microcavities*. *Applied Physics Letters*, vol. 79, page 2865, 2001. 88
- [Moreau 01b] E. Moreau, I. Robert, L. Manin, V. Thierry-Mieg, J.M. Gérard & I. Abram. *Quantum Cascade of Photons in Semiconductor Quantum Dots*. *Physical Review Letters*, vol. 87, page 183601, 2001. 19

- [Moreau 02] E. Moreau. *Etude d'une source solide monomode de photons uniques constituée par une boîte quantique semi-conductrice dans une micro-cavité optique*. PhD thesis, Université de Paris VI, Paris, France, November 2002. 79
- [Moriwaki 00] O. Moriwaki, T. Someya, K. Tachibana, S. Ishida & Y. Arakawa. *Narrow photoluminescence peaks from localized states in InGaN quantum dot structures*. Applied Physics Letters, vol. 76, page 2361, 2000. 21
- [Morris 99] D. Morris, N. Perret & S. Fafard. *Carrier energy relaxation by means of Auger processes in InAs/GaAs self-assembled quantum dots*. Applied Physics Letters, vol. 75, page 3593, 1999. 73
- [Mozume 92] Teruo Mozume & Isao Ohbu. *Desorption of In during the Growth of GaAs/InGaAs/GaAs heterostructures by Molecular Beam Epitaxy*. Japanese Journal of Applied Physics, vol. 31, page 3277, 1992. 59
- [Mukhametzhanov 99] I. Mukhametzhanov, Z. We, R. Heitz & A. Madhukar. *Punctuated island growth: An approach to examination and control of quantum dot density, size, and shape evolution*. Applied Physics Letters, vol. 75, page 85, 1999. 62
- [Murray 98] R. Murray, D. Childs, S. Malik, P. Siverns, C. Roberts, J.M. Hartmann & P. Stavrinou. *1.3 μm Room Temperature Emission from InAs/GaAs Self-Assembled Quantum Dots*. Japanese Journal of Applied Physics, vol. 38, page 528, 1998. 46
- [Nakata 00] Y. Nakata, K. Mukai, M. Sugawara, K. Ohtsubo, H. Ishikawa & N. Yokoyama. *Molecular beam epitaxial growth of InAs self-assembled quantum dots with light-emission at 1.3 μm* . Journal of Crystal Growth, vol. 208, page 93, 2000. 46
- [Nakayama 95] M. Nakayama, Koji Suyama & Hitoshi Nishimura. *Biexciton formation in GaAs/AlAs type-II superlattices under extremely low excitation powers*. Physical Review B, vol. 51, pages 7870–7873, 1995. 79

- [Nishi 99] Kenichi Nishi, Hideaki Saito, Shigeo Sugou & Jeong-Sik Lee. *A narrow photoluminescence linewidth of 21 meV at 1.35 mm from strain-reduced InAs quantum dots covered by In_{0.2}Ga_{0.8}As grown on GaAs substrates*. Applied Physics Letters, vol. 74, page 1111, 1999. 49, 50
- [Offermans 05] P. Offermans, P. M. Koenraad, R. Nötzel, J. H. Wolter & K. Pierz. *Formation of InAs wetting layers studied by cross-sectional scanning tunneling microscopy*. Applied Physics Letters, vol. 87, page 111903, 2005. 59
- [Oshinowo 94] J. Oshinowo, M. Nishioka, S. Ishida & Y. Arakawa. *Area Density Control of Quantum-Size InGaAs/Ga(Al)As Dots by Metalorganic Chemical Vapor Deposition*. Japanese Journal of Applied Physics, vol. 33, pages L1634–L1637, 1994. 52
- [Panish 93] M.B. Panish & H. Temkin. *Gas source molecular beam epitaxy*. Springer Series in Materials Science 26, 1993. 30
- [Patella 06] F. Patella, F. Arciprete, M. Fanfoni & A. Balzarotti. *Apparent critical thickness versus temperature for InAs quantum dot growth on GaAs(001)*. Applied Physics Letters, vol. 80, page 161903, 2006. 46
- [Patriarche 04] G. Patriarche, L. Largeau & J.-C. Harmand. *Morphology and composition of highly strained InGaAs and InGaAsN layers grown on GaAs substrate*. Applied Physics Letters, vol. 84, page 203, 2004. 60
- [Patton 03] B. Patton, W. Langbein & U. Woggon. *Trion, biexciton, and exciton dynamics in single self-assembled CdSe quantum dots*. Physical Review B, vol. 68, page 125316, 2003. 82
- [Paul 91] S. Paul, J. B. Roy & P. K. Basu. *Empirical expressions for the alloy composition and temperature-dependence of the band-gap and intrinsic carrier density in Ga_xIn_{1-x}As*. Journal of Applied Physics, vol. 69, page 827, 1991. 72
- [Peter 05] E. Peter, P. Senellart, D. Martrou, A. Lemaître, J. Hours, J. M. Gérard & J. Bloch. *Exciton-Photon Strong-Coupling Regime for a*

- Single Quantum Dot Embedded in a Microcavity*. Physical Review Letters, vol. 95, page 067401, 2005. 88
- [Poser 03] F. Poser, A. Bhattacharya, S. Weeke & W. Richter. *Growth of spatially ordered InAs quantum dots on stepbunched vicinal GaAs (100) substrates*. Journal of Crystal Growth, vol. 248, page 317, 2003. 52
- [Pulizzi 04] F. Pulizzi, A. J. Kent, A. Patanè, L. Eaves & M. Henini. *Time-resolved photoluminescence of InAs quantum dots in a GaAs quantum well*. Applied Physics Letters, vol. 84, page 3046, 2004. 74
- [Purcell 46] E. M. Purcell. *Spontaneous emission probabilities at radio frequencies*. Physical Review, vol. 69, page 681, 1946. 87
- [Raymond 96] S. Raymond, S. Fafard, P. J. Poole, A. Wojs, P. Hawrylak, S. Charbonneau, D. Leonard, R. Leon, P. M. Petroff & J. L. Merz. *State filling and time-resolved photoluminescence of excited states in $In_xGa_{1-x}As/GaAs$ self-assembled quantum dots*. Physical Review B, vol. 54, page 11548, 1996. 68
- [Reithmaier 04] J. P. Reithmaier, G. Sek, A. Löffler, C. Hofmann, S. Kuhn, S. Reitzenstein, L. V. Keldysh, V. D. Kulakovskii, T. L. Reinecke & A. Forchel. *Strong coupling in a single quantum dot semiconductor microcavity system*. Nature, vol. 432, page 197, 2004. 88
- [Riel 02] B.J. Riel, K. Hinzer, S. Moisa, J. Fraser, P. Finnie, P. Piercy, S. Fafard & Z.R. Wasilewski. *InAs/GaAs(100) self-assembled quantum dots: arsenic pressure and capping effects*. Journal of Crystal Growth, vol. 236, page 145, 2002. 48
- [Robinson 05] J. W. Robinson, J. H. Rice, K. H. Lee, J. H. Na & R. A. Taylor. *Quantum-confined Stark effect in a single InGaN quantum dot under a lateral electric field*. Applied Physics Letters, vol. 86, page 213103, 2005. 21
- [Rodt 03] S. Rodt, R. Heitz, A. Schliwa, R. L. Sellin, F. Guffarth & D. Bimberg. *Repulsive exciton-exciton interaction in quantum dots*. Physical Review B, vol. 68, page 035331, 2003. 79

- [Ru 03] Eric C. Le Ru, Patrick Howe, Tim S. Jones & Ray Murray. *Strain engineered InAs/GaAs quantum dots for 1.5 μm emitters*. *physica status solidi (c)*, vol. 0, pages 1221–1224, 2003. 51
- [Sadoka 01] K. Sadoka. *Optical properties of photonic crystals*. Springer, Berlin, 2001. 92
- [Saint-Girons 06a] G. Saint-Girons, N. Chauvin, A. Michon, G. Patriarche, G. Beau-doin, G. Brémond, C. Bru-Chevallier & I. Sagnes. *Microphotoluminescence of exciton and biexciton around 1.5 μm from a single InAs/InP(001) quantum dot*. *Applied Physics Letters*, vol. 88, page 133101, 2006. 21
- [Saint-Girons 06b] G. Saint-Girons, I. Sagnes & G. Patriarche. *Indium incorporation in In-rich $\text{In}_x\text{Ga}_{1-x}\text{As}/\text{GaAs}$ layers grown by low-pressure metalorganic vapor-phase epitaxy and its influence on the growth of self-assembled quantum dots*. *Physical Review B*, vol. 73, page 045308, 2006. 60
- [Sanguinetti 99] S. Sanguinetti, M. Henini, M. Grassi Alessi, M. Capizzi, P. Frigeri & S. Franchi. *Carrier thermal escape and retrapping in self-assembled quantum dots*. *Physical Review B*, vol. 60, no. 11, pages 8276–8283, Sep 1999. 73
- [Santori 01] C. Santori, M. Pelton, G. Salomon, Y. Dale & Y. Yamamoto. *Triggered Single Photons from a Quantum Dot*. *Physical Review Letters*, vol. 86, page 1502, 2001. 15, 22
- [Savona 98] V. Savona. *Confined photon systems- fundamentals and applications lectures notes*. Springer, 1998. 88
- [Schmidt 06] R. Schmidt, U. Scholz, M. Vitzethum, R. Fix, C. Metzner, P. Kailuweit, D. Reuter, A. Wieck, M. C. Hübner, S. Stuffer, A. Zrenner, S. Malzer & G. H. Döhler. *Fabrication of genuine single-quantum-dot light-emitting diodes*. *Applied Physics Letters*, vol. 88, page 121115, 2006. 95, 96

- [Sebald 02] K. Sebald, P. Michler, T. Passow, D. Hommel, G. Bacher & A. Forchel. *Single-photon emission of CdSe quantum dots at temperatures up to 200 K*. Applied Physics Letters, vol. 81, pages 2920–2922, 2002. 21
- [Seeger 85] K. Seeger. *Semiconductor physics*. Springer, 1985. 105
- [Seo 03] J.W. Seo, E. Couteau, P. Umek, K. Hernadi, P. Marcoux, B. Lukic, Cs. Mikó, M. Milas, R. Gaál & L. Forró. *Synthesis and manipulation of carbon nanotubes*. New Journal of Physics, vol. 5, page 120, 2003. 33
- [Shahimin 04] M. M. Shahimin. *Investigation of the role of coherent rayleigh noise in the accurate determination of the backscattered brillouin signal*. <http://www.ecs.soton.ac.uk/mms04r/project/body.htm>, 2004. 17
- [Shchukin 99] Vitaliy A. Shchukin & Dieter Bimberg. *Spontaneous ordering of nanostructures on crystal surfaces*. Reviews of Modern Physics, vol. 71, page 1125, 1999. 62
- [Shchukin 01] V.A. Shchukin, N.N. Ledentsov & D. Bimberg. *Spontaneous formation of nanostructures on crystal surfaces*. Physica E, vol. 9, pages 140–148, 2001. 43
- [Shin 06] Hyunho Shin, Jong-Bong Kima, Yo-Han Yoo, Woong Lee, Euijoon Yoon & Young-Moon Yu. *Enhanced strain of InAs quantum dots by an InGaAs ternary layer in a GaAs matrix*. Journal of Applied Physics, vol. 99, page 023521, 2006. 49
- [Song 06] H. Z. Song, T. Usuki, Y. Nakata, N. Yokoyama, H. Sasakura & S. Muto. *Formation of InAs/GaAs quantum dots from a subcritical InAs wetting layer: A reflection high-energy electron diffraction and theoretical study*. Physical Review B, vol. 73, page 115327, 2006. 31
- [Stranski 38] I.N. Stranski & L. Krastanov. *Zur Theorie der orientierten Ausscheidung von Ionenkristallen aufeinander*. Sitzungsbericht Akademie der Wissenschaften Wien, Math.-naturwiss. Kl. IIb, vol. 146, pages 797–810, 1938. 40

- [Streiff 05] M. Streiff, B. Witzigmann, C. Zinoni, B. Alloing, C. Monat & A. Fiore. *Technology CAD based design of semiconductor optical microcavities for single photon emitters*. Proceedings - SPIE, vol. 5840, page 602, 2005. 121
- [Stucki 02] D. Stucki, N. Gisin, O. Guinnard, G. Ribordy & H. Zbinden. *Quantum key distribution over 67 km with a plug&play system*. New journal of Physics, vol. 4, pages 41.1–41.8, 2002. 16
- [Sun 06] Z. Z. Sun, S. F. Yoon, W. K. Loke & C. Y. Liu. *Mechanism of emission-energy tuning in InAs quantum dots using a thin upper confinement layer*. Applied Physics Letters, vol. 88, page 203114, 2006. 49
- [Takemoto 04] K. Takemoto, Y. Sakuma, S. Hirose, T. Usuki & N. Yokoyama. *Observation of Exciton Transition in 1.3-1.55 μm Band from Single InAs/InP Quantum Dots in Mesa Structure*. Japanese Journal of Applied Physics, vol. 43, page L349, 2004. 21
- [Teich 88] M.C. Teich & B. E. A. Saleh. Progress in optics, volume 26. North-Holland, Amsterdam,, 1988. 82
- [Trofimov 04] Vladimir I. Trofimov, Hee Seok Park & Jong-Il Kim. *Growth and optical properties of InAs/GaAs quantum dot structures*. Applied Surface Science, vol. 226, pages 45–51, 2004. 48
- [Tu 04] Y. Tu & J. Tersoff. *Origin of Apparent Critical Thickness for Island Formation in Heteroepitaxy*. Physical Review Letters, vol. 93, page 216101, 2004. 46
- [Vanderbilt 91] D. Vanderbilt & L. K. Wickham. *Elastic energies of coherent germanium islands on silicon*. Materials Research Society Symposium Proceedings, vol. 202, page 555, 1991. 41
- [Venables 84] J. A. Venables, G. D. T. Spiller & M. Hanbucken. *Nucleation and growth of thin films*. Reports on Progress in Physics, vol. 47, page 399, 1984. 56, 57

- [Volmer 26] M. Volmer & A. Weber. *Keimbildung in übersättigten Gebilden*. Zeitschrift der. physikalischen Chemie, vol. 119, pages 277–301, 1926. 40
- [Vuckovic 03] J. Vuckovic, D. Fattal, C. Santori, G. S. Solomon & Y. Yamamoto. *Enhanced single-photon emission from a quantum dot in a micropost microcavity*. Applied Physics Letters – May 26, 2003 – Volume 82, Issue 21, pp. 3596-3598, vol. 82, pages 3596–3598, 2003. 88
- [Wang 94] G. Wang, S. Fafard, D. Leonard, J. E. Bowers, J. L. Merz & P. M. Petroff. *Time-resolved optical characterization of InGaAs/GaAs quantum dots*. Applied Physics Letters, vol. 64, page 2815, 1994. 74
- [Wang 04] Zh. M. Wang, Sh. Seydmohamadi, J. H. Lee & G. J. Salamo. *Surface ordering of (In,Ga)As quantum dots controlled by GaAs substrate indexes*. Applied Physics Letters, vol. 85, page 5031, 2004. 52
- [Ward 04] M.B. Ward, D.C. Unitt, Z. Yuan, P. See, R.M. Stevenson, K. Cooper, P. Atkinson, I. Farrer, D.A. Ritchie & A.J. Shields. *Single quantum dot electroluminescence near 1.3 μm* . Physica E, vol. 21, pages 390–394, 2004. 95
- [Ward 05] M. B. Ward, O. Z. Karimov, D. C. Unitt, Z. L. Yuan, P. See, D. G. Gevaux, A. J. Shields, P. Atkinson & D. A. Ritchie. *On-demand single-photon source for 1.3 μm telecom fiber*. Applied Physics Letters, vol. 86, page 201111, 2005. 22
- [Winston] D. Winston. <http://ece-www.colorado.edu/~bart/ecen5355/f05/simwindows.htm>. 103, 104
- [Wootters 82] W. K. Wootters & W. H. Zurek. *A single quantum cannot be cloned*. Nature, vol. 299, pages 802–803, 1982. 15
- [Xu 98] S. J. Xu, X. C. Wang, S. J. Chua, C. H. Wang, W. J. Fan, J. Jiang & X. G. Xie. *Effects of rapid thermal annealing on structure and luminescence of self-assembled InAs/GaAs quantum dots*. Applied Physics Letters, vol. 72, page 3335, 1998. 51

- [Xu 04] X. Xu, D. A. Williams & J. R. A. Cleaver. *Electrically pumped single-photon sources in lateral p-i-n junctions*. Applied Physics Letters, vol. 85, page 3238, 2004. 95, 110
- [Yablonovitch 87] E. Yablonovitch. *Inhibited spontaneous emission in solid state physics and electronics*. Physical Review Letters, vol. 58, page 2059, 1987. 92
- [Yamaguchi 02] K. Yamaguchi, T. Kaizu, K. Yujobo & Y. Saito. *Uniform formation process of self-organized InAs quantum dots*. Journal of Crystal Growth, vol. 237, page 1301, 2002. 72
- [Yang 97] W. Yang, R. R. Lowe-Webb, H. Lee & P. C. Sercel. *Effect of carrier emission and retrapping on luminescence time decays in InAs/GaAs quantum dots*. Physical Review B, vol. 56, page 13314, 1997. 74
- [Yariv 91] A. Yariv. Optical electronics. Saunders College, San Francisco, 1991. 115, 116
- [Yeh 00] N.-T. Yeh, T.-E. Nee, J.-I. Chyia, T. M. Hsu & C. C. Huang. *Matrix dependence of strain-induced wavelength shift in self-assembled InAs quantum-dot heterostructures*. Applied Physics Letters, vol. 76, page 1567, 2000. 49
- [Yoshie 04] T. Yoshie, A. Scherer, J. Hendrickson, G. Khitrova, H. M. Gibbs, G. Rupper, C. Ell, O. B. Shchekin & D. G. Deppe. *Vacuum Rabi splitting with a single quantum dot in a photonic crystal nanocavity*. Nature, vol. 432, pages 200–203, 2004. 88
- [Yuan 02] Zhiliang Yuan, Beata E. Kardynal, R. Mark Stevenson, Andrew J. Shields, Charlene J. Lobo, Ken Cooper, Neil S. Beattie, David A. Ritchie & Michael Pepper. *Electrically Driven Single-Photon Source*. Science, vol. 295, page 102, 2002. 95, 96, 110
- [Zbinden 97] H. Zbinden, J.D. Gautier, N. Gisin, B. Huttner, A. Muller & W. Tittel. *Interferometry with Faraday mirrors for quantum cryptography*. Electronics Letters, vol. 33, page 568, 1997. 15

- [Zinoni 04] C. Zinoni, B. Alloing, C. Paranthoën & A. Fiore. *Three-dimensional wavelength-scale confinement in quantum dot microcavity light-emitting diodes*. Applied Physics Letters, vol. 85, page 2178, 2004. 114, 115
- [Zinoni 06] C. Zinoni, B. Alloing, C. Monat, V. Zwiller, L.H. Li, A. Fiore, L. Lunghi, A. Gerardino, H. de Riedmatten, H. Zbinden & N. Gisin. *Time-resolved and antibunching experiments on single quantum dots at 1300 nm*. Applied Physics Letters, vol. 88, page 131102, 2006. 22, 81, 82, 85, 86
- [Zwiller 03] V. Zwiller, T. Aichele, W. Seifert, J. Persson & O. Benson. *Generating visible single photons on demand with single InP quantum dots*. Applied Physics Letters, vol. 82, pages 1509–1511, 2003. 21
- [Zwiller 04] V. Zwiller, T. Aichele & O. Benson. *Quantum optics with single quantum dot devices*. New Journal of Physics, vol. 6, page 96, 2004. 21

Acknowledgements

This thesis project was above all a team work and I would like to thank all people who contribute directly or indirectly to its realization:

First of all, my thesis supervisor **Andrea Fiore**, thank you for giving me the opportunity to work in your group, thanks for your availability and listening (even at 8 PM), thank you for your support and motivation, it was really a great pleasure and a chance for me to work with you.

Lianhe Li and **Cyril Paranthoën**, my two "MBE bosses", thank you Cyril for introducing me to the MBE growth mystery, for your inexhaustible interest in quantum dot field and for your effort and patience regarding MBE caprices...Thank you Lianhe for your kindness, for being always ready to share your knowledge and for the numerous discussions we have had. I will be glad to visit you in China!

Carl Zinoni and **Christelle Monat**, my office mates and also team-workers of the single photon project; many thanks Carl for your profound knowledge of electronic and of simulation tool, thanks Christelle for your work on LED structures. Your contributions gave the possibility to achieve such nice results.

Laurent Balet for rescuing me at the end of my thesis and **Lamberto Luighi** for your e-beam processes expertise and for calmness in every situation.

Aline Gruaz for your invaluable assistance in administrative worries.

All the technical team, in particular **Yoan Trolliet** for keeping everything in order and specially the MBE room, and **Nicolas Leiser** for your precious help before Yoan arrival, for keeping the clean-room running and for help in multiple occasions, always with smile.

Hansjörg Bühlmann for your wire-bonding experience among your knowledge extent.

Members of the institute and in particular members or ex-members of the Quantum Devices' group: **Alexander Markus**, **Marco Rossetti**, **Pablo Moreno alias Robin Wood**, **David Bitauld**, **Francesco Marsili**, **Philipp Ridha**, **Nicolas Chauvin**, **Andrea Dunbar**, **Reto Joray**, **Samuel Sonderreger**, **Raphael Butté**, **Eric Feltin**, **Pascal Gallo**... Thank you for your friendship which gives a so nice work atmosphere to the lab.

All of “Bossette”-and-grill addicted people which allowed me to be disconnected from the physics world every Friday evening: **Christiane, Isabelle, Lorena, Sebastien, Rolando, Deborah, Julien, Kathy, Julie, Jean, Barbara, Michael, Luigi, Irène, Laure, Stefan, Maxime, Fabienne, David, Fahd, Palma, Kay, Marike,**... the list is endless.

Members of the jury, **Nicolas Grandjean, Massimo Gurioli, Jean-Christophe Harmand,** and **Georges Meylan** who took time to read and correct my manuscript and gave me the possibility to present my work.

Lars for your daily support, advice, and presence even far from 800 km.

My brothers and sisters, and above all, my parents for your love and never ending support.

ALLOING Blandine

✉ Rue de la Pontaise 43bis
CH-1018 Lausanne
☎ +41 21 646 76 12 (private)
+41 21 693 53 77 (office)

Date of birth: February 23, 1979
Single
Nationality: French
Email: blandine.alloing@epfl.ch

EDUCATION

- Nov 2002 - present **Research assistant / PhD. Thesis: *Growth and characterization of single quantum dot devices for fiber-based quantum communications.***
Swiss Federal Institute of Technology (EPFL), Institute of Quantum Electronics and Photonics, Lausanne, Switzerland
Thesis Advisor: Prof. A. Fiore
- 2201-2002 **Pre-doctorate diploma (DEA) in material sciences, Caen University, France**
- 1999-2002 **Master's degree in Science and graduate physics engineer**
"Institut des sciences de la matière et du rayonnement" (ISMRA), National Graduate Engineering School, Caen, France.
- 1997 **Baccalauréat, Lycée Joffre (secondary school), Montpellier, France.**

PROFESSIONAL EXPERIENCE

- 2002 - 6 month **Picogiga Company, Marcoussis, France**
Diploma thesis: *Realization of GalnAsN laser emitting at telecommunication wavelength.*
- 2001 - 2002 **PHILIPS Semi-conducteurs - CNRS/CRISMAT laboratory, Caen, France :**
Project: *Study of recycling possibilities of mechanical pieces used in epitaxial reactors.*
- 2001 - 4 month **Toronto University - Canada:**
Internship: *Study of brass oxidation in humid environment*
- 2000 -2 month **SIEMENS automobile department - Würzburg, Deutschland:**
Internship: *Work on the assembly line.*

PERSONAL INTERESTS

Associative activities :

- Member of the student association of Caen Engineering School
- Secretary in the humanitarian student association « ISF » (Ingénieurs Sans Frontière). Construction project of a school with 3 classrooms in Burkina Faso.
- 1997: Certificate of competence to be organizer in holiday colonies.

Hobbies :

- Sport: ballet, volleyball, hiking
- Piano

PUBLICATIONS:

Participation to conferences:

- **Oral presentations**
 - *International Workshop on Semiconductor quantum dot based devices and applications* (IWSQDA), Paris (France), March 16-17, 2006
 - *Material Research Society*, Boston (USA), November 27-December 2, 2005
 - *MBE Workshop*, Grindelwald (Switzerland), March 7-9, 2005
 - *National Centers of Competence in Research Meeting*, Neuchâtel (Switzerland), June 2004
- **Poster presentations**
 - *Quantum Dots 2004*, Banff (Canada) May 10-13, 2004
 - *Semiconductor Quantum Dots: Physics and devices*, Summer School, Monte Verità, Ascona (Switzerland), September 5-10, 2004
 - *Quantum Optics*, Summer School, Granada (Spain), September 27- October 2, 2003

Refereed Journal Articles:

- B. Alloing, C. Zinoni, L. H. Li and A. Fiore
“*Structural and optical properties of low-density and In-rich InAs/GaAs quantum dots*”
Accepted for publication in *Journal of Applied Physics*.
- C. Monat, B. Alloing, C. Zinoni, L. H. Li, and A. Fiore
“*Nanostructured Current-Confined Single Quantum Dot Light-Emitting Diode at 1300 nm*”
Nanoletters, Vol.6, 1464, 2006
- C. Zinoni, B. Alloing, C. Monat, V. Zwiller, L. H. Li, A. Fiore, L. Lunghi, A. Gerardino H. de Riedmatten, H. Zbinden, and N. Gisin
“*Time-resolved and antibunching experiments on single quantum dots at 1300nm*”
Applied Physics Letters, Vol 88, 131102, 2006
- B. Alloing, C. Zinoni, V. Zwiller, L.H. Li, C. Monat, M. Gobet, G. Buchs, A. Fiore, E. Pelucchi and E. Kapon
“*Growth and characterization of single quantum dots emitting at 1300 nm*”
Applied Physics Letters, Vol. 86, 101908, 2005
- C. Zinoni, B. Alloing, C. Paranthon, and A. Fiore
“*Three-dimensional wavelength-scale confinement in quantum dot microcavity light-emitting diodes*”
Applied Physics Letters, Vol. 85, 2178, 2004
- Fiore, M. Rossetti, B. Alloing, C. Paranthoën, J.X. Chen, L. Geelhaar, and H. Riechert
“*Carrier diffusion in low-dimensional semiconductors: A comparison of quantum wells, disordered quantum wells, and quantum dots*”
Physical Review B, Vol. 70, 205311, 2004

Conference Proceedings:

- C. Zinoni, B. Alloing, C. Monat, L. H. Li, L. Lunghi, A. Gerardino and A. Fiore
"Time-resolved measurements on low-density single quantum dots at 1300nm"
QD 2006 proceeding, to be published in Physica Status Solidi (c).
- M. Francardi, L. Balet, A. Gerardino, C. Monat, C. Zinoni, L.H. Li, B. Alloing, N. Le Thomas, R. Houdré and A. Fiore
"Quantum dot photonic crystal nanocavities at 1300 nm for telecom-wavelength single-photon sources"
QD 2006 proceeding, to be published in Physica Status Solidi (c).
- A. Fiore, C. Zinoni, B. Alloing, V. Zwiller, L.H. Li and C. Monat
"Nanoscale single quantum dot devices at 1300 nm"
SPIE proceeding, Vol. 5734, 106, 2005
- M. Streiff, B. Witzigmann, C. Zinoni, B. Alloing, C. Monat and A. Fiore
"Technology CAD based design of semiconductor optical microcavities for single photon emitters"
SPIE proceeding, Vol. 5840, 602, 2005
- Fiore, C. Zinoni, B. Alloing, C. Monat, L. Balet, L.H. Li, N. Le Thomas, R. Houdré, L. Lunghi, M. Francardi, A. Gerardino and G. Patriarche
"Telecom-wavelength single-photon sources for quantum communications"
Nanocose 3 proceeding, to be published in Journal of Physics: Condensed Matter (March 2007)
- A. Gerardino, M. Francardi, L. Balet, C. Monat, C. Zinoni, B. Alloing, L.H. Li, N. Le Thomas, R. Houdré and A. Fiore
"Fabrication and characterization of point defect photonic crystal nanocavities at telecom wavelength"
Micro- and Nano-Engineering 2006 proceeding, to be published in Microelectronic Engineering (April 2007).